The Mechanisms of Rubber Abrasion

Guangchang Wu

A thesis submitted for the degree of Doctor of Philosophy

School of Engineering and Materials Science

Queen Mary University of London

October 2016

Abstract

Rubber abrasion is one of the most important properties for rubber products, such as tyres. However, due to its complexity rubber abrasion is still a very challenging topic in rubber research. Rubber abrasion is not governed by a single mechanism. Different mechanisms can dominate the abrasion behaviour depending on the rubber compound, base polymer type, loading severity, contact conditions, testing temperature and chemical environment. This study investigates the different mechanisms for rubber abrasion and the transition between these mechanisms using two types of abrasion apparatus, a blade abrader and a surface abrader, respectively.

Blade abrasion was used to generate the abrasion pattern. Once the abrasion pattern was formed on the rubber surface under unidirectional sliding, the underlying mechanism was primarily one of fatigue crack growth, which is referred as “fatigue wear” in the literature. An independent pure shear fatigue test with various loading profiles was conducted to predict the crack growth rate using a fracture mechanics approach during these abrasion tests. The tearing energy during blade abrasion was calculated using a fracture mechanics approach. A Finite Element Analysis (FEA) technique using the Virtual Crack Closure Technique (VCCT) was adopted. The VCCT approach was a simpler, faster and more reliable approach to derive the tearing energy under these complicated large strain contact conditions. The prediction of the abrasion rate using this independent measurement of the crack growth resistance of materials worked best for unfilled SBR material.

A bespoke surface contact abrasion machine was used to investigate rubber abrasion on silicon carbide sandpaper under both dry and wet conditions. Depending on the materials, contact conditions and sliding velocity, two different mechanisms were observed. The first being a mechanochemical degradation, during which a sticky layer was generated on the rubber surface. This behaviour is also called “smearing wear”. The second failure mode resulted from a purely mechanical fracture named “abrasive wear”. It seemed that the carbon black filled rubber was more susceptible to smearing wear than the silica filled one. Higher sliding velocities promoted smearing wear, possibly due

to higher temperatures being generated at the interface. Alternatively, water lubrication was seen to promote abrasive wear. Therefore, the abrasion mechanism changed to more rapid abrasive wear under wet conditions, which resulted in a significant increase in the rate of weight loss.

Finally, the sticky debris generated during the smearing wear was characterised using various different techniques. This revealed that the sticky debris had more oxygen and lower carbon and sulphur content. It contained a greater amount volatiles and generated more char formation during its degradation in the air. The molecular weight of the sticky debris was much lower when compared to the original uncured rubber. It seemed that in the sticky debris the filler network can slowly recover and the degraded polymer chains can re-absorb back onto filler surface forming “bound rubber”, which leads to faster rates of weight loss.

Declaration

I hereby declare that all the works presenting in this thesis are originally done by myself during my graduate study. And all the referenced and collaborating works have been illustrated as they are.

I confirm that this thesis has not been previously submitted for the award of a degree by this or any other university.

Guangchang Wu

Signature:

Date

Details of publications and conference proceedings

Publications:

G. Wu, AG. Thomas, JJC. Busfield. *Estimating strain energy release rate during blade abrasion using finite element analysis* in Constitutive Models for Rubber IX: Proceedings of the Ninth European Conference on Constitutive Models for Rubber, CRC Press, Prague, Czech Republic, September 2015, ISBN: 1315658151.

G. Wu, AG. Thomas, JJC Busfield. *Investigation of rubber abrasion based on laboratory testing*, Tire Technology International, Annual Review, 2015.

G. Wu, AG. Thomas, JJC. Busfield. 2013. Effect of the blade sharpness on the blade abrasion of rubber. in Constitutive Models for Rubber VIII: Proceedings of the Eighth European Conference on Constitutive Models for Rubber, CRC Press, San Sebastian, Spain, June 2013, ISBN: 1138000728

G. Wu, LB. Tunnicliffe, AG. Thomas, JJC Busfield. *Characterisation on the sticky debris on the rubber surface during abrasion*, in preparation.

G. Wu, AG. Thomas, JJC Busfield. *Investigation the different abrasion mechanisms of elastomer and the transition under different test conditions*, in preparation.

Details of conference proceedings:

G. Wu, LB. Tunnicliffe, T. Tada, JJC Busfield. *Chemical degradation of elastomers during abrasion*, International Rubber Conference, Kitakyushu, 2016.

G. Wu, JJC Busfield. *Characterization of the sticky debris generated on rubber surface during abrasion*, American Chemical Society, 190th Technical Meeting of the Rubber Division, Pittsburgh, 2016.

G. Wu, AG. Thomas, JJC Busfield. *Estimating strain energy release rate during blade abrasion using virtual crack closure technique*, American Chemical Society, 188th Technical Meeting of the Rubber Division, Cleveland, 2015.

G. Wu, AG. Thomas, JJC Busfield. *Prediction of rubber abrasion*, American Chemical Society, 186th Technical Meeting of the Rubber Division, Nashville, 2014.

G. Wu, AG. Thomas, JJC Busfield. *Prediction of rubber abrasion*, International Rubber Conference, Beijing, 2014.

G. Wu, AG. Thomas, JJC Busfield. C*orrelation between blade abrasion and real road wear test*, American Chemical Society, 184th Technical Meeting of the Rubber Division, Cleveland, 2013.

Acknowledgements

I would like to express my gratitude to my supervisor Professor James Busfield for giving me the opportunity to do a PhD degree and introducing me to the magnificent rubber world. Without his tremendous help, encouragement, and research support, I could never keep it going so far.

I would like to thank Cabot Corp for sponsoring my PhD project. Especially, I would like to express my gratitude to Dr Michael Morris, Dr Dhava Doshi, and Fred Rumph for their interests and useful discussion for my work and allowing me to access their laboratory facilities. I would like express my gratitude to Prof Paul Sotta in Laboratoire Polymères et Matériaux Avancés for the collaboration on the characterisation of the wear debris using the double quantum NMR. I would also like to thank Dr Toshio Tada at Sumitomo Rubber Industries for the collaboration work on investigation the sticky layer generated during rubber abrasion. All the academic staff and experiment technicians in School of Engineering and Materials Science are acknowledged.

I would like to also thank all the current and former members in the Soft Matter Group for all the knowledge, training, discussion, and inspiration that I get from them. In particular, I would like to thank Prof Alan Thomas, Dr Lewis Tunnicliffe, Dr Menglong Huang, Thomas Baumard, Hediyeh Zahabi, Richard Winslow, and Yinping Tao, who make me feel like a big family in the group. I would like to thank all my friends I met in London, particularly, Lei Fu, Dr Jian Yao, Kailun Zheng, Jingjing Zhao, Tianyi Tao, and Xi Zhang.

Finally, I would like to express my sincere gratitude to my parents for supporting me to study abroad and my wife for being long-distance with me for over five years. Their understanding and support are always the faith in me, which keeps me moving forward.

Table of Contents

List of Abbreviations

6PPD	(N(1,3-dimethyl-butyl)-N'-phenyl-P-phenylenediamine)
BET	(Brunauer, Emmett, and Teller)
BR	(Butadiene Rubber)
CBS	(N-cylcohexylbenzothiazole-2-sulfenamide)
CTAB	(Cetyltrimethyl Ammonium Bromide)
DBPA	(Di(n-dibutyl) phthalate absorption)
DMA	(Dynamic Mechanical Analysis)
DSC	(Differential Scanning Calorimetry)
DPG	(Diphenyl Guanidine)
DQ-NMR	(Double Quantum Nuclear Magnetic Resonance Spectroscopy)
EDX	(Energy-dispersive X-ray Spectroscopy)
EPR	(Electro Paramagnetic Resonance)
FEA	(Finite Element Analysis)
GPC	(Gel Permeation Chromatography)
HNBR	(Hydrogenated Nitrile Butadiene Rubber)
IR	(Infrared)
MA	(Massachusetts)
NR	(Natural Rubber)
RID	(Refractive Index Detector)
SEM	(Scanning Electron Microscopy)
SEF	(Strain Energy Function)
TEA	(Triethylamine)
TEM	(Transmission Electron Microscopy)
TGA	(Thermogravimetric Analysis)
THF	(Tetrahydrofuran)
TTS	(Time Temperature Superposition)
USA	(United State of American)
VCCT	(Virtual Crack Closure Technique)
WLF	(Williams, Landel and Ferry)

List of Symbols

$[O_3]$	Concentration of ozone
A	Abradability or abrasion coefficient
A_H	Helmholtz free energy
A_s	Area
A_t	Constant for fatigue crack growth in chemical-mechanical region
a_T	WLF function frequency shift factor
a_L	Length of contact area
B_t	Constant for power law relationship of fatigue crack growth
b	Statistical segment length
b_f	Fatigue wear steadiness
C_1, C_2	Material constants for Mooney SEF
C_{W1}, C_{W2}	WLF constant
c	Crack length
D_0, d_0	Initial external and internal diameter of rubber wheels
D_{com}	Bulk compliance
E	Young's modulus
E_b	Bulk modulus
e	Additional strained length of fatigue test sample
F	Elastic force
F_F	Friction force
F_N	Normal force
F_{ad}	Adhesion contribution of friction
F_{def}	Deformation or hysteresis contribution of friction
f_f, f_p	Filler and polymer fraction
G	Shear modulus
G'	In-phase modulus

$G"$	Out-phase modulus
h	Height of fatigue sample
h_0	Thickness or width or wheel sample
I_1, I_2	Strain invariants
I_{ref}	Reference decay for DQ-NMR
I_{DQ}	DQ build-up signal
I_{def}	Network defects long-time signal for DQ-NMR
I_{nDQ}	Normalised DQ signal
$I_{\sum DQ}$	Full magnetization
k	Boltzmann constant
k_c	Correction factor
k_α	Fatigue wear coefficient
L	Length
M_c	Average chain molecular weight between crosslinks
M_e	Entanglement molecular weight
M_w	Weight average molecular weight
m_0	Initial mass
m_d	Dry mass after extraction
N	Number of crosslinks
n	Number of cycles or number of revolutions
P, Q	Material constants for tyre wear model
p	Distance of an abrasion pattern ridge to a reference line
R	Length of end to end vector
R_B	Parameter specifying roughness
R_b	Bound rubber amount
R_{gas}	Gas constant
R_w	Resilience of tyre wheel

r	Radius of rubber wheel
S	Entropy
S_b	Average value of local backbone orientation
S_P	Abrasion pattern spacing
T	Tearing energy
T_t	Temperature
T_s	WLF reference temperature
T_g	Glass transition temperature
T_0	Threshold tearing energy
T_s	Tyre surface temperature
T_A	Reference temperature for tyre wear model
t	Time
U	Internal energy
U_b	Energy density at break
V_0	Initial volume
W	Strain energy density
W_r	Wear rate
w	Length of fatigue sample
ψ	Absolute temperature
λ_i	Principal extension ratios
ρ	Density
ε	Strain
σ	Stress
σ_0	Maximum amplitude of stress
η_e	Viscosity coefficient
γ	Shear strain
γ_0	Maximum amplitude of strain
ω	Angular frequency

δ	Phase angle between stress and strain
β	Constant for power law relationship of fatigue crack growth
μ	Friction coefficient
θ	Crack growth angle during abrasion
θ_s	Slip angle
θ'	Angle between the local chain direction and a reference direction
α	Orientation of end to end vector
α_T	Temperature coefficient of tyre wear model
ξ	Wear resistance
ν	Crosslinking density
τ_{DQ}	Evolution time
ΔU	Energy required to close a crack
X_{1L}, Z_{1L}	Nodal force along X and Z direction at point L
$\Delta u_{2L}, \Delta w_{2L}$	Displacement difference between L and L' in X and Z direction
Δv	Relative displacement
X_i', Z_i'	Forces at the crack tip in the local coordinate system
$\Delta u_i', \Delta w_i'$	Relative displacement behind crack tip in the local coordinate.

List of Equations

List of Tables

List of Figures

1 Chapter One: Introduction

Rubber has been one of the most important engineering materials since the vulcanisation process was invented by Charles Goodyear in 1839. Rubber is a highly stretchable, very elastic and energy absorbable material. The demand for rubber increased rapidly in 1888, when pneumatic tyres were developed by John Dunlop (De and White, 2001). After that rubber became one of the most expensive materials in the world, since at that time rubber was only produced from the latex of rubber trees (Hevea Brasiliensis) found in Brazil. Henry Wickham (Gabriel, 2010), a British explorer, stole about 70,000 seeds of the rubber tree from Brazil and dispatched them to Asia, which significantly promoted the production of rubber.

Today, rubber is not a scarce material. Various different types of rubber are used for various different applications. However, tyres are still the largest applications for rubber materials, which consumed more than half of the rubber produced in the world (Liang, 2007). The requirement for the tyre design can be complicated and depends on different conditions. There are three key requirements for tyre design, wet grip, rolling resistance and abrasion. The aspiration to improve all three qualities in tyre design is known as expanding the “magic triangle” within the tyre industry. No matter what situation is encountered, abrasion rate is one of the key issues, as it is the life limiting performance characteristic in service. However, it is very challenging to predict real tyre wear behaviour. In practice, the tyre wear depends on the tyre construction, the tyre load, the inflation pressure, the suspension system, the vehicle type (two-wheel drive or four-wheel drive), the tyre position (front wheels or rear wheels), the road conditions, the weather conditions, the driving habits and of course the tyre tread properties. Even for carefully controlled laboratory testing, various abrasion machines give different abrasion results and sometimes even reverse performance rankings.

From a scientific perspective, despite the extensive studies on rubber abrasion over the past sixty years, the exact underlying mechanisms remain unresolved. Unlike other materials, due to the relative low modulus and the unique viscoelastic properties, rubber materials can display different abrasion mechanisms under different

circumstances. Depending on the detailed compound formulations where the key parameters include the choice of the base polymer type, the filler type, and the vulcanisation system, the abrasion rate for different rubber can be more than order magnitude different from each other. Even for the same rubber, under different test conditions such as the roughness of the counter surface, ambient temperature, or lubricant conditions, the abrasion rate can also have a scatter greater than one order of magnitude. These factors significantly complicate the study for rubber abrasion.

The aim of this thesis is to investigate the phenomenology and underlying mechanisms of rubber abrasion under well-controlled laboratory conditions. Even though the laboratory tests used here are generally more severe than those experienced during conventional road based tyre testing, it is worth noting that this study aims to derive a better understanding of the degradation mechanisms found in commercial passenger tyre wear rather than those encountered under severe wear conditions such as in aircraft tyres or tyres during motor racing. By applying different types of abrasion test, different fundamental abrasion mechanisms can be separated and investigated individually. To conduct this investigation the thesis is structured as follows.

Chapter 2 gives a brief review on general rubber background knowledge, including types of rubber, vulcanisation processes, rubber elasticity and viscoelasticity, fillers and filler reinforcement, fracture mechanics, and rubber friction. All of these basics are necessary to know to understand the abrasion process.

Chapter 3 presents a detailed literature review on rubber abrasion. Various types of rubber abrasion and the underlying mechanism for each type of abrasion are presented. The main existing abraders and some analytical model used to predict abrasion behaviour are also described. Finally, some gaps in understanding the abrasion mechanisms are highlighted in order to help establish the experimental programme for this project.

Chapter 4 examines the fatigue wear for rubber abrasion, which is the typical dominant abrasion mechanism for rubber abrasion against a smooth surface. Under uni-

directional sliding, a characteristic abrasion pattern is always generated on the rubber surface. A blade abrader is used for this abrasion test in order to apply fracture mechanics to investigate the crack growth once the abrasion pattern is fully developed. An attempt is made to correlate the abrasion results to the independent pure shear fatigue results. Different loading configurations are also applied to the pure shear fatigue crack growth test to try to match the actual loading conditions during abrasion.

Chapter 5 develops a new way to calculate the tearing energy at the steady state during blade abrasion using a novel Finite Element Analysis (FEA) approach, which uses the Virtual Crack Closure Technique (VCCT). The blade abrasion process was carefully modelled using ABAQUS. It was the first time that the VCCT had been used to calculate the tearing energy for blade abrasion. The predicted rate of abrasion coupling this tearing energy prediction with independently measured fatigue crack growth data is then compared with measured lab based abrasion test data.

Chapter 6 investigates the abrasion on surfaces with sharp asperities. A bespoke surface abrader was developed using rubber wheels rotating on silicon carbide sandpaper surfaces. Various different sliding velocities were applied starting from 20 cm/s to 200 cm/s. Both dry and water lubricated contact conditions were used. Depending on actual conditions, two abrasion mechanisms are observed, which are termed abrasive wear and smearing wear. The transition between these two abrasion mechanisms is also discussed.

Chapter 7 presents a systematic study on the characterisation of the sticky debris generated by the smearing wear. The chemical content, glass transition temperature, and the molecular weight of the sticky debris is analysed. The effect of the sticky debris on the final abrasion and friction properties is also discussed.

Chapter 8 summarises the key findings obtained in this work and gives some ideas for ongoing and future work.

2 Chapter Two: General Background on Rubber Materials

2.1 What is Rubber?

Polymeric materials that can be stretched to a large strain and which return their original shape are known as rubber or elastomer materials. The term “rubber” was coined by Joseph Priestly. In 1770, he found that the dry latex could easily rub out the marks of a black lead pencil from paper (Loadman, 2005). The word, elastomer as elastic polymer is often used interchangeably with rubber, although according to ISO1382:1996 the term elastomer can be used for any polymer that exhibits large strain elasticity, the word rubber implies a material which in addition to this requirement is also insoluble in a suitable swelling solvent.

Rubber materials are widely used in modern daily life, from simple rubber bands to much more complicated structures such as car tyres. Back in 1600 BC the ancient Mesoamerican Mayas already knew how to manufacture bouncing rubber balls using rubber latex (Hosler et al., 1999). The use of rubber materials however really only took off in engineering applications once the sulphur vulcanisation was accidentally discovered by Charles Goodyear in 1839 and which he subsequently patented in 1844, when he subjected a rubber compound to the heat of a hot stove (Baranwal and Stephens, 2001). Polymers that illustrate rubbery properties can be defined by the following four requirements (Treloar, 1975, Cowie and Arrighi, 2007).

- It is normally above its glass transition temperature at room temperature.
- The polymer is amorphous at least not highly crystalline.
- The force between the molecules must be weak.
- The polymer should be cross-linked.

2.2 Types of Rubber

Various different types of rubber are used for a wide variety of engineering application. In general, rubber can be divided in two categories: natural rubber and synthetic rubber, respectively. Natural rubber is extracted from natural plants. The other types of rubber

are chemically synthesised rubber. The three main types of rubber, which are mostly used in the tyre industry are introduced below.

2.2.1 Natural Rubber (NR)

Although a large number of natural plants contain NR, the most widely cultivated source of NR is from the tree sap from “rubber tree”, Hevea Brasiliensis. The latex is collected by ‘tapping’ of the tree, where a slit is made into the bark of the rubber tree to allow the flow of a milky sap. The latex contains water, polyisoprene, and small quantities of other ingredients such as proteins and carbohydrates (Ciesielski, 1999). Then it is coagulated and processed to form a processable coagulum.

NR is a high molecular weight (200,000 – 500,000 Da), long chain, stereoregular polymer (Baranwal and Stephens, 2001). It is primarily composed of cis- 1,4- polyisoprene. The molecular configuration is shown in Figure 2-1. The glass transition temperature of NR is around -70 °C. Due to its stereoregular structure, NR can crystallise either at low temperature or in the strained state. The strain-induced crystallisation results from the melting points of the NR crystals increasing as the molecules are oriented with strain. Therefore, NR displays a self-reinforcing mechanism and has an outstanding tensile strength and fatigue behaviour. However, owing to the presence of natural impurities NR has inherently large intrinsic flaw. As a consequence of the unsaturated double bond it also has a low chemical stability, susceptible at high temperature and high concentration of ozone and under ultraviolet light. NR has a relatively good abrasion resistance at low severity. However, at high severity the abrasion properties are poor.

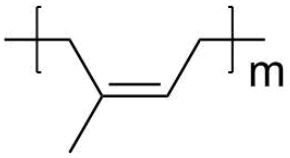

Figure 2-1. Chemical Structure of cis-polyisoprene.

2.2.2 Styrene Butadiene Rubber (SBR)

SBR is the most widely used synthetic rubber, which represents half of all synthetic rubber production. The production of SBR began as a war time emergency to provide a material suitable to replace NR in many products (Baranwal and Stephens, 2001). SBR is a random copolymer of styrene and butadiene. The chemical structure is shown in Figure 2-2. SBR can be synthesised by free-radical polymerisation as an emulsion in water creating a material known as emulsion SBR (E-SBR) or anionically in solution which creates a material known as solution SBR (Gent, 2012).

The glass transition temperature for SBR is between -50 to -10 °C depending on the vinyl content. As a random copolymer, SBR does not show crystallisation behaviour. In comparison with NR, gum vulcanisates (unfilled) made from SBR have poor mechanical properties. As a result, SBR is always used as a composite material incorporating a reinforcing filler such as carbon black. Filled SBR has good mechanical properties, which are comparable to that of filled NR.

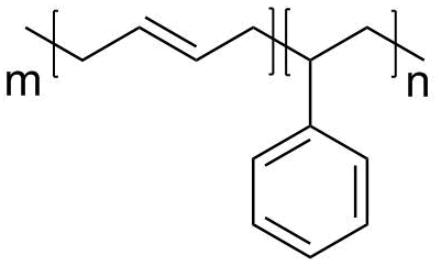

Figure 2-2. Chemical structure of styrene butadiene rubber.

2.2.3 Butadiene Rubber (BR)

Another widely used rubber for tyre tread compounds is BR, which is another synthetic polymer. It consists of butadiene unit, which can form either a cis-1,4 polybutadiene or a trans-1,4 polybutadiene conformation as well as 1,2 polybutadiene as shown in Figure 2-3. BR is commonly used as a blend with other rubber due to its relatively poor strength and the difficulty in processing the material. The glass transition temperature for low-vinyl BR is very low around -100 °C. There BR confers high resilience (good elasticity), low heat build-up, and good abrasion resistance (Ciesielski, 1999).

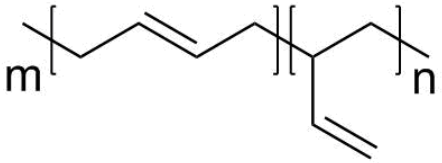

Figure 2-3. Chemical structure of butadiene rubber.

2.3 Vulcanisation

Raw gum rubber is a very flexible and mechanically weak material which has very limited use. It does not return to its original shape after a large deformation and can be dissolved in a suitable solvent. Vulcanisation is the process by which rubber is changed from essentially a viscous liquid to either an elastic or a hard material (Baranwal and Stephens, 2001). It involves producing network junctions by the insertion of crosslinks between polymer chains (Mark et al., 2013). The mechanical properties of rubber are dramatically enhanced by the vulcanisation process.

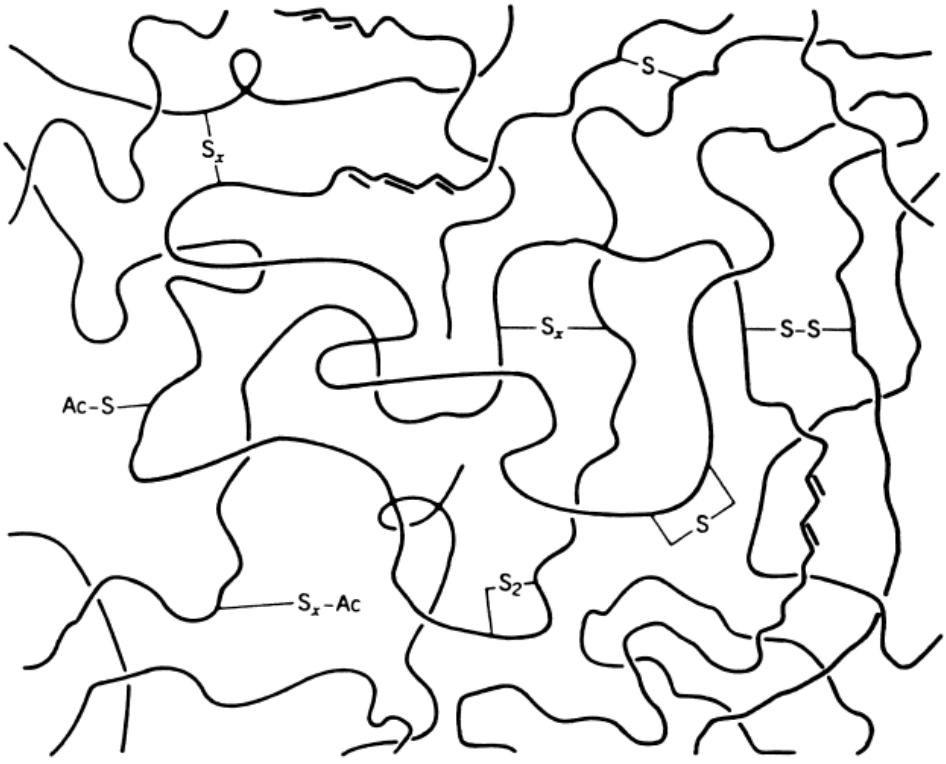

Figure 2-4. 2-D schematic polymer structure after sulphur vulcanisation with different types of crosslinks (Mark et al., 2013).

The most widely used curing agent is sulphur. Since vulcanisation with sulphur alone is both time consuming and inefficient, accelerators are always used to speed up the rate of vulcanisation. Another two materials, zinc oxide and stearic acid together with sulphur and an accelerator typically constitute the cure system (Ciesielski, 1999). The long chains of the rubber molecules are simply linked together by crosslinks of one or more sulphur atoms as show in Figure 2-4. The number of sulphur atoms per crosslink alters the properties of the cured rubber. The C-S bond is more stable than S-S bond. The stability of S-S bond decreases as the number of sulphur atoms in the crosslink increases as shown in Table 2-1. However, the tensile strength, elasticity and fatigue properties are found to be improved as the length of the sulphide crosslinking increases. This is due to the lability and flexibility of polysulphidic linkages, which can yield under strain and then recombine through free radical recombination in the strained state (Bateman, 1963). Antioxidants, antiozonants, and antidegradants are also necessary to put into the rubber in order to improve the chemical stability. There are other curing agents for rubber such as peroxides or metal oxides.

Table 2-1. Dissociation energy of bonds in rubber crosslinks (Baranwal and Stephens, 2001).

Bond	Dissociation energy, Kcal / mole
Alkyl-C—C-alkyl	80
Alkyl-C—S—C-alkyl	74
Alkyl-C—S—S—C-alkyl	54
Alkyl-C—S_n—S_m—C-alkyl	34

The vulcanisation characteristics are measured using a rheometer. The mechanical properties of rubber are measured against time at a given temperature. Figure 2-5 shows a typical curing curve. The resulting torque to oscillate the upper or lower die of the rheometer is measured which gives an indication of the modulus of the rubber. At the beginning, there is a time delay before the crosslinking starts. This is known as the scorch time, which is important in practical applications as it indicates the time that can be used to allow the rubber to flow into the mould before significant vulcanisation starts. The time required to reach 90% of the total torque increase is defined as t_{90}, which is a useful estimate of the overall cure rate (Dluzneski, 2001).

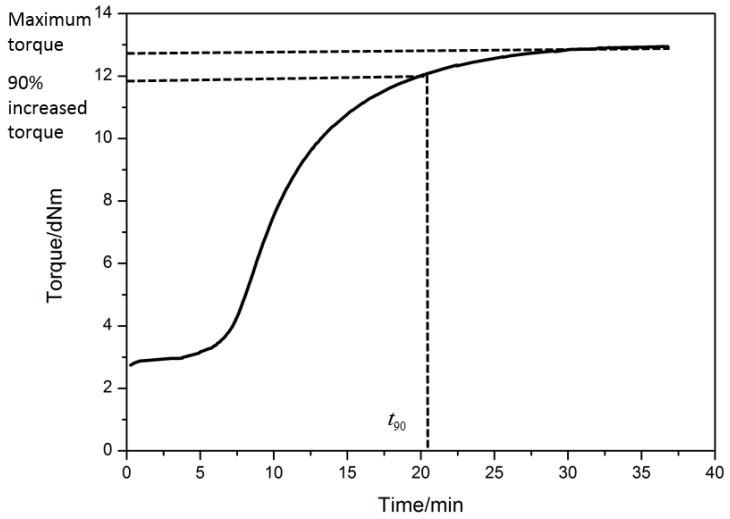

Figure 2-5. Typical curing curve for rubber, measured torque at certain strain against to time at a specific temperature.

2.4 Rubber Elasticity

Many theories have been published to explain rubber elasticity. They can be divided into two different approaches, a thermodynamic statistical theory, and a phenomenological theory. Key points of each theory are reviewed in this section.

2.4.1 Thermodynamics of Rubber

Two observations regarding the rubber thermoelastic properties of rubber were reported by Gough in 1805 (Sakulkaew, 2012). The first being that a rubber stretched under a given load shrinks upon heating. And the other being that heat is released when rubber is elongated and is absorbed when rubber is retracted to its original shape. Later Joule (1859) quantitatively re-examined Gough's findings. These two thermodynamic effects are known collectively as the Gough-Joule effects. Based on the first and second laws of thermodynamics, if the volume change is constant, $\mathrm{d}V = 0$, the elastic deformation is due to the combined changes of the internal energy and the entropy, which is expressed as (Treloar, 1975):

$$F = \left(\frac{\partial U}{\partial L}\right)_{\psi,V} - \psi\left(\frac{\partial S}{\partial L}\right)_{\psi,V} \qquad \text{Equation 2-1}$$

where F is elastic force, U is internal energy, L is the length of the rubber, V is the volume, ψ is the absolute temperature, and S is the entropy. The partial differentiation of the entropy can be expressed by:

$$\left(\frac{\partial S}{\partial L}\right)_{\psi,V} = -\left(\frac{\partial F}{\partial \psi}\right)_{L,V} \qquad \text{Equation 2-2}$$

So the elastic force can be rewritten as:

$$F = \left(\frac{\partial U}{\partial L}\right)_{\psi,V} + \psi\left(\frac{\partial F}{\partial \psi}\right)_{L,V} \qquad \text{Equation 2-3}$$

The contribution from internal energy change and entropy change can be discriminated by plotting the force versus temperature. Figure 2-6 shows the relative contribution of these two effects. Clearly, the internal energy change contribution to the rubber elasticity is minimal due to the absence of molecular geometry and intermolecular interactions (Sakulkaew, 2012).

2.4.2 Statistical Theory

The statistical approach extends the thermodynamic approach to consider the relationship between entropy changes and the molecular conformation of rubber during deformation. If there is no volume change and internal energy change on deformation, and assuming the rubber chains in the rubber network have a Gaussian distribution, the entropy is the sum of the entropies of the individual chains between each crosslink. The change in entropy for all the chains contained in unit volume of the network under deformation is obtained by (Treloar, 1975):

$$\Delta S = -\frac{1}{2} Nk\left(\lambda_1^2 + \lambda_2^2 + \lambda_3^2 - 3\right) \qquad \text{Equation 2-4}$$

where N is the number of chains per unit volume in the rubber network, k is the Boltzmann constant, λ_i are the three principal extension ratios. For a reversible deformation, the Helmholtz free energy A_H is defined as:

$$A_H = U - T_t S \qquad \text{Equation 2-5}$$

For an isothermal deformation, the work of deformation per unit volume, W , is given by:

$$W = \Delta A_H = \Delta U - T_t \Delta S \qquad \text{Equation 2-6}$$

Hence, W represents the elastic stored energy function (SEF) is expressed as:

$$W = \frac{1}{2} NkT_t \left(\lambda_1^2 + \lambda_2^2 + \lambda_3^2 - 3 \right) \qquad \text{Equation 2-7}$$

where:

$$NkT = \rho R_{gas} T_t / M_c = G \qquad \text{Equation 2-8}$$

where G is a physical constant known as the shear modulus, ρ is the density, R_{gas} is the gas constant, and M_c is the average chain molecular weight between crosslinks. The SEF derived from statistical elasticity is called the Neo-Hookean SEF. One limitation for the thermodynamically based statistical approach is that it only works at small and modest strains. At larger strains additional contributions to the applied stress such as finite network extensibility and strain-induced crystallisation take place and are not included in the theory (Tunnicliffe, 2015).

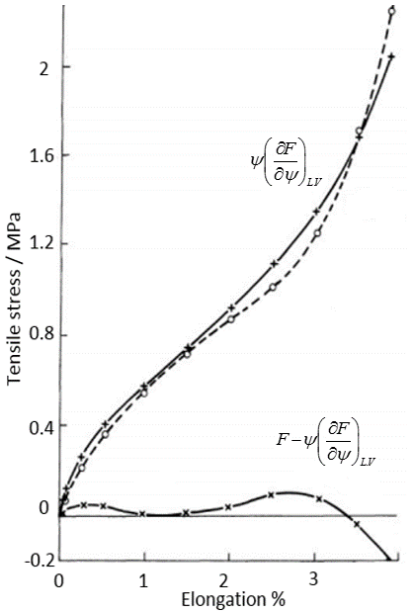

Figure 2-6. The stress-elongation curve of natural rubber cured with sulphur deconvoluted into internal energy contribution and entropy contribution using Equation 2-3 (Treloar, 1975).

2.4.3 Phenomenological Theory

The last theory for rubber elasticity is the phenomenological approach, which utilises continuum mechanics to derive a strain energy function to match the stress-strain behaviour. Mooney (1940) was the first one to derive a strain energy function W of the rubber materials under the assumption that rubber is an incompressible and isotropic material in the unstrained state. The strain energy function can be shown as:

$$W = C_1(I_1 - 3) + C_2(I_2 - 3) \qquad \text{Equation 2-9}$$

where C_1 and C_2 are material constants, and I_1 and I_2 are strain invariants defined as:

$$I_1 = \lambda_1^2 + \lambda_2^2 + \lambda_3^2 \qquad \text{Equation 2-10}$$

$$I_2 = \lambda_1^2\lambda_2^2 + \lambda_1^2\lambda_3^2 + \lambda_2^2\lambda_3^2 = \lambda_1^{-2} + \lambda_2^{-2} + \lambda_3^{-2} \qquad \text{Equation 2-11}$$

The Mooney SEF can be simplified to the Neo-Hookean function, when $C_1 = G/2$ and $C_2 = 0$.Rivlin (1948) further developed Mooney approach and showed that the SEF can be expressed as an infinite power series:

$$W = \sum_{i=0,\, j=0}^{\infty} C_{ij}(I_1 - 3)^i (I_2 - 3)^j \qquad \text{Equation 2-12}$$

Equation 2-12 is usually truncated to the first few terms. When only the first term ($i = 1$ and $j = 0$) is adopted, the Neo-Hookean SEF is obtained. The Mooney SEF is derived when applying the first two terms ($i = 1$ and $j = 1$).

2.4.4 Viscoelasticity

A typical stress-strain curve when applying a force to extend a piece of rubber and then during the removal phase so that the material returns to its original shape is shown in Figure 2-7. Clearly the material is not perfectly elastic and the unloading curve does not follow the loading path. Less energy is recovered during the rubber's return to its original state than was required to make the initial extension. The amount of energy equivalent to the area in the loop formed by the two curves is dissipated into heat. This energy conversion is known as hysteresis, and it is a consequence of the viscous damping

component of the rubber. Therefore, in reality rubber is viscoelastic materials and both elastic and viscous behaviour contribute to the observed mechanical properties (Ciesielski, 1999).

As a result, rubber always exhibit a time dependent mechanical response which can be observed as phenomena such as stress relaxation and creep behaviour. Stress relaxation takes place when rubber is deformed to a fixed displacement where the stress decreases gradually with time. Creep is a behaviour that the deformation increases under a constant load (Liang, 2007). The viscoelasticity can be visualised as a combination of two separate mechanisms occurring at the same time in rubber, using a spring represents the elastic portion and a dashpot represents the viscous component. Two classical viscoelasticity models can be used to define the basic viscoelastic elements known as either a Maxwell or a Voigt model (Ciesielski, 1999) as shown in Figure 2-8. The constitutive equation for a Maxwell models is:

$$\frac{\mathrm{d}\varepsilon}{\mathrm{d}t} = \frac{1}{E}\frac{\mathrm{d}\sigma}{\mathrm{d}t} + \frac{\sigma}{\eta_e} \qquad \text{Equation 2-13}$$

and for a Voigt model is:

$$\sigma(t) = \varepsilon(t) + \eta_e \frac{\mathrm{d}\varepsilon(t)}{\mathrm{d}t} \qquad \text{Equation 2-14}$$

where σ is the stress, ε is the strain, E is the elastic modulus, η_e is the viscosity coefficient and t is the time.

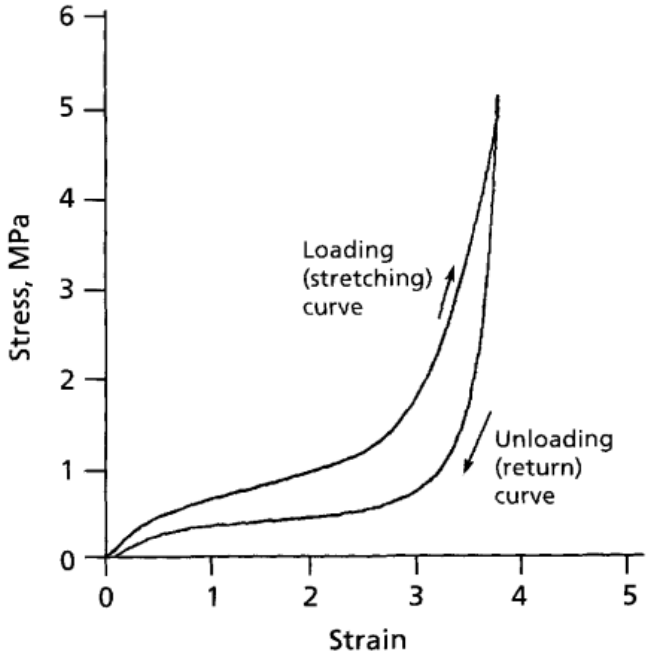

Figure 2-7. A tensile stress-strain loading and unloading curve at the sixth cycle (Ciesielski, 1999).

When a sinusoidal shear stress is imposed periodically on a rubber material at a frequency ω, the strain will also alternate sinusoidally but will be out of phase, the strain lagging the stress as shown in Figure 2-9. The shear strain γ and stress σ can be expressed as (Wang, 1998):

$$\gamma = \gamma_0 \sin \omega t \qquad \text{Equation 2-15}$$

and

$$\sigma = \sigma_0 \sin\left(\omega t + \delta\right) \qquad \text{Equation 2-16}$$

where δ is the phase angle between stress and strain, and γ_0 and σ_0 are the maximum amplitude of strain and stress, respectively. The equation can be further expanded into two components, the part that is in-phase and the part that is out-phase with strain:

$$\sigma = \sigma_0 \sin \omega t \cos \delta + \sigma_0 \cos \omega t \sin \delta \qquad \text{Equation 2-17}$$

Thus, the dynamic stress-strain behaviour can be represented by an in-phase modulus G' (elastic modulus or storage modulus), and an out-phase modulus G'' (viscous modulus and loss modulus):

$$\sigma = \gamma_0 G' \sin \omega t + \gamma_0 G'' \cos \omega t \qquad \text{Equation 2-18}$$

with

$$G' = \left(\sigma_0 / \gamma_0\right) \cos \delta \qquad \text{Equation 2-19}$$

and

$$G'' = \left(\sigma_0 / \gamma_0\right) \sin \delta \qquad \text{Equation 2-20}$$

The phase angle, δ, is viscoelastic characteristic for rubber materials (0° for ideal elastic material and 90° for ideal viscous material). The loss tangent is defined as:

$$\tan \delta = \frac{G''}{G'} \qquad \text{Equation 2-21}$$

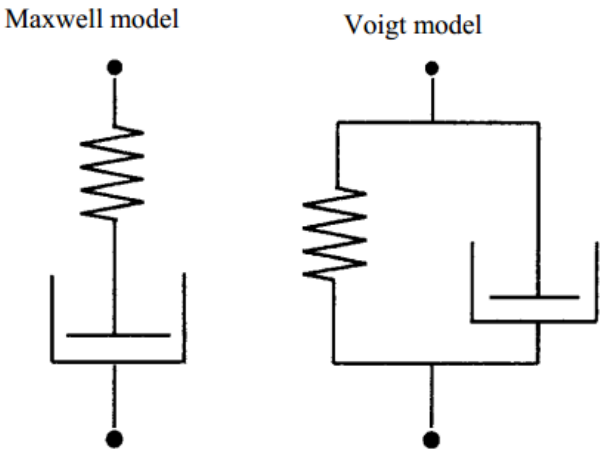

Figure 2-8. Models of viscoelastic materials, Maxwell and Voigt model (Ciesielski, 1999).

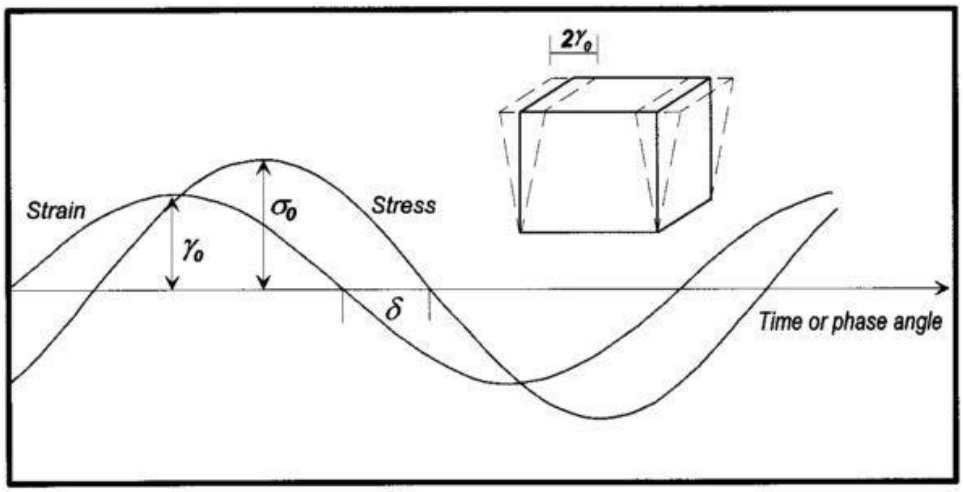

Figure 2-9. Sinusoidal stress and strain correspondence (Wang, 1998).

Both storage modulus and loss modulus are a function of time and temperature. Figure 2-10 shows the temperature sweep result of an unfilled rubber using Dynamic Mechanical Analysis (DMA) at 0.1% strain and 1Hz. However, it is very difficult to perform a frequency sweep experiment due to the limitation of the machine. Fortunately, the Time-Temperature Superposition (TTS) allows us to get a master curve for a very large frequency range. Williams, Landel and Ferry (WLF) (1955) derived an equation to calculate the temperature dependent shift factor a_T :

$$\log_{10} a_T = \frac{-C_{W1}(T - T_S)}{C_{W2} + T - T_s} \qquad \text{Equation 2-22}$$

where T is the test temperature and T_s is a reference temperature. C_{W1} and C_{W2} are constants and T_s is the reference temperature defined as:

$$T_s = T_g + 50°C \qquad \text{Equation 2-23}$$

Examples for the frequency sweep master curve for unvulcanised rubber and vulcanised filled rubber blend are shown in Figure 2-11 and Figure 2-12. Both G' and G'' are measured at different frequencies over a range of temperatures. A horizontal shift of the curves at different temperature is applied to generate the master curve. The formation of master curve for filled rubber is less reliable due to the temperature dependent filler-polymer interactions. In order to obtain a good master curve for filled rubber an additional vertical shift is also necessary.

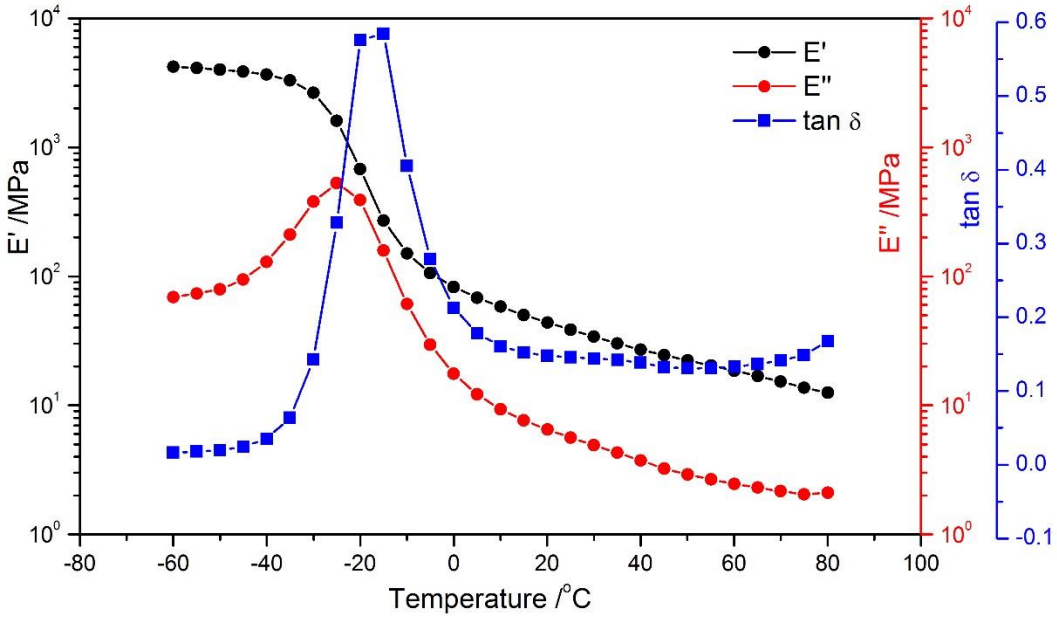

Figure 2-10. Dynamic mechanical properties of carbon black filled SBR as a function of temperature.

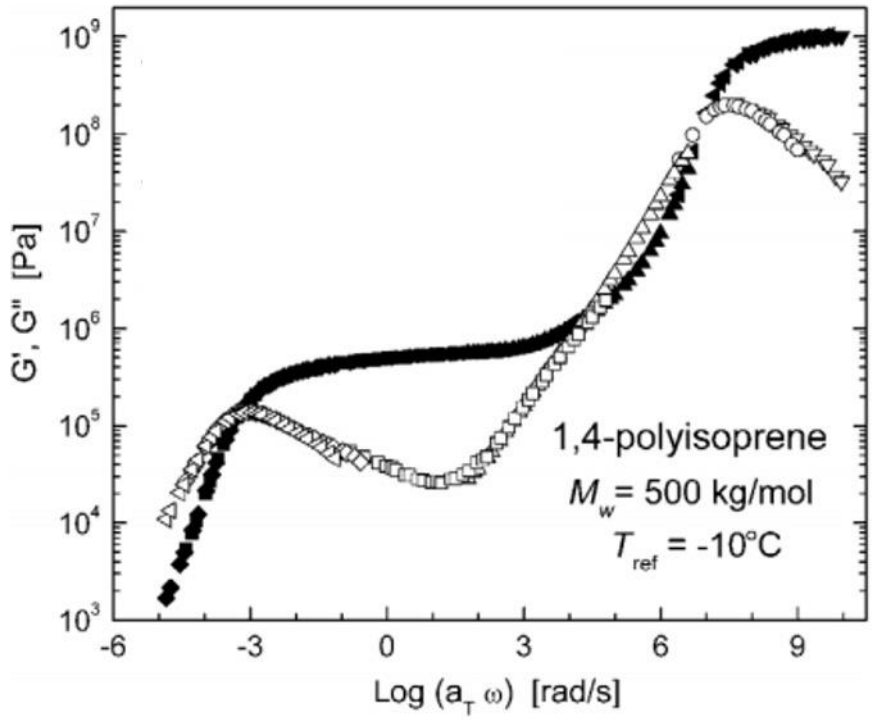

Figure 2-11. Example of frequency master curve for an uncured polyisoprene rubber (Mark et al., 2013).

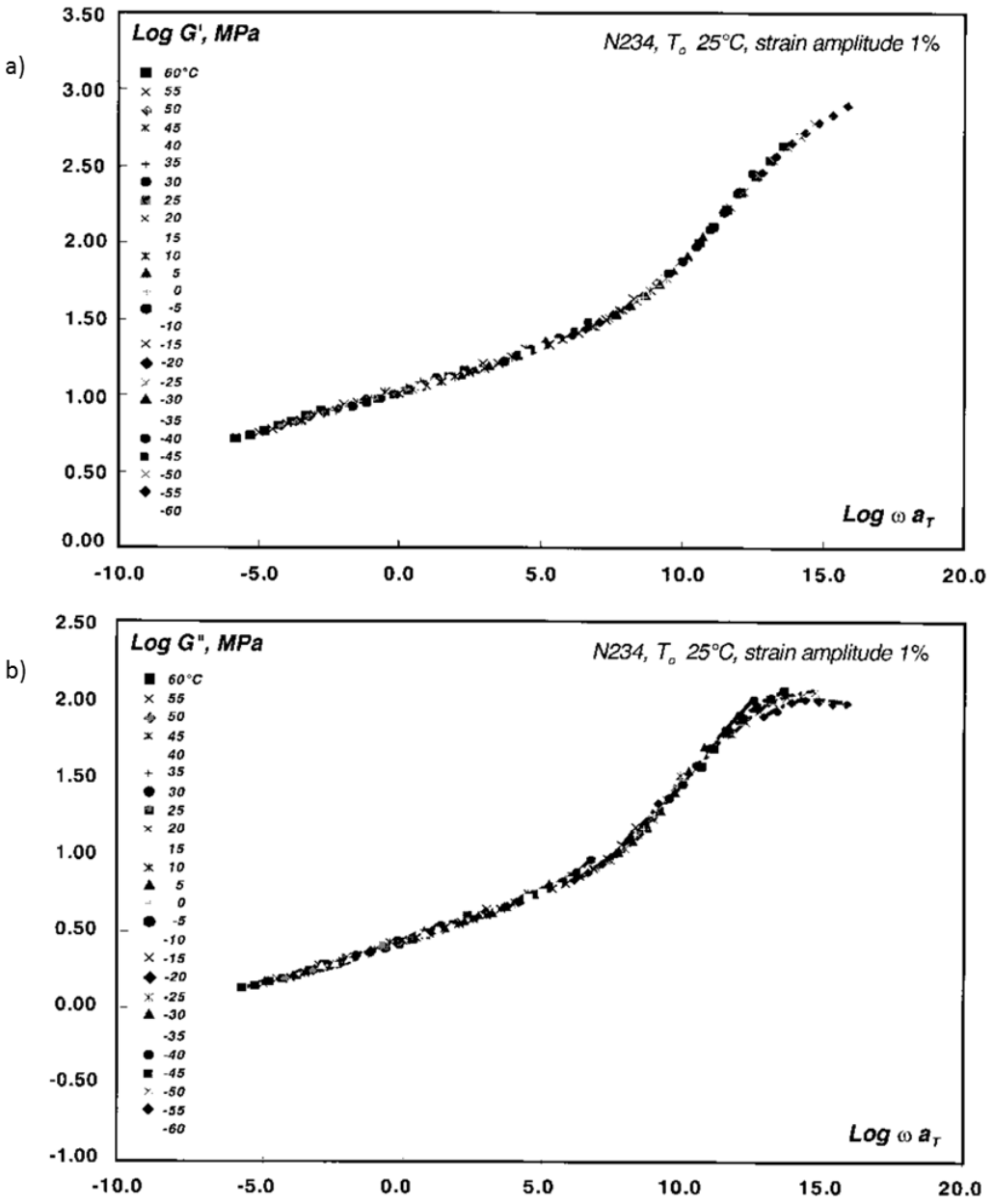

Figure 2-12. Example of frequency master curve for a cured N234 filled SBR and BR blend, a) G' and b) G'' (Wang et al., 2000).

2.5 Filler and Filler Reinforcement

Typically most rubber products are reinforced with particulate filler to enhance the final mechanical properties such as tensile strength or tear resistance. Various fillers with different type, size, structure, and surface area and activity, are available in the rubber industry. The most common fillers are carbon black and precipitated silica.

2.5.1 Carbon Black

Carbon black is produced by incomplete combustion of vaporised hydrocarbons under strictly controlled conditions. The chemical structure of carbon black at different scales is given in Figure 2-13. The carbon black used in rubber industry has a primary size between 10 to 100 nm (Donnet, 1993). Owing to the high surface energy and high aspect ratio, these primary carbon black particles tend to attach to each other and form carbon black aggregates, which is the smallest unit they are encountered in a rubber matrix. Different carbon blacks even if they have similar sized aggregates may have different geometric complexity. This property is known as the filler's structure. The filler aggregates properties therefore depend upon the primary particle size, the number of particles in the aggregate and also the filler structure. Various techniques can be used to characterise the morphological properties of carbon black such as Transmission Electron Microscope (TEM) for primary particle size, Brunauer, Emmett, and Teller (BET) nitrogen adsorption and cetyltrimethyl ammonium bromide (CTAB) adsorption for surface area, and di(*n*-dibutyl) phthalate absorption (DBPA) for filler structure. A cluster of filler aggregates is then also known as a filler agglomerate (Huang, 2015).

2.5.2 Precipitated Silica

Precipitated silica is an amorphous silica produced by acidification of sodium silicate under controlled conditions (Tunnicliffe, 2015). Unlike carbon black which has various grades, precipitated silica can be divided into two categories: conventional silica and highly dispersible silica. Highly dispersible silica has a similar morphology and surface area as carbon black and is generally used in tyre industry. However, the surface chemistry of silica is different compared to carbon black. The surface of silica is presented with polar hydroxyl (silanol) groups as shown in Figure 2-14 (Luginsland, 2002a). And also a moisture "shell" surrounds the silica surface by hydrogen bonding due to the production process. Therefore, silica with high polar surface is less compatible with most of non-polar diene rubber, which results in less filler-polymer interaction and worse micro and macro scale filler dispersion. This can in part be overcome by using an organosilane dispersing and coupling agent to modify the surface of the silica (Luginsland, 2002a).

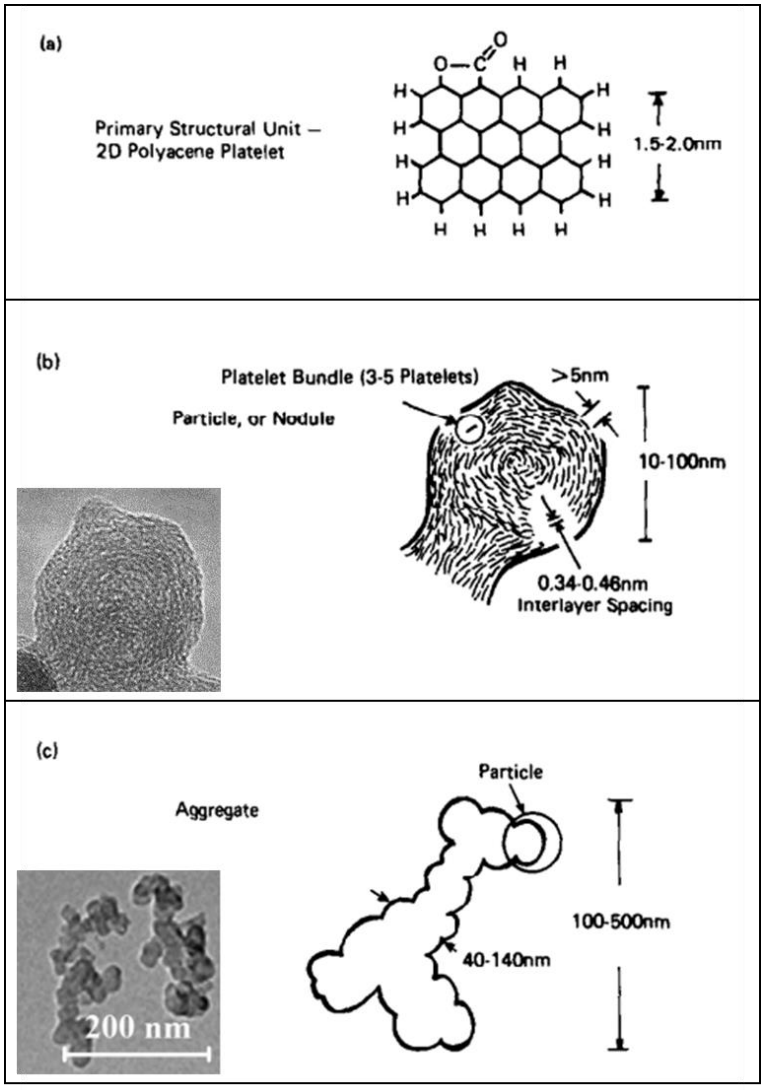

Figure 2-13. The structure of carbon black at different length scales (a) 2D carbon platelet (b) primary particle. The inset is a SEM image for N285 primary particle. (c) carbon black aggregate. The inset is a TEM image for N134 aggregate (Huang, 2015).

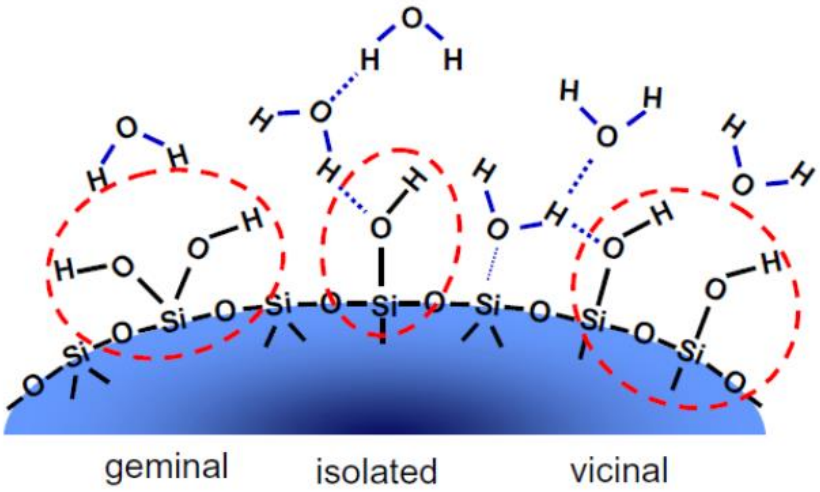

Figure 2-14. Silanol groups present on the precipitated silica surface (Luginsland, 2002b).

2.5.3 Filler Reinforcement

The mechanisms of filler reinforcement are complex and are still a topic of significant debate in the academic literature. The various mechanisms proposed include the hydrodynamic effect (Einstein, 1906, Smallwood, 1945, Guth, 1945), the bound rubber and the occluded rubber effect (Medalia, 1970, Medalia, 1972, Dannenberg, 1986, Wolff et al., 1993, Wang, 1998), the strain amplification effect (Bergstrom and Boyce, 1999, Austrell and Kari, 2005, Akutagawa et al., 2008), the filler network effect (Fletcher and Gent, 1953, Fletcher and Gent, 1954, Payne, 1963, Payne and Whittaker, 1971), and the effect of modified polymer dynamics at the interface (Smit, 1966, O'brien et al., 1976, Berriot et al., 2002, Fragiadakis et al., 2011). One simple way to illustrate the reinforcing mechanisms is to examine the Payne effect as shown in Figure 2-15. The increases in the shear modulus can be split into a linear combination of hydrodynamic, fill-polymer interaction (bound rubber, occluded rubber and strain amplification), and filler-filler interaction (filler network). The Payne effect also shows the non-linear viscoelasticity of rubber at large strains.

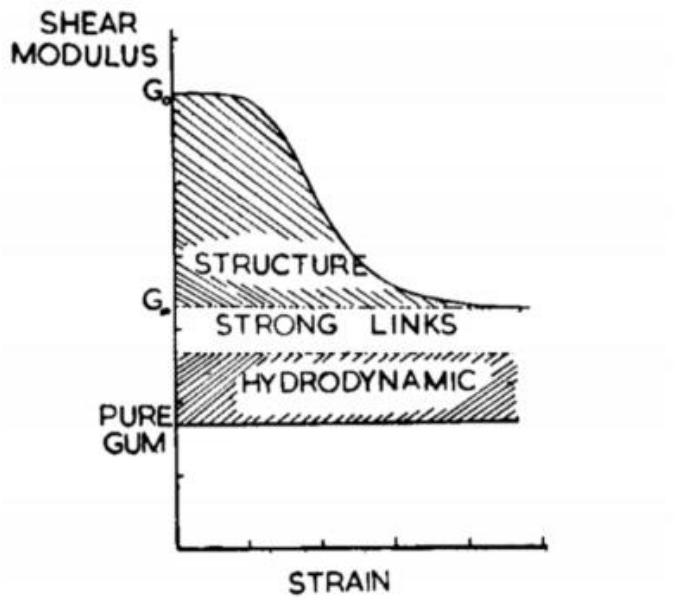

Figure 2-15. Dynamic non-linear viscoelasticity for filled rubber at small strain.(Payne, 1963).

2.6 Fracture Mechanics for Rubber Materials

It is of importance to develop a method to assess the strength of rubber components, whether in a single loading or when subjected to cyclic fatigue type loading. Rivlin and Thomas (Rivlin and Thomas, 1953) firstly developed the theory for crack growth in rubber from the Griffith (1921) energy criterion for brittle materials. This approach considers the irreversible energy dissipation which happens in the highly strained regions in the neighbourhood of the crack tip. The magnitude of these losses depends on the viscoelastic properties of rubber materials, the strain in the crack tip region of a given size and the crack growth rate. The energy required to drive the crack is known as tearing energy, T is given as:

$$T = -\left(\frac{\partial U}{\partial A_s}\right)_l \qquad \text{Equation 2-24}$$

where suffix l denotes the differentiation with constant displacement of the boundaries, U is elastic stored energy, and A_s is the area of fracture surface of the crack. The tearing energy is a characteristic property of a specific rubber material and it is independent of the form of test pieces (Rivlin and Thomas, 1953, Thomas, 1960, Lake et al., 1969).

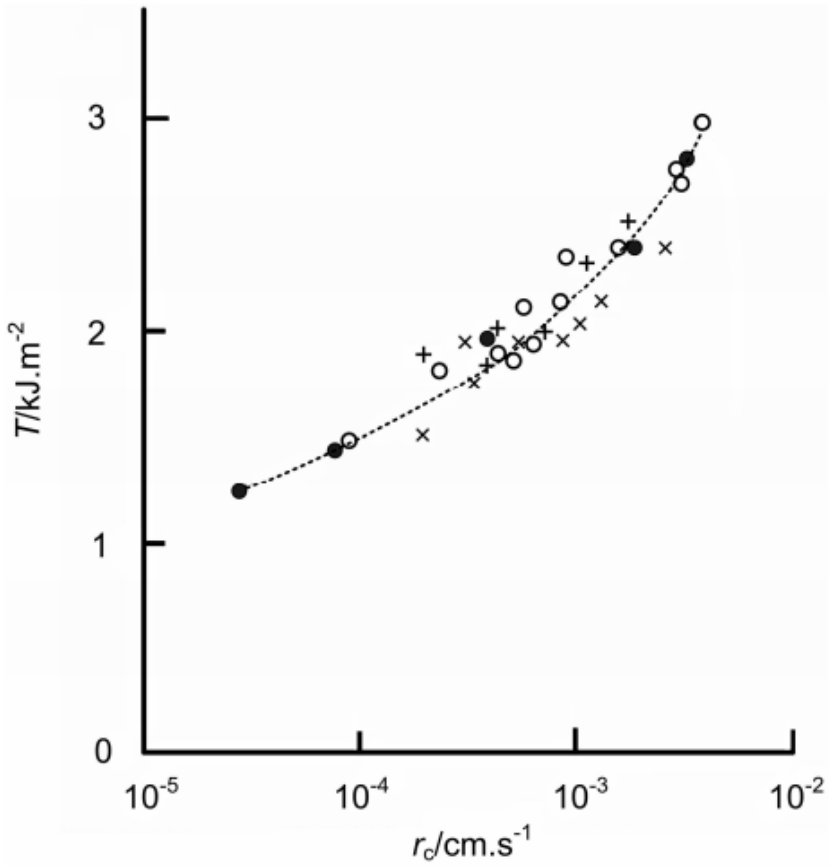

Figure 2-16. The tearing energy determined by various test configurations. Trouser tear: x; pure shear: +; angled: •; and split: o (Lake et al., 1969).

Figure 2-16 shows a plot of the tearing energy against the tearing rate for unfilled SBR measured using various different geometrical configurations. It is clear that a constant tearing energy independent of the specimen geometry can be obtained. The principle being that for a non-linear elastic material, the energy dissipation due to tearing is dependent on the physical properties of the material and not on the geometry of the test piece. The tearing energy should provide a true measure of the tear resistance independent of the geometry of the test piece and of the way the forces are applied (Liang, 2007).

When rubber materials are under cyclic loading or deformation, the materials fail at cyclic strain amplitude much lower than their catastrophic tear strength because of cumulative cyclic fatigue growth. Lindley and Thomas (1962) found that the extent of crack growth per cycle is determined by the maximum value of the tearing energy during

the loading cycle, when the specimen is fully relaxed in each loading cycle. Therefore, the crack growth per cycle can be represented as:

$$\frac{\mathrm{d}c}{\mathrm{d}n} = f\left(T\right) \qquad \text{Equation 2-25}$$

where c is the crack length, n is the number of cycles and T is the maximum tearing energy during a cycle.

A typical graph of the rate of fatigue crack growth per cycle against the tearing energy on a double logarithmic scale is shown in Figure 2-17. The figure is easy to divide into three regions with an additional fourth type of behaviour at the highest value of T. The crack growth rate can be fitted by particular equations in each region (Lake, 1983).

In region I, where the tearing energy is below a threshold T_0, which is the minimum tearing energy at which mechanical crack growth can occur (Lake and Thomas, 1967). Consequently, there is no relationship between the crack growth rate and the tearing energy. The crack growth is dominated by chemical processes, the most active of which is ozone attack. Thus, the crack growth rate can be represented by the ozone concentration as:

$$\frac{\mathrm{d}c}{\mathrm{d}n} = k_Z\left[O_3\right] \qquad \text{Equation 2-26}$$

where $\left[O_3\right]$ is the concentration of ozone, k_Z is a constant.

Region II is a transition range. There is a linear relationship between the crack growth rate and the tearing energy shown as:

$$\frac{\mathrm{d}c}{\mathrm{d}n} = R_Z + A_t\left(T - T_0\right) \qquad \text{Equation 2-27}$$

where A_t is crack growth constant for region II.

In region III, there is a power relationship, which corresponds most closely with crack growth rates found in the engineering fatigue range or during abrasion processes. This region can be represented by a power law relationship, given by:

$$\frac{\mathrm{d}c}{\mathrm{d}n} = B_t \left(\frac{T}{T_u} \right)^{\beta} \qquad \text{Equation 2-28}$$

where B_t and β are rubber crack growth parameters, characteristic for region III. T_u is introduced to make the equation dimensionless with the value being set as 1 Jm^{-2}.

The final region is the catastrophic failure region. The tearing energy is higher than T_c, above which failure would happen in one cycle.

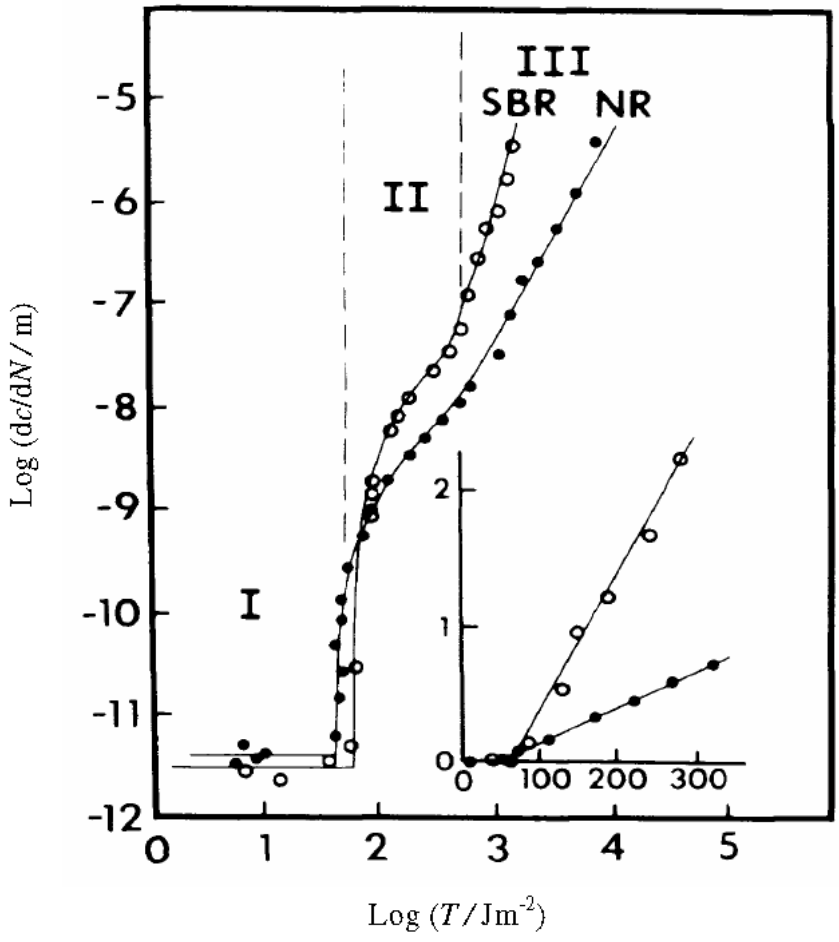

Figure 2-17. The crack growth per cycle as a function of tearing energy in a double logarithmic scale. The inset shows the region near the threshold tearing energy, plotted in a linear scale (Lake, 1983).

The test temperature also has a significant effect on fatigue crack growth, especially for non-strain-crystallizing rubbers, whose strength are derived from their viscoelasticity and hence their proximity to the glass transition temperature (Gent, 2012). A 10^4 fold decrease in fatigue life is observed for an unfilled SBR on raising its test temperature from 0 to 100 °C, in contrast to unfilled NR, which only shows a fourfold decrease (Lake and Lindley, 1964).

2.7 Rubber Friction

For most of the solid materials, the friction under dry conditions follows Amontons' laws and Coulomb's laws. The three resulting laws can be summarised as (Gabriel, 2010):

1. The friction force F_F in directly proportional to the normal load F_N.
2. The friction force F_F is independent of the apparent contact area.
3. Kinetic friction is independent of the sliding velocity.

However, for rubber materials, they do not obey these friction laws due to its viscoelastic nature particularly its low elastic modulus and the high internal friction over a wide range of frequencies (Persson, 1998). Different factors contribute to the total friction for rubber materials. For dry conditions, two components contribute to the final friction:

$$F_F = F_{ad} + F_{def} \qquad \text{Equation 2-29}$$

where F_{ad} is the adhesion term resulting from adhesion between the elastomer and the mating contact surface, F_{def} is the deformation term or hysteresis contribution due to the viscoelastic energy dissipation (Grosch, 1963). The adhesion friction mainly dominates the rubber friction for very smooth contact situations (Roberts and Thomas, 1975). In contrast, adhesion is almost negligible for rough interfaces and the deformation term is the major contribution to the frictional force (Persson, 2001).

Rubber friction is temperature and velocity dependent because of its viscoelastic nature. Grosch (1963) investigated rubber friction in a large range of temperatures and velocities. The friction coefficient is plotted against the sliding velocity under various

temperatures as shown in Figure 2-18. Figure 2-18 can also be horizontally shifted using TTS as described in section 2.6 to form a master curve The velocity dependence of the friction coefficient at a constant temperature over a large velocity range is shown in Figure 2-19. The position of the peak in Figure 2-19 is empirically related to dynamic properties of the rubber, where velocity correlates to the frequency at which the mechanical loss angle has its maximum. The construction of the master curve for friction is only valid as long as sliding velocities are low enough for frictional temperature rises to be negligible (Schallamach, 1968b).

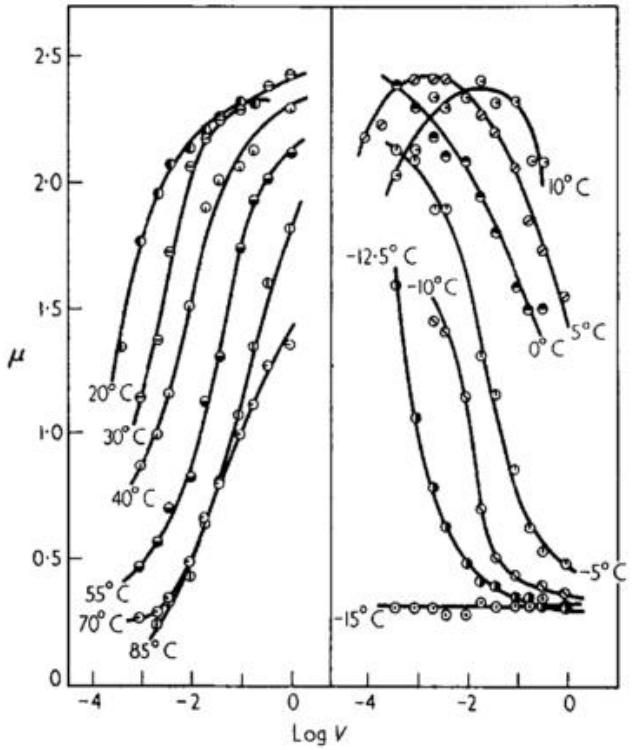

Figure 2-18. Friction coefficient of pin-head glass on unfilled acrylonitrile-butadiene rubber at various temperatures and velocity (Grosch, 1963).

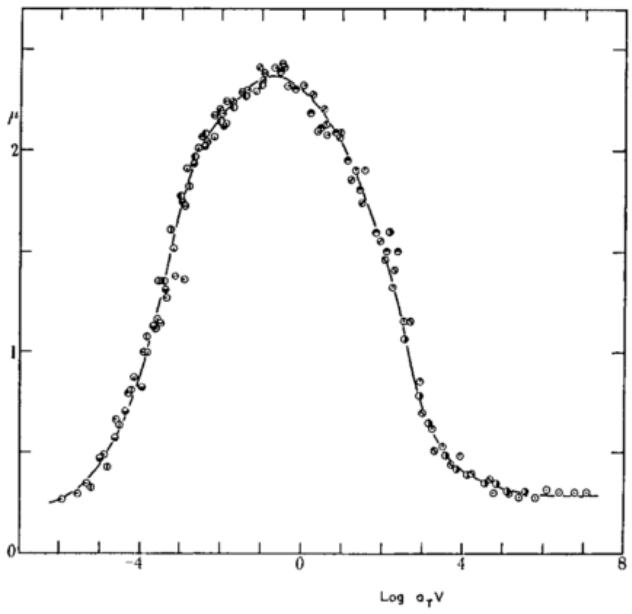

Figure 2-19. Master curve for coefficient of friction of acrylonitrile-butadiene rubber against velocity at 20°C derived from Figure 2-18 (Grosch, 1963).

2.8 Summary

The basic knowledge of rubber materials is briefly reviewed in this chapter. This is essential to investigate the abrasion behaviour of rubbers. Due to its own characteristics as described in this chapter, rubber materials exhibit a complicated range of abrasion phenomena when compared to other hard materials. A literature review of the rubber abrasion is given in the next chapter.

3 Chapter Three: Rubber Abrasion

3.1 Introduction

The word 'abrasion' is defined in the Oxford English Dictionary (Soanes and Stevenson, 2004) as 'damage to a surface caused by rubbing something very hard against it'. For most materials, 'abrasion' is a phenomenon of scoring by hard and sharp asperities which results in a purely mechanical failure. However, for rubber materials, abrasion may not only result from mechanical fracture but also variety of other mechanisms (Gent and Pulford, 1983, Muhr and Roberts, 1992). Thus, rubber abrasion is a complex process that has mechanical, thermal, and chemical contributions (Moore, 1972). The term 'wear' can be used interchangeably with 'abrasion' for rubber materials, although in practice 'wear' is used for real applications and 'abrasion' typically denotes laboratory testing (Arayapranee, 2012).

Abrasion frequently arises in rubber applications such as shoe soles, tyre treads, conveyer belts, and annular blow-out preventers that seal oil drilling pipes. It is one of the most important properties for a rubber material, as it often determines a product's life expectancy. Failure due to abrasion can be disastrous, for example, driving a car with insufficient tyre tread depth can result in either the tyre bursting or skidding off the road. Wear failure of a blow-out preventer results in the uncontrolled loss of crude oil at the seabed, resulting in disastrous environmental pollution and tremendous economic loss. Therefore, abrasion resistance is a primarily concern when designing rubber products.

In order to satisfy the design requirements for real products it is often necessary to predict the abrasion rate. This requires extensive laboratory testing which can only correlate to the actual performance of the products, if the laboratory conditions map onto the loading that is encountered in service. To make these predictions requires an extensive knowledge of the basic mechanisms of rubber abrasion. However, as has already mentioned, rubber abrasion is a complex behaviour and the fundamental mechanisms are still not fully understood. In addition, various factors, including the detailed rubber formulations and the detailed test conditions all have an effect on

abrasion behaviour. Different polymers in different formulations have different fracture properties and then when compounded as a composite incorporating fillers the problem is made even more complex as the fillers significantly alter the mechanical properties. The detailed test conditions also may include the sliding velocity, slip ratio, temperature, contact surface profile, lubrication and environmental atmosphere all of which serve to make this topic even more challenging. Over the past 60 years, many researchers have investigated rubber abrasion and many different laboratory based abrasion tests have been developed. This has allowed some understanding of the various abrasion mechanisms to be revealed but the complete picture is still not clear. A detailed literature review on this topic is given in this chapter.

3.2 Abrasive Wear

Different abrasion mechanisms operate under different conditions. It has been demonstrated that when rubber slides against surfaces containing sharp asperities, abrasive wear is the dominant abrasion mechanism. Stress concentrations generated by the sharp points of contact cut into the rubber which can then reach the limiting strength of the material and micro-cutting or scratching is observed on the rubber surface. This produces longitudinal scratches which are parallel to the sliding direction and which are known as score line as shown in Figure 3-1. Abrasive wear is caused by tensile failure, which normally produces large amounts of weight loss. In this case, rubber abrasion is very similar to the abrasion of hard materials such as plastics and metals.

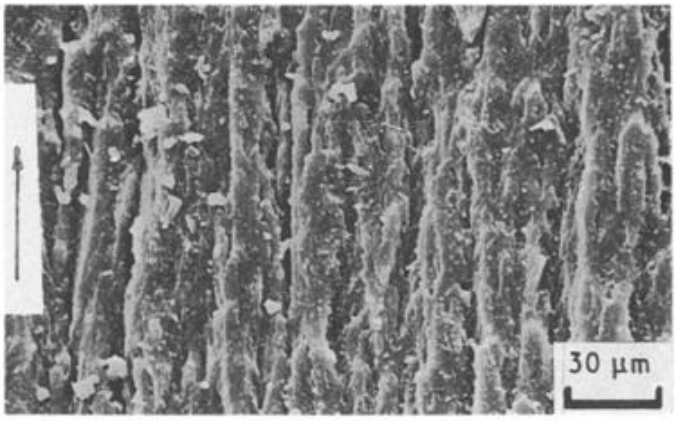

Figure 3-1. SEM image of rubber surface under abrasive wear, the arrow shows the sliding direction (Thavamani and Bhowmick, 1993).

Schallamach (1952) first investigated this type of abrasive wear of rubber from a scientific point of view. A needle was used to scratch against rubber surfaces under various different conditions of normal loading and sliding velocities. A series of discontinued periodic needle traces were generated on the rubber surface as shown in Figure 3-2. Although the materials loss is little from just one needle, there is clearly significant surface damage generated due to catastrophic tearing behind the needle. The formation of these grooves was further explained in Figure 3-3 (Schallamach, 1958). The curves shown were originally equidistant reference lines, which were marked perpendicular to the direction of sliding. The distortion of these curves showed the strain distribution and stress concentration around the needle tip. Even though the largest stress was initiated at the front of needle, no failure occurred owing to the frictional adherence. Instead, rubber tore at the point where it first loses contact with the needle.

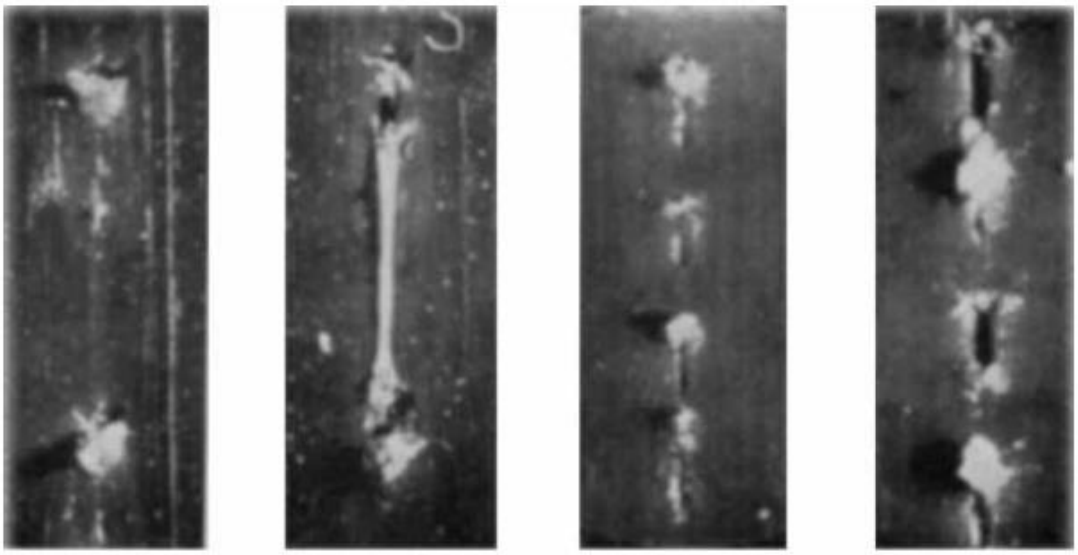

Figure 3-2. Needle trace on various rubber surface with different load (Schallamach, 1952).

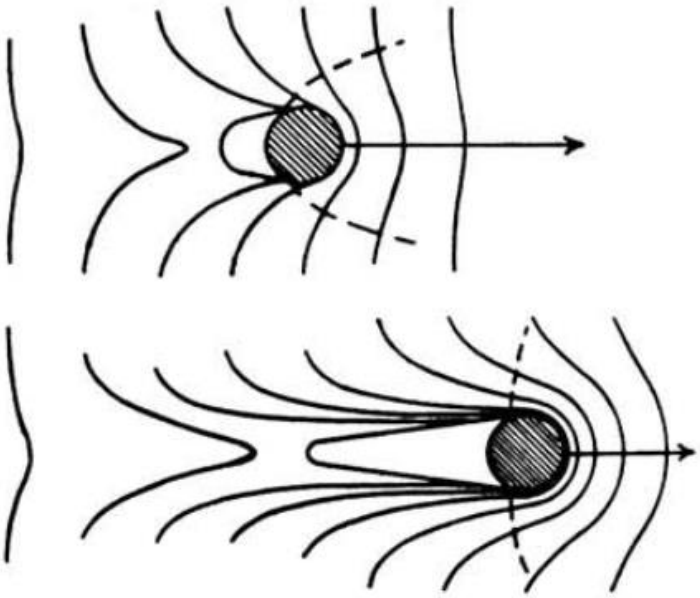

Figure 3-3. Schematic representation of stress concentration and strain distribution on the rubber surface around the tip of the needle (Schallamach, 1958).

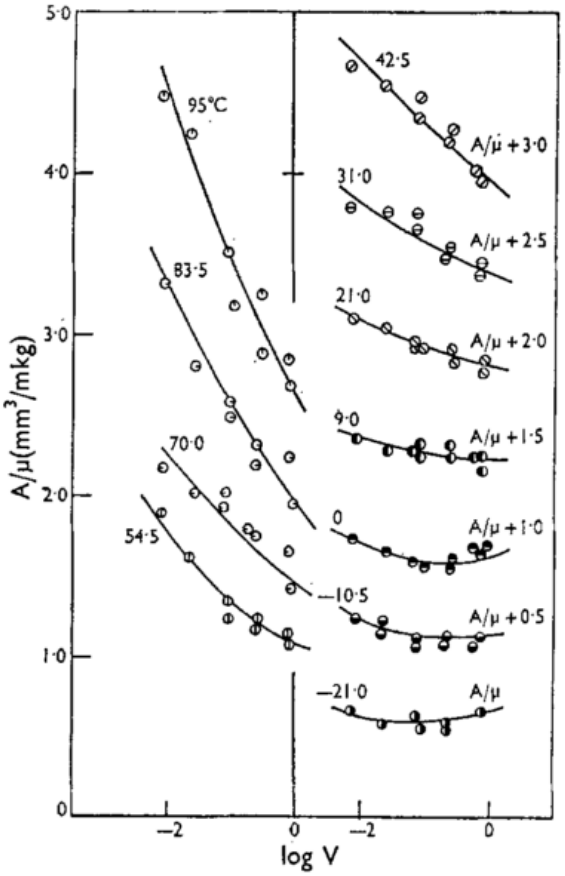

Figure 3-4. Abradability as a function of sliding velocity at various temperatures. (Grosch and Schallamach, 1966).

In order to generate a measurable amount of abrasion loss, instead of using just a single point of contact, researchers applied multiple surface contacts with sharp asperities such as that encountered when abrading with silicon carbide paper. Abrasion of rubber sliding on a silicon carbide abrasive paper at a large temperature range with variable velocities was carried out by various researchers (Grosch and Schallamach, 1966), an example of which is shown in Figure 3-4.

The rubber volume abraded per unit normal load and unit sliding distance was defined as abrasion coefficient A and A/μ was a load-independent ratio defined as the abradability. The abradability of a non-filled SBR compound as a function of the logarithm of sliding velocity at different temperature is given in Figure 3-4. The family of curves were very similar to the friction coefficient measured under different velocities and temperatures. This allowed the abradability curves to be transformed into one continuous 'master curve' using a WLF time-temperature superposition. The master curve is plotted in Figure 3-5 where the resulting master curve is compared with that measured for another two rubber compounds.

The values of Standard Reference Temperature T_S derived from the abrasion data correlated well with values derived by measuring other viscoelastic properties. This suggested that the rate of abrasive wear was essentially determined by viscoelastic processes. If this were true, then the abradability should be proportional to the reciprocal of energy density at break $1/U_b$. In order to validate this, tensile tests measured at a similar strain rate to that of rubber abrasion process were performed. A home-built tension machine was developed by Grosch and Schallamach (1966) to match the strain rate encountered during abrasion. There was an excellent agreement between the A/μ measured in abrasion and $1/U_b$ taken from the tensile testing as shown in Figure 3-6. This confirmed that the abrasive wear resulted from the tensile failure. Thavamani and Bhowmick (1993) used a modified Du Pont Abrader to study the wear behaviour of HNBR. It was found that the abrasion loss increased with a decrease in crosslinking density and increased with temperature. That was partially due to a

decrease in the strength and the energy at break, which confirmed the abradability increased linearly with reciprocal of breaking energy.

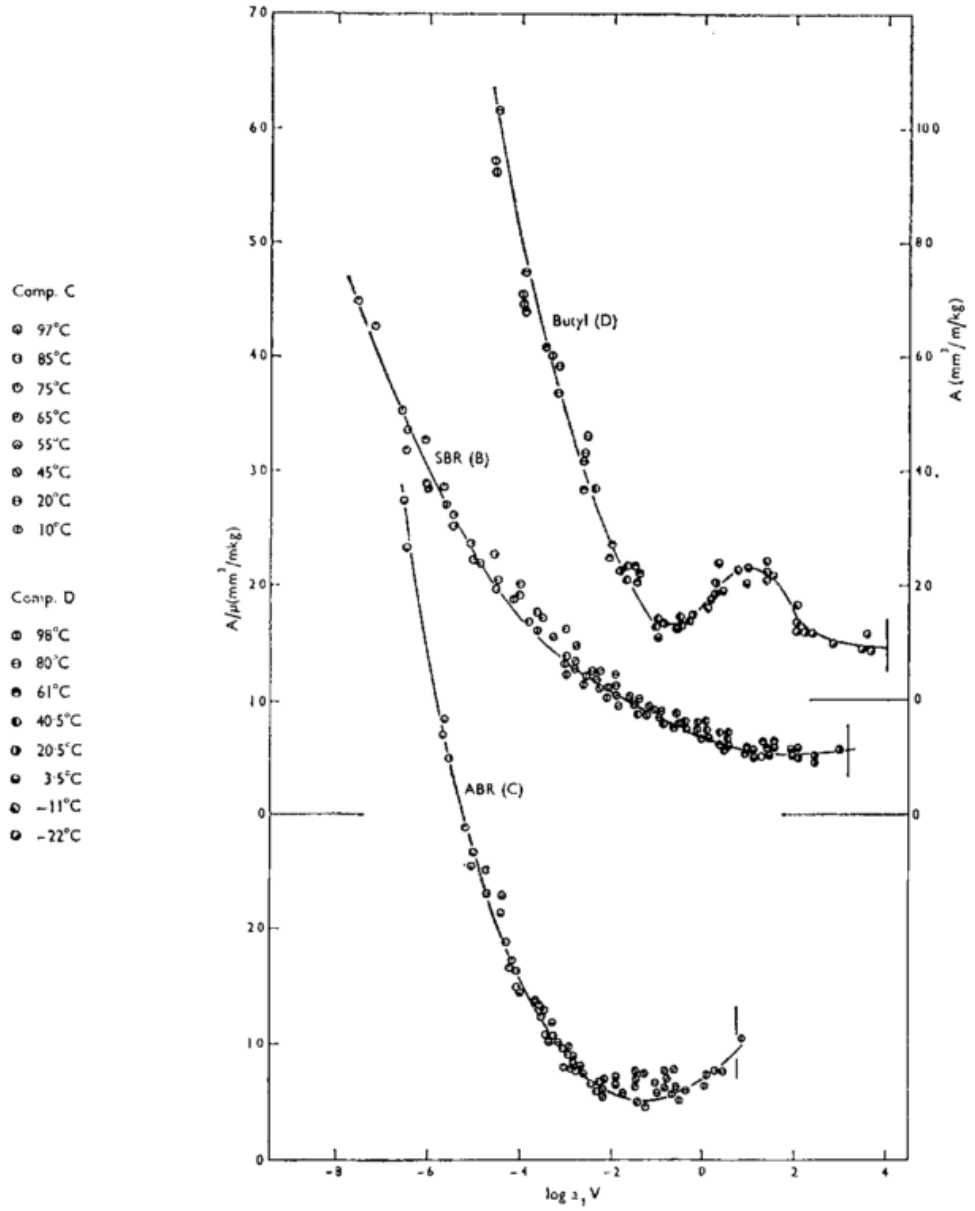

Figure 3-5. Master curve of abradability as a function of sliding velocity (Grosch and Schallamach, 1966).

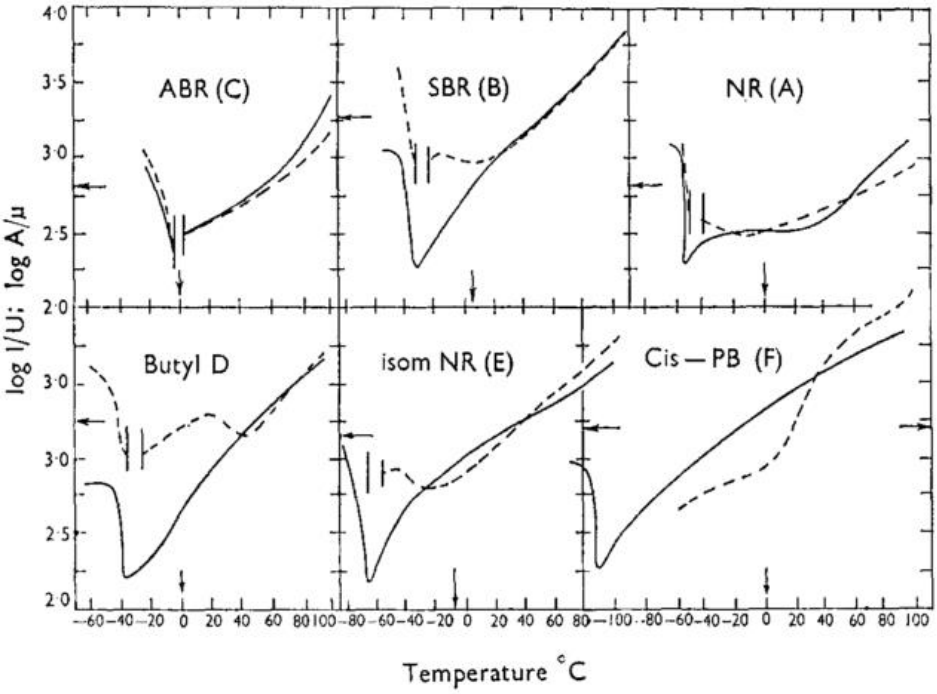

Figure 3-6. Abradability (broken lines) and reciprocal of energy density at break (solid lines) as a function of temperature for six different types of rubber (Grosch and Schallamach, 1966).

3.3 Fatigue Wear

When rubber materials slide against smooth rigid abrasives, the stress concentrations are much lower generating a fatigue failure rather than tensile failure to remove wear particles. Therefore, the abrasion of rubber caused by this failure mode is called fatigue wear or adhesion wear. In the conditions of uniaxial sliding, a series of periodic parallel ridges at the right angle to the sliding direction are always formed on the rubber surface shown in Figure 3-7. This is known as 'abrasion pattern' or sometimes as a 'Schallamach pattern'. However, when the sliding direction is periodically changed the formation of this characteristic abrasion pattern is prevented, the type of abrasion which occurs in this case is called intrinsic abrasion (Schallamach, 1958). The abrasion pattern dramatically increases the rate of abrasion loss and plays an important role in rubber abrasion. Therefore, many studies have been conducted investigating the formation of abrasion patterns.

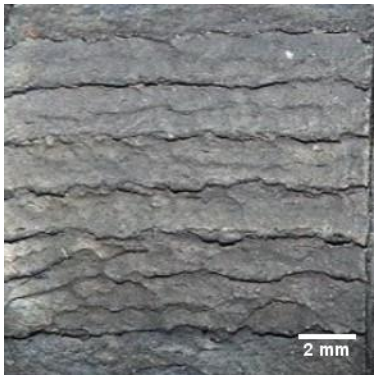

Figure 3-7. Abrasion pattern on rubber surface.

For fatigue wear the abrasion process can be divided in two separate phases, an initiation phase and a steady state, respectively. At first the abrasion rate increases and the pattern slowly develops. The geometry of the pattern, including ridge spacing and ridge height, grows continuously. When the pattern reaches a critical size, the abrasion weight loss maintains a constant value. Under these conditions the materials are exhibiting steady state abrasion. A bimodal size distribution of abraded particles has been reported, 1-5 µm during the initiation phase and up to several hundred µm during steady state abrasion (Gent and Pulford, 1983). Schallamach (1954) found that the spacing of the abrasion pattern was proportional to the cube root of the normal load, proportional to the two-thirds power of the particles size on an abrasive medium with polyhedral particles, and directly proportional to the particle size on an abrasive medium with hemispherical particles.

Blade abrasion was developed as a simple method to allow the application of fracture mechanics to rubber abrasion in 1974 (Champ et al.). Since then many studies have been conducted using this type of abrasion machine. The advantages of blade abrasion being that two abrasion stages can be clearly differentiated from the experiment and the method can predict the rate of rubber abrasion using an independent fatigue test. A general model was proposed by Southern and Thomas (1978), in which the tearing energy and crack growth rate could be determined when an abrasion patterns has been fully developed at steady state. There was a good agreement between the abrasion rate results and that derived from an independent crack growth measurement, as shown in Figure 3-8 for a non-crystallizing rubber. This indicated that the underlying mechanism

during abrasion was one of fatigue crack growth. The crack growth rate for crystalized NR during abrasion was much larger than that during a fatigue test. A possible reason being that the rapid deformation of the rubber during abrasion gave insufficient time for strain induced crystallization to arise. Zhang (1984a, 1984b, 1985, 1997) further investigated blade abrasion. His theory was further developed to clarify the phenomena and processes of rubber abrasion under different conditions of blade abrasion. Instead of using the approximate theory to calculate the tearing energy during blade abrasion as was initially proposed by Southern and Thomas (1978), Liang (2009, 2010) applied FEA to calculate the tearing energy during abrasion. An improved correlation was found for both unfilled and filled SBR. The high abrasion resistance of low strength BR probably was a result of the much smaller asperities of abrasion pattern formed under steady state, which resulted in a lower tearing energy.

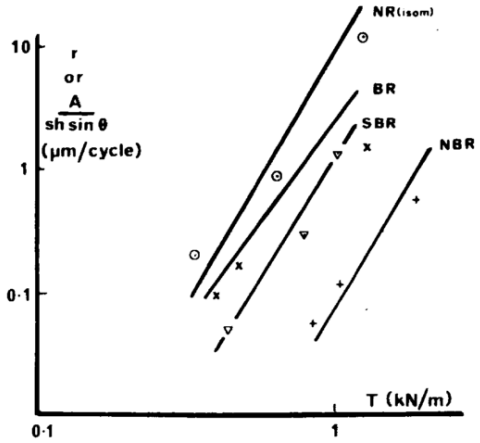

Figure 3-8. Correlation of abrasion results (points) and crack growth results (full lines) (Southern and Thomas, 1978).

The effect of the blade sharpness on the rate of abrasion was also studied (Muhr and Richards, 1992, Gent and Nah, 1996, Wu et al., 2013). Muhr and Richards (1992) claimed that the blade sharpness only speeded up the rate of development of a coarse pattern, but once formed, the abrasion rate depended more on the size of the pattern and the frictional force than on the blade sharpness. The role of the blade sharpness via a cutting mechanism as it dragged across a rubber surface was significant but secondary to the frictional mechanisms. However, Gent and Nah (1996) indicated that some rubber materials such as BR or NR were abraded at similar rates using either sharp or blunt

blades, and some other rubbers such as SBR were abraded much more slowly using a blunt blade. They also reported that the rates of abrasion decreased markedly with running time for some rubbers potentially as a result of the wear of the knife blade.

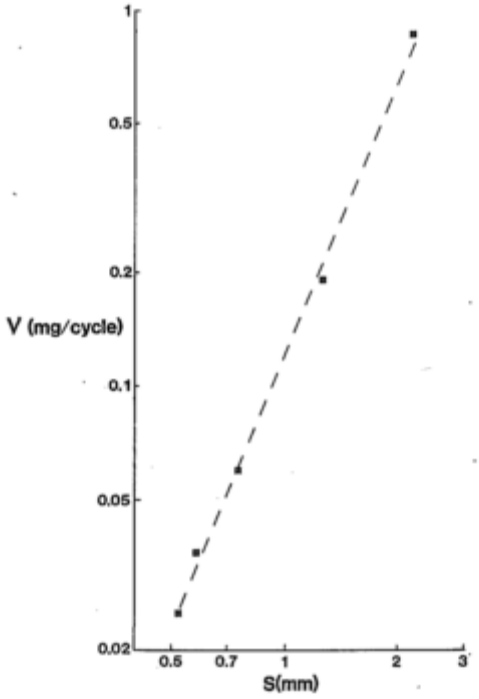

Figure 3-9. Relationship between abrasion rate and pattern spacing for SBR (Muhr and Richards, 1992)

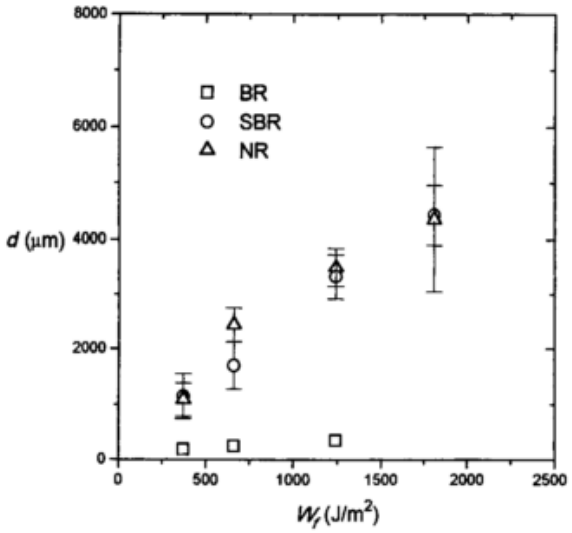

Figure 3-10. Relationship between pattern spacing and frictional work input (Nah and Han, 1998).

A power law relationship between the volume loss and pattern spacing was found as shown in Figure 3-9 for blade abrasion (Muhr and Richards, 1992). A similar power law relationship between abrasion rate and frictional work was reported (Stupak et al., 1990). Nah and Han (1998) reported a relationship between the pattern spacing and frictional work input as is shown in Figure 3-10. Clearly the pattern spacing for the BR was much lower than that for the SBR or NR compounds. This might be explained by the lower friction encountered for BR material as BR has a lower T_g value. This explanation was further supported by the observation that SBR compound generated much smaller abrasion patterns and lower friction when tested at elevated temperature(Nah and Han, 1998). A model for the growth and detachment of the tongue of abrasion pattern at steady state has been postulated (Uchiyama and Ishino, 1992). Initially, the crack propagated downwards at the bottom of the ridge at an angle and a tongue was formed which gradually increased in size. As the tongue increased in length, smaller cracks formed tend to cut into the tongue and which eventually resulted in the formation of a detached wear particle, as shown in Figure 3-11.

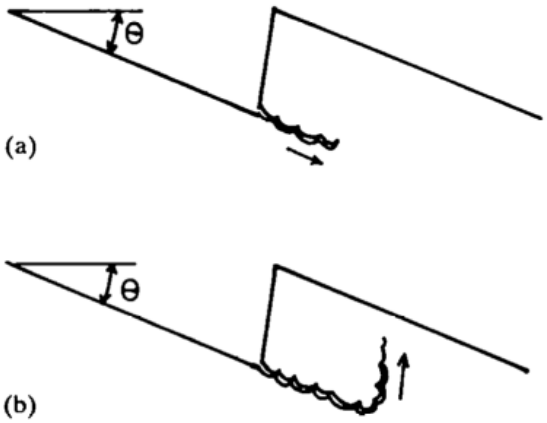

Figure 3-11. A model for crack propagation under the abrasion pattern asperity (Uchiyama and Ishino, 1992).

Hypothetical mechanisms for the crack initiation for the process of rubber abrasion were proposed by Gent (1989). Three potential mechanisms of crack initiation included unbounded elastic expansion of microscopic precursor voids, internal pressure by thermal decomposition of the rubber, and tri-axial tension by the dilating action of frictional forces.

Later, a micro-vibration and a stick-slip motion generated during frictional sliding of rubber was reported as two driving forces for the crack initiation by Fukahori and Yamazaki (1994a, 1994b, 1995). Figure 3-12 a) shows the typical spectrum of frictional force when a hard slider rubs against a rubber surface. A clear stick-slip motion at a low frequency of the order of 10-20 Hz was found, in which regions I and II corresponded to the stick and slip phase of stick-slip motion, respectively. Figure 3-12 b) is an acceleration spectrum of the normal vibration measured simultaneously with the frictional force. Violent micro-vibrations at a much higher frequency of the order of 500-1000 Hz were generated in the slip stage of stick-slip oscillation. The micro-vibrations had a natural frequency of the rubber and it was thought that these micro-vibrations were the driving force for the crack initiation process. However, the propagation of the cracks was strongly accelerated in the stick phase. The initial abrasion pattern spacing was determined as a distance defined by the ratio of the sliding velocity divided by the frequency of the micro-vibration. The final steady state pattern spacing correlated well with the distance defined by the sliding velocity divided by the frequency of the stick-slip motion. They also claimed that a filler raised the modulus and hence the natural frequency for both periodic motions, which in turn resulted in a smaller initial and final pattern spacing. However, the results obtained by Coveney and Christian (1999) did not support the theory of Fukahori that bursts of high frequency microvibration were the universal initiators for blade abrasion. Instead, high local stress concentrations were probably the initiation mechanisms (Muhr and Roberts, 1992). Fukahori and co-workers (2008) studied the crack initiation process using an FEA simulation. It was shown that the first crack generated at the location where the tensile stress was maximum during the slip phase of the stick-slip motion.

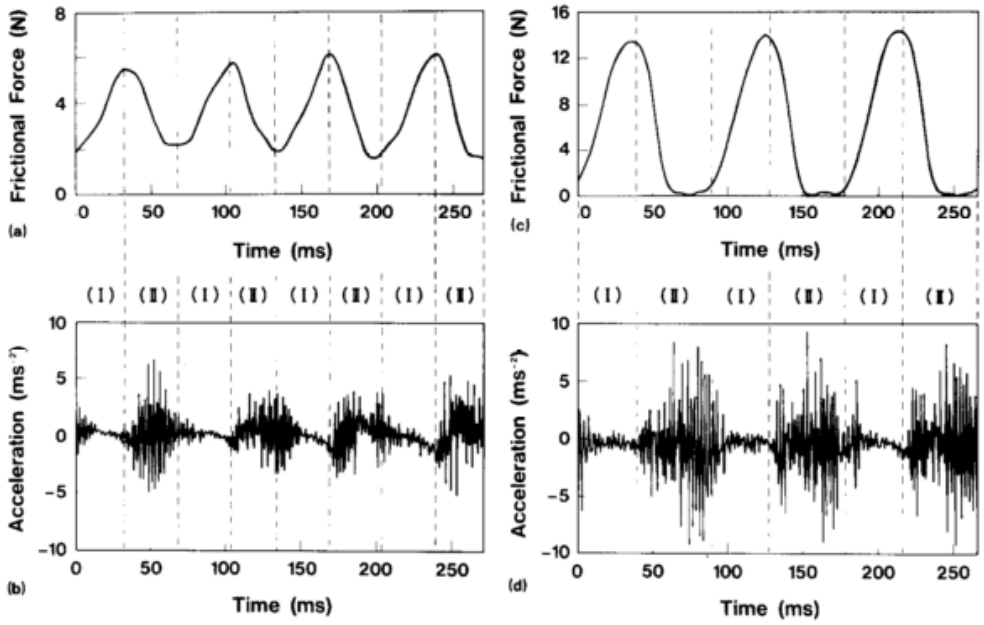

Figure 3-12. (a) Friction force spectrum against time at 4 N normal force. (b) Acceleration spectrum against time at 4 N normal force. (c) Friction force spectrum at 8 N normal force. (d) Acceleration spectrum at 8 N normal force (Fukahori and Yamazaki, 1994a).

The formation of the abrasion pattern was investigated in detailed by monitoring both the change in friction and the worn surface profile (Iwai et al., 2005). In Figure 3-13, stripe-like variations of friction appeared in the early stage of sliding which remained until steady state conditions were achieved. Most of the stripe like variations moved parallel to each other and were perpendicular to the direction of rubber sliding. The time period of these stripe-like friction variations hardly changed as the abrasion pattern developed. For the worn surface of rubber shown in Figure 3-14, a similar stripe-like profile appeared as well. The growth, movement and combination of the many small ridges that were present during the initiation state of abrasion was observed and this allowed the development of the abrasion pattern to be observed step by step.

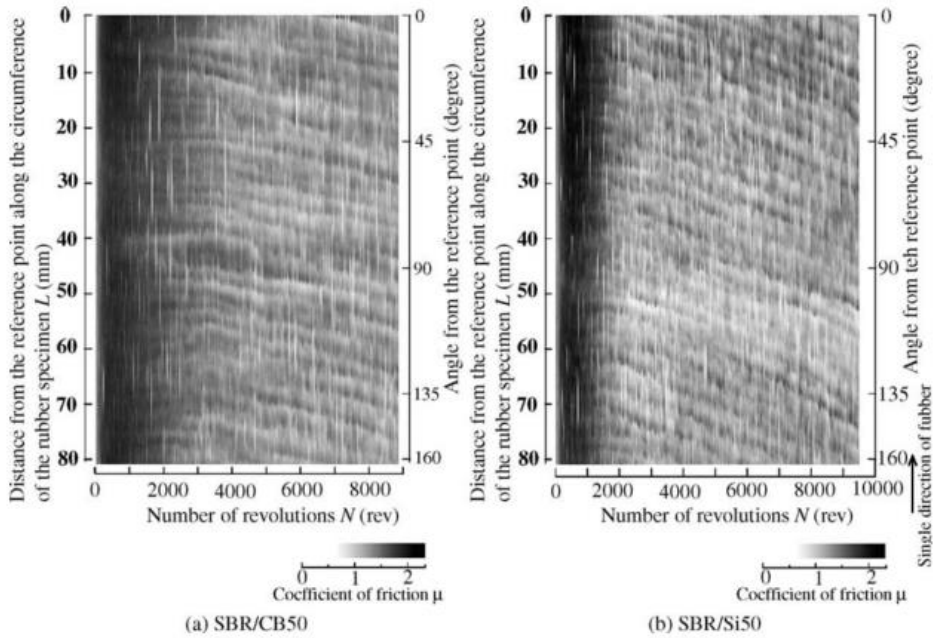

Figure 3-13. Distribution maps of the coefficient of friction along the identical extent of the circumference of the rubber surface. The density represents the value of the coefficient of friction: (a) SBR50CB and (b) SBR50SI (Iwai et al., 2005).

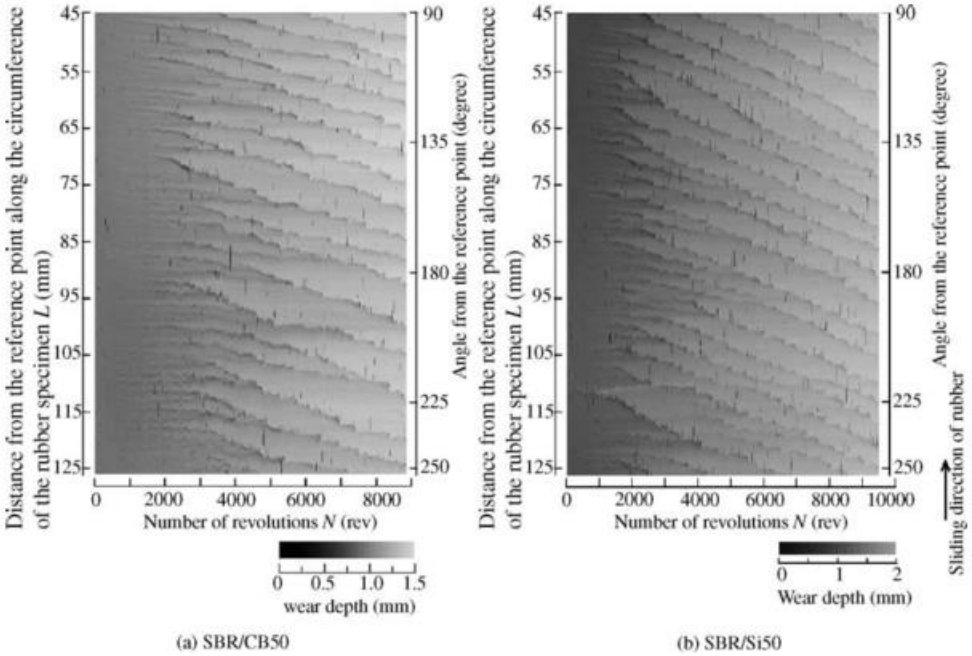

Figure 3-14. Distribution maps of the worn surface profile along the identical extent of the circumference of the rubber surface. The density represents the value of the height of the rubber surface: (a) SBR50CB and (b) SBR50SI (Iwai et al., 2005).

3.4 Smearing Wear

Both abrasive and fatigue wear result from a type of mechanical failure. However, under many test conditions, rubber abrasion is not a single mechanism process. When rubber compounds especially a tyre tread compound is abraded under mild conditions, a sticky, gooey transfer layer is often generated on the rubber surface as shown in Figure 3-15. This sticky transfer layer sometimes even appears on tyres on the road (Muhr and Roberts, 1992). The abrasion failure in this way is a type of degradation process which is referred as 'smearing' in the literature.

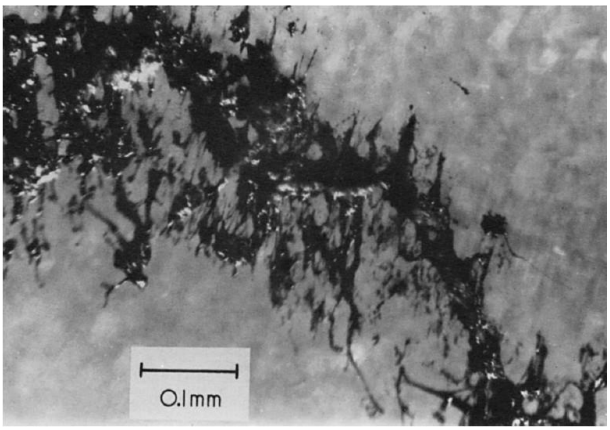

Figure 3-15. Sticky debris (Gent and Pulford, 1983).

This smearing effect has been widely reported (Howland et al., 1954, Rudakov and Kuvshinskii, 1964, Grosch and Schallamach, 1966, Gent and Pulford, 1983, Uchiyama, 1986, Thavamani et al., 1993, Morris, 2014). It is widely agreed that this smearing is due to some form of rubber decomposition, the detailed view as to which basic mechanism is responsible for the degradation process is still not agreed upon (Zhang, 1989).

Gent and Pulford (1983) described three potential degradation mechanisms: thermal decomposition due to local heating during sliding; oxidative deterioration possibly accelerated by local heating; and mechanical rupture of macromolecules to form reactive radical species. The most plausible mechanism of smearing seemed to be oxidative consummation of scissions produced by frictional force, in much the same way as occurred during cold mastication of NR (Arayapranee, 2012).

Although a few studies (Gehman et al., 1955, Uchiyama, 1986) indicated that the smearing result in an increase of the abrasion rate, most studies (Howland et al., 1954, Garten et al., 1956, Schallamach, 1968a, Muhr and Roberts, 1992) claimed that the smearing caused a significantly reduced abrasion rate. It is clear that this uncertainty has created an increases in the experimental difficulty of making reliable measurements during an abrasion test. Thus, a lot of effort has been made to avoid the formation of the sticky transfer layer. The most common ways encountered in standard tests include feeding a drying powder into the nip between rubber and counterpart, using a testing inert atmosphere, or by lowering the ambient test temperature. The effect of various drying powders such as magnesium oxide, Fuller's earth, and French chalk on abrasion was investigated (Grosch and Schallamach, 1966). As highlighted in Figure 3-16, two competing effects of powder could be confirmed. The first resulted in the abrasion rate being increased as the powder helped remove the lubricating low molecular weight impurities from rubber surface. In contrast, abrasion was decreased because the powder intervened and acted like a lubricant between the rubber and the track. The magnesia appeared to be the most effective way to prevent the smearing. It was demonstrated that certain rubbers like NR and SBR only degraded in the presence of oxygen. The rate was much less when they were abrasion tested in an inert atmosphere such as nitrogen. BR produced only dry debris during abrasion. It was proposed that any free radicals produced by main chain scission in a BR compound could rapidly react with the polymer itself, resulting in an increase in crosslinking density rather than degradation (Gent and Pulford, 1983).

Schallamach (1968a) investigated the abrasion of NR in an inert atmosphere. Figure 3-17 shows that following an abrasion in nitrogen, switching the atmosphere to air resulted in drop in the abrasion rate due to an instantaneous formation of a sticky transfer layer. The abrasion increased with time and was finally greater than the steady state rate of abrasion in nitrogen. When the abrasion rate of a rubber was low in air due to smearing, the subsequent abrasion in nitrogen was often greater than in air. However, the less grossly degraded rubber was mechanically weakened in air. If smearing was obviated by the use of a suitable dust, the abrasion was greater in air than in nitrogen as shown in

Figure 3-18. The temperature further complicates this description and is discussed in more detail in section 3.5 later.

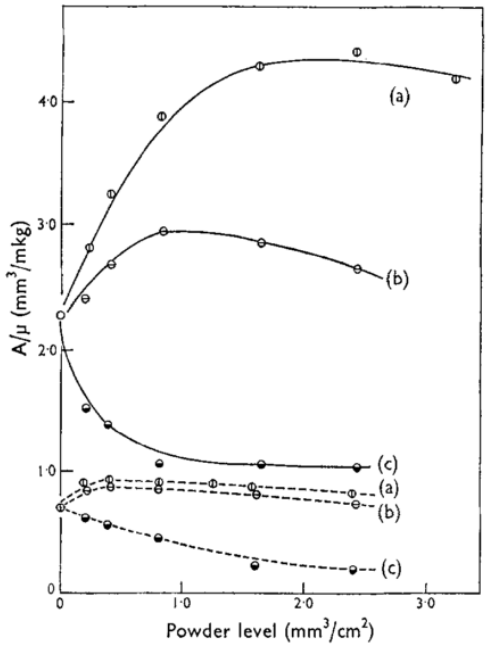

Figure 3-16. Abradability (solid lines) and coefficient of friction (dash lines) as a function of dust level at 95°C. (a) Magnesium oxide; (b) Fuller's earth; (c) French chalk (Grosch and Schallamach, 1966).

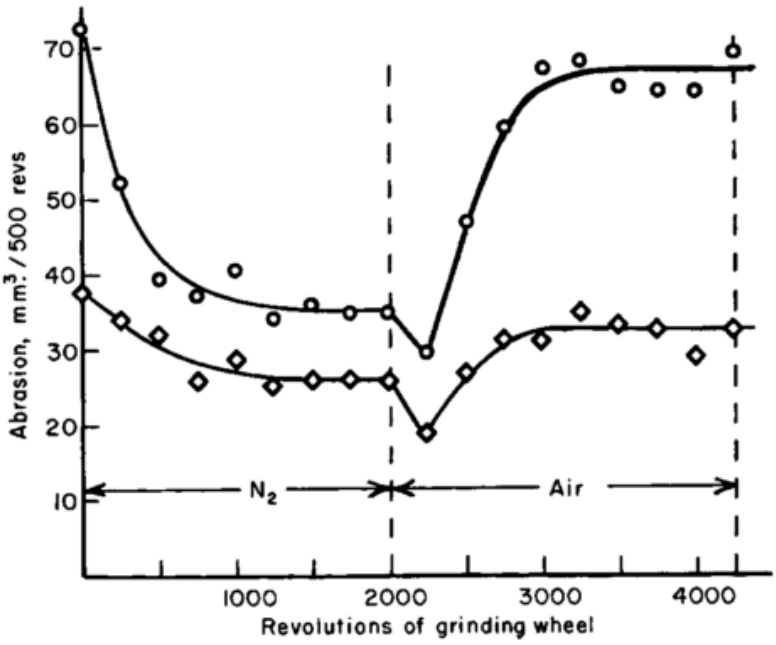

Figure 3-17. Effect of the atmosphere on abrasion rate for NR. (○) No antioxidant; (◊) 2 phr Nonox ZA (Schallamach, 1968a).

Gehman et al. (1955) measured the smearing temperature, although there was not a sharp melting point for rubber. It was reported that no smearing was found for SBR. In contrast, NR compounds smeared heavily. Therefore, they claimed that was why SBR showed better abrasion resistance at higher temperature. Garten (1956) proposed that carbon black could react with chain scission products. The free radicals caused by abrasion might not react with oxygen but might preferentially recombine with the active sites on the carbon black surface. These primarily formed bonds between carbon and rubber could well be broken up again under a suitable shearing force, which might even allow some of original chain fragments to recombine. If this were true then, the rubber matrix in the elastomer composite was protected against further degradation. The effect of antioxidant on smearing was also investigated. As shown in Figure 3-17, antioxidants significantly reduced the abrasion rate in air. It was reported that antioxidants were only effective in reducing the abrasion rate of NR during smearing abrasion. They had no noticeable effect when physical, cohesive fracture processes dominated the behaviour (Pulford, 1983). In terms of friction, the smeared film adhered strongly to the mating surface and increased the friction coefficient (Uchiyama, 1986).

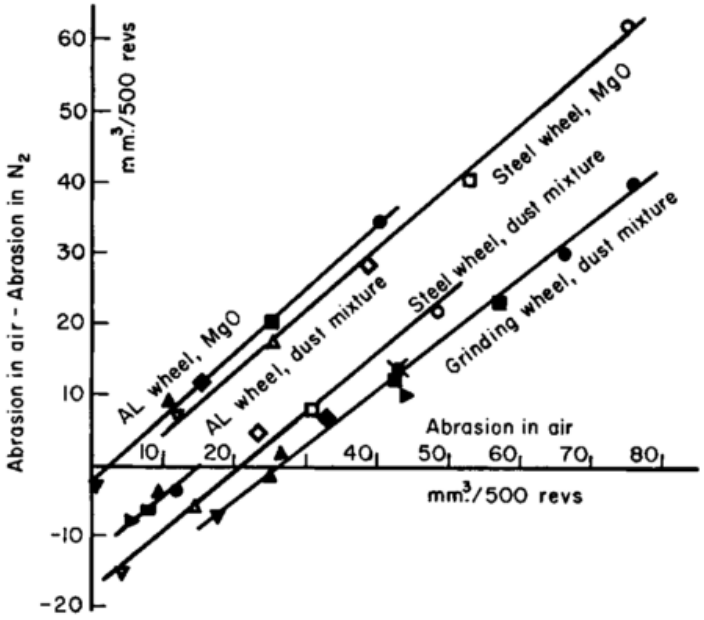

Figure 3-18. Difference between the abrasion in air and in nitrogen as a function of the abrasion in air (Schallamach, 1968a).

3.5 Effect of Temperature

Temperature plays a very important role during rubber abrasion. Not only does it affect the viscoelastic properties of rubber itself, but it can also determine the actual abrasion mechanism. There are three contributions of temperature during rubber abrasion, the ambient temperature, the contact temperature, and the flash temperature (under the hot spot at the contact point). Most studies have investigated the effect of ambient temperature on abrasion rate as this is the easiest one to control. The flash temperature generated due to the local friction in the contact area is in contrast much more difficult to measure. Frictional energy and sliding velocity during abrasion leads to a temperature build-up in the contact area. Figure 3-19 shows the temperature rise in the contact area as function of speed (Grosch, 1974). For a thick rubber strip such as a tyre, Grosch (2008) even derived a simple relation between the temperature and the sliding velocity, where the temperature rise was proportional to the square root of the velocity. An attempt was also made to determine the frictional temperatures which may occur in tyres under various driving conditions based on phenomenological theories of heat conduction (Viehmann, 1958). From this approach, it was predicted that under extreme conditions, such as under rapid acceleration, or during severe braking, high frictional temperatures would be encountered, which lie far above the decomposition temperature of rubber.

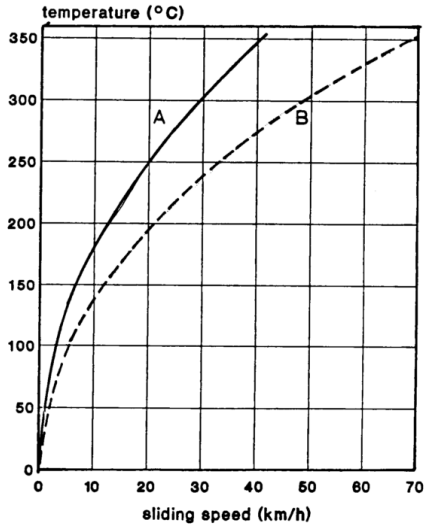

Figure 3-19. Temperature rise in the contact area of a small steel indenter as a function of speed A: cone tip radius 1 mm; B: sphere 11 mm diameter (Grosch, 1974).

For the abrasive wear shown in Figure 3-1, the abrasion rate decreased with a decrease in the temperature above T_g. This resulted from an increase in the relevant strength of the rubber as the temperature was reduced. Below -40°C the abradability increased sharply with a further reduction of the temperature, which is probably because at this rate of deformation the effective temperature of the rubber was reduced below its glass transition temperature. Therefore, it behaves like an abraded metal or plastic (Grosch and Schallamach, 1966). Gent (1983) carried out the blade abrasion test at room temperature and at 100°C. The results showed a relatively small effect of temperature on the rate of fatigue wear, which was inconsistent with a mechanical fatigue abrasion mechanism, since the crack growth rate was dramatically increased by a temperature rise of this amount. Later he (1996) showed that the rate of abrasion of SBR and BR at 100°C increased with time under a constant frictional work. This was attributed to aging of the rubber and a consequent reduction in tear strength. A periodicity in rate of abrasion was noted as the abrasion continued, the rate increased and subsequently decreased by a large factor as shown in Figure 3-20 due to aging of newly exposed underlying materials. Normally for smearing abrasion, higher temperature promotes the degradation process, which in turn increases the rate of smearing abrasion.

Different abrasion mechanisms dominate under different temperature range, at lower temperatures it is abrasive wear, moderate temperatures produce fatigue wear, and higher temperatures produce smearing. As a result of this, changing the temperature can switch the abrasion mechanism from one mechanism to another. Muhr and Roberts (1992) used an Akron type abrader running on a smooth glass slide. The results showed that both smeared and rubber particles were deposited one the glass. In the temperature range from -30 to 60 °C, the higher ambient temperature resulted in a greater production of smearing, and at lower temperature there was a greater amount of particular debris. In the case of temperatures below -20 °C no smearing was present. It was found that the abraded surface of all the compounds at 25 °C did not show any ridges except ploughing marks along the direction of abrasion. Ridges appeared above 50 °C (Thavamani and Bhowmick, 1993). It has been reported that the appearance of

the abraded rubber surface shows score mark at low temperatures and abrasion patterns at higher temperatures (Grosch, 2008).

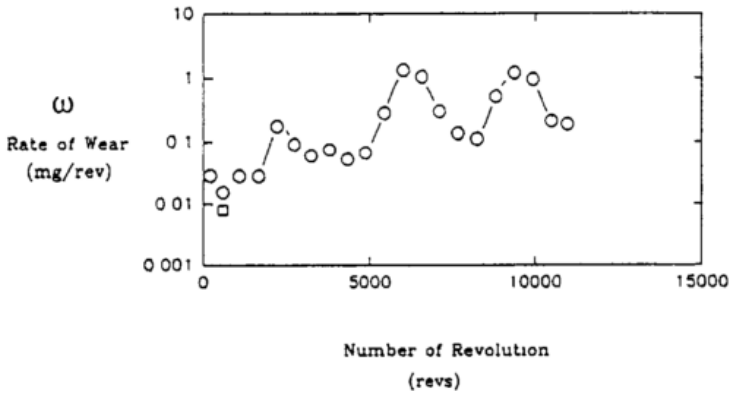

Figure 3-20. Abrasion rate as a function of revolution for unfilled SBR at 100°C (Gent and Nah, 1996).

3.6 Effect of Lubricants

Lubricants are widely used to protect the rubber from severe abrasion. Lubricants can keep the rubber surface and the counterpart seperate. Therefore, the friction is significantly reduced on a smooth surface. The effect is not as significant when the rubber has a rough surface.

Muhr (1987) investigated the effect of lubrication on blade abrasion. It was shown that lubrication dramatically reduced the rate of abrasion and the size of the abrasion pattern. Nevertheless, they only have a small influence on the overall frictional force. For blade abrasion under wet conditions, a modification of the deformation of abrasion pattern makes the frictional force less efficient at propagating cracks into the rubber. Mofidi (2008, 2010) reported that in many conditions, the lubrication caused the abrasive wear of rubber to be increased. Two different reasons may account for this effect. One is that the rubber was weakened or swollen in the presence of lubricating oil. The other might be because lubrication prevented the wear debris aggregating, which provided more direct contact. It was also found that the lubricants can also change the abrasion mechanism. In the presence of water, abrasive wear dominated the rate of wear loss, whereas under dry friction condition, the prominent wear mechanism were

combination of abrasive wear and fatigue wear as reported by Wu and his colleagues in their study (2016).

3.7 Predicting Tread Wear On Road

3.7.1 Laboratory Based Abrasion Testing

The easiest way to predict the actual tread wear is to replicate the full service conditions in an accelerated laboratory abrasion test. However, factors such as tyre construction, vehicle characteristics, road conditions, driving habits, locality, weather conditions and other variables discussed by Veirh (1992) each influence real tyre tread wear. As a result of this complexity, there is little scope up to now of reproducing service testing in the laboratory. On the other hand, there is a real need for a laboratory method that can be used for evaluate the abrasion resistance of rubber compounds (Adams et al., 1952). Many different laboratory abraders have been developed including: the Lambourn abrader (Adams et al., 1952, Howland et al., 1954, Ramakrishnan et al., 1995); the Akron abrader(Schallamach, 1960, Mathew and De, 1983, Wei et al., 2012); the LAT 100(Grosch, 2004, Heinz and Grosch, 2007, Grosch, 2008, Dorozhkin et al., 2015); and the DIN abrader (Mathew and De, 1983, Kim et al., 1999, Pal et al., 2009). The attributes of each of these abrasion test machines are described.

The Lambourn abrader is essentially a machine for driving a small rubber wheel on an abrasive wheel to which a continuous braking force is applied (Adams et al., 1952). The schematic of the Lambourn type abrader is shown in Figure 3-21. The constant slip between the rubber wheel and the grinding wheel is determined by a gear box. A suitable surface drying powder is applied through a soft transfer wheel.

The Akron abrader described in British Standard BS903 Part A9 Method B (Institution, 1988) is very similar as the Lambourn abrader. Instead of positioning moulded rubber wheels in the same plane of the grinding wheel, the rubber wheels is placed at a certain angle to the grinding wheel in order to achieve the constant slip. The Akron abrader has the advantage of allowing a variation in the degree of slip during testing by virtual of changing the angle of the test sample (Arayapranee, 2012).

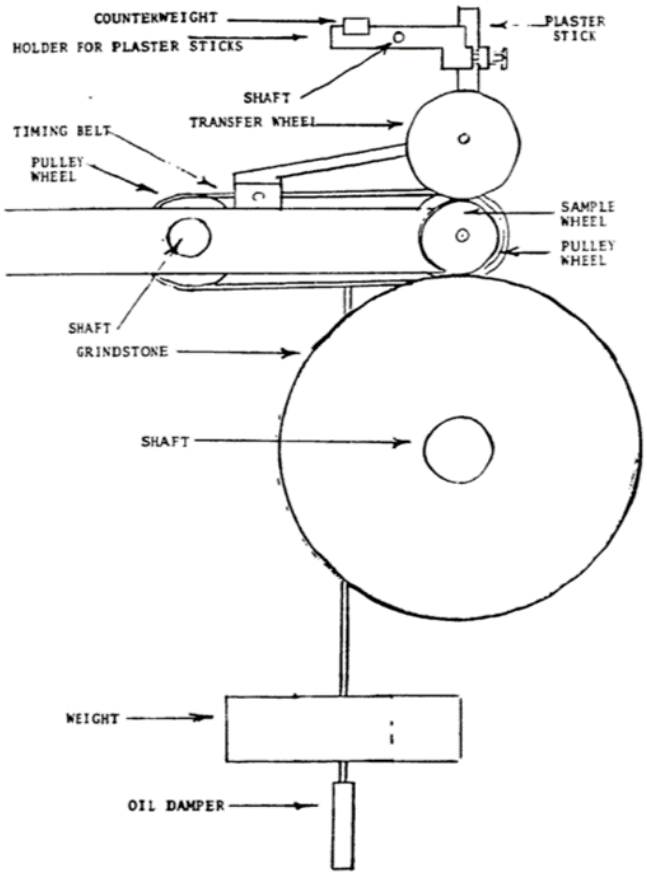

Figure 3-21. Schematic of the Lambourn abrader (Morris, 2014).

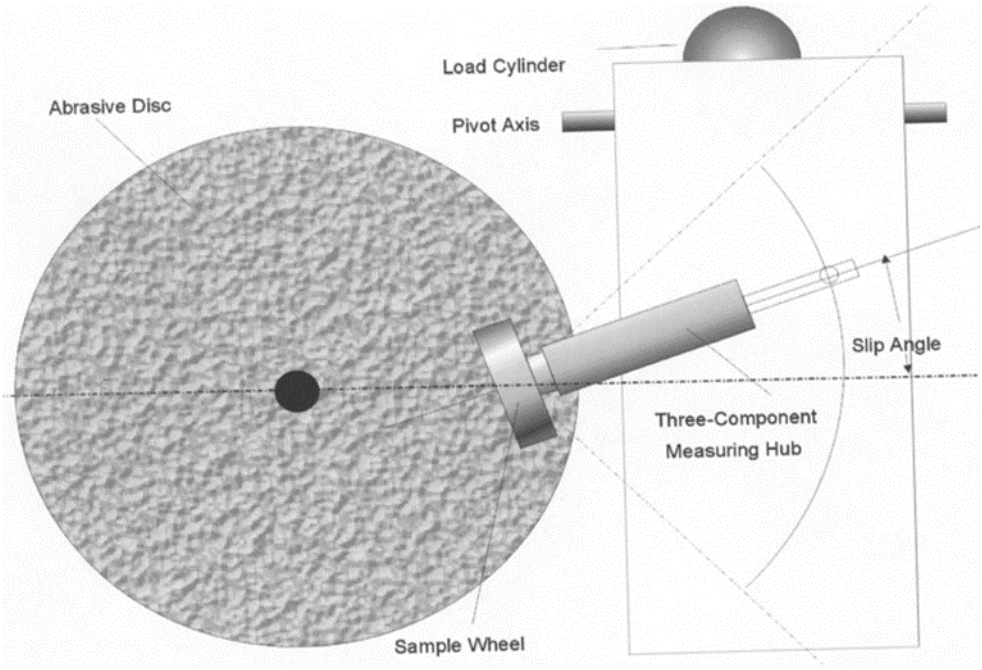

Figure 3-22. Schematic of LAT 100 abrader (Grosch, 2004).

The LAT 100 abrader also adopts this slip angle approach to maintain a constant slip of a test rubber wheel spinning on a flat abrasive disk as shown in Figure 3-22. The rubber sample wheel runs at a specified normal load at a specific speed (Grosch, 2004).

The DIN abrader (ISO4969, 2010) is another common encountered lab based abrasion machine. The rubber piece is sliding on a rotating cylinder covered with a sheet of the abrasive paper. The advantage of the DIN abrader is that it allows the test sample move across the whole surface of the drum as it rotates. Therefore, a greater abrasive surface area is provided during the test.

3.7.2 Analytical Model Approach

The other way to predict the real tyre wear is to use a tyre wear model. Although there are a large number of various factors affecting the tyre wear and it is difficult to take each fully into account, many studies (Saibel and Tsai, 1969, Mitchell, 1984, Luginsland, 2002b) have been done in the past to develop an analytical expression to predict real tyre wear.

Saibel and Tsai (1969) reviewed three different formulas for the tyre wear as listed below. Each of them was derived based on different criteria. They further claimed that it was difficult to set up a unified equation to describe the tyre wear phenomenon due to the differences between different kinds of rubber.

$$W_r = \theta^2 R_w f_w A\left[1+\alpha_T (T_s - T_A) + const.S_P\right] \qquad \text{Equation 3-1}$$

$$W_r = const.\frac{\left(E/\sigma_0\right)\mu^{\delta-\beta\delta-1}\left(\theta_s / a_L\right)^{2+\beta\delta}}{2+R_B\beta} \qquad \text{Equation 3-2}$$

$$W_r = const.\left(P\theta_s^{\,2} + Q\theta_s^{\,2}\right) \qquad \text{Equation 3-3}$$

Where, W_r is wear rate; θ_s is slip angle; R_w is resilience of the wheel; f_w is wheel stiffness; A is abradability; α_T is a temperature coefficient; T_s is the tyre surface temperature; T_A is the reference temperature at which $A = A_0$; S_P is the spacing of the

abrasion pattern; σ_0 is tensile strength; β is the fatigue exponent; R_B is a parameter specifying track roughness; a_L is length of contact area; P and Q are both material constants.

Using distribution functions for accelerations, speeds and loads, Grosch (2008) managed to calculate the necessary slip for a large number of driving events with the help of the brush tyre model. This road wear test simulation summed up all the volume losses associated with different events obtained using their laboratory abrasion equipment. Therefore, the tyre life time was estimated. Reasonable correlations were obtained for both passenger car tyres and truck tyres for certain rubber compounds.

Abraham (2015) further developed the theory proposed by Resnikowskij's tyre wear model and proposed a simplified fatigue wear resistance equation using the dynamic shear modulus G^* and only one fitting parameter, fatigue wear coefficient k_α shown as:

$$\zeta = \mu\sigma_0^{b_f} G^{\frac{2(1-b_f)}{3}} k_\alpha^{b_f} \qquad \text{Equation 3-4}$$

where, b_f is fatigue wear steadiness, derived from abrasion testing. The new analytical equation has been claimed to offer good correlations with real world tyre road wear.

3.7.3 Difficulties of Predicting the Tyre Wear

Although various laboratory abraders and tyre wear models are available today, there is still no universal laboratory test or simulation which can predict the tyre wear behaviour for all conditions. Each approach has its limitation. Morris (2014) showed the large discrepancy of the wear rate measured in the laboratory using a Lambourn type abrasion test and real road wear test data as shown in Figure 3-23 and summarised three possible reasons for the difference. Firstly, the short duration for the laboratory testing might not represent the much longer term performance of tyre wear as only the initial wear rate was measured. In addition, the laboratory testing was too severe. Therefore, a different abrasion mechanism to that observed in the field was being tested. The last

point being that the drying powder required during the laboratory testing might have a significant influence on the results.

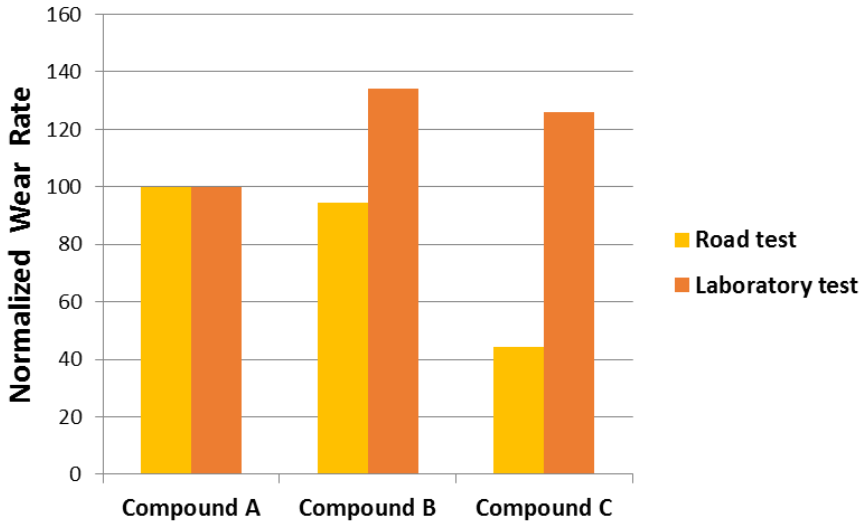

Figure 3-23. Comparison of the wear rate between laboratory test and road test (Morris, 2014).

3.8 Summary and Aim of the Study

Al lot of effort has been devoted to the investigation of rubber abrasion over the last sixty years and several of the abrasion mechanisms are now well described. However, rubber abrasion is still a very challenging topic in rubber research. Several theories have been proposed as reviewed above. However, there is no universal theory which can account for all real abrasion behaviour. For real applications such as tyre wear, no single mechanism dominates the behaviour. Since rubber abrasion is material (formulation) dependent, severity dependent, contact condition dependent and environment dependent. Several different mechanisms could contribute together to determine the final abrasion loss. Therefore, it is very difficult to predict the real tyre wear loss based on a laboratory test where the conditions are not identical to the in service conditions. It is even more difficult to try and use a computational simulation to predict the behaviour.

This study is attempting to investigate the fundamental mechanisms of rubber abrasion with the aspiration of understanding why laboratory tests used for compound

development very rarely correctly rank the abrasion performance of when tested in service. Since all the laboratory abraders used in the rubber industry as described in section 3.7.1 are too complex for the fundamental study. Only two simple abrasion tests, blade abrasion and surface contact abrasion, were performed, which allowed the investigation of rubber abrasion on both blunt and sharp and dry and wet contact conditions.

Several mechanisms exist for rubber abrasion. However, no systematic study has been done to look into the transition between these mechanisms. Even for a single mechanism such as the fatigue wear, although there is general agreement that the underlying behaviour is fatigue crack growth, how to derive the precise tearing energy encountered during abrasion is still a significant challenge. For smearing wear, it is not yet clear whether the sticky layer presented on rubber surface serves to protect the rubber or causes it to endure further loss? What exactly is this sticky layer? Can the molecular weight of the sticky debris be measured directly using some techniques such as Gel Permeation Chromatography (GPC)? How does this sticky layer affect the abrasion and friction properties during a test? All these questions are to be addressed to allow a better understanding of rubber abrasion in practice.

4 Chapter Four: Correlation of Fatigue Wear with Independent Crack Growth Measurement

4.1 Introduction

The development of blade abrader in 1974 (Champ et al.) was a significant breakthrough for the investigation of rubber abrasion. Once the abrasion pattern is fully formed on the rubber surface, a simple model can be applied to investigate the rubber abrasion using fracture mechanics. Therefore, the abrasion can be predicted by an independent fatigue crack growth tests. Previous work (Southern and Thomas, 1978, Liang, 2007) suggested that there was reasonable correlation for unfilled SBR materials. In this chapter two unfilled model material (SBR0 and NR0) and five typical tread compounds were tested using blade abrasion. Pure shear fatigue crack growth tests were then carried out to how well they correlated to the measured abrasion test results.

The rate of loading during abrasion is extremely fast with the frequency of loading on individual asperities on the rubber surface being in the kHz range. Conversely the rate of loading measured during the fatigue crack growth testing is much lower at rates closer to 1-10 Hz. In order to get a better correlation, it is necessary to bridge this frequency gap. However, in practice due to the limitations of the mechanical test equipment, it is very difficult to conduct the fatigue crack growth test at 1000 Hz. Three different loading configuration were used for the pure shear fatigue crack growth test to investigate the effect of loading profile on the crack growth rate. Normal sinusoidal waves at two different test frequencies of 2 Hz and 5 Hz were applied. And a pulse like loading profile which is closer in terms of the loading rate to the abrasion test was also conducted.

4.2 Experiment

4.2.1 Materials

Two unfilled rubber compounds (SBR0 and NR0) were compounded manually using an open two-roll mill. All the compounding ingredients were weighted precisely before the compounding process. In addition, five uncured typical tread compounds were supplied

by Cabot Corporation, MA, USA. Two of them were oil-extended SBR filled with 80 phr N234 carbon black and highly dispersible silica Zeosil 1165mp. The other two compounds were normal SBR filled with 50 phr N234 and silica. The last one was an oil-extended SBR and BR blend filled with 80 phr N234. The surface areas of N234 and HDS filler materials was measured by BET nitrogen absorption methods as being 125 and 160 m^2/g respectively (Donnet, 1993, Tunnicliffe, 2015). The uncured tread compounds were compounded in a Banbury-type internal mixer with a mixing chamber volume of 1 L. The optimal curing conditions were determined using an Alpha 2000 moving die rheometer. The detailed formulations and curing conditions for all the materials used are given in Table 4-1.

Table 4-1. Detailed formulations and curing conditions for 12.5 mm thickness rubber wheel in phr (Parts per Hundred Rubber).

Ingredient		SBR0	NR0	SBR80CB	SBR80SI	SBR50CB	SBR50SI	SBR/BR80CB
SBR	1500	100						
SBR	BUNA VSL 4526-2HM			137.5	137.5			82.5
SBR	BUNA VSL 4720-0HM					100	100	
NR	SMR CV60		100					
BR	BR CB24							40
Carbon black	N234			80		50		80
Carbon black	N330				6.4		4	
Silica	Z1165MP				80		50	
Coupling agent	Si69				6.4		4	
Process oil	Vivatec 500 Oil							15
Tackifier	Koresin			3	3	3	3	3
Wax				2.5	2.5	2.5	2.5	2.5
Zinc Oxide		3	5	3	3	3	3	3
Stearic Acid		1	2	2	2	2	2	2
Antioxidant	6PPD	1	3	1	1	1	1	1
Accelerator	CBS		1.5	1.1	2	1.1	2	1.1
Accelerator	DPG	1		0.3	2.1	0.3	2.1	0.3
Sulphur		3	1.5	1.4	1.6	1.4	1.6	1.4
Curing Temperature / °C		160	145	150	150	140	140	140
Curing time / minute		60	30	50	50	50	60	45

4.2.2 Tensile Test

An Instron 5967 machine with a 1 kN load cell was used to measure the stress-strain behaviour for all seven of the rubber samples. Flat dumbell-shaped specimens were tested at 50 mm/minute extension speed. The strain was recorded using a video extensometer. Five specimen were repeated for each sample. All the tests were performed at room temperature.

4.2.3 Blade Abrasion

The apparatus for blade abrasion testing is shown in Figure 4-1. It consisted of seven main components. The blade had an initial wedge shape when manufactured but as it was used extensively it also experienced significant wear. Therefore, the blade tip reached an equilibrium state which was used throughout these experiments with an approximately constant sharpness of 0.3 mm radius and as a consequence of wearing processes this surface was considered as being smooth during the analysis of the results. It was fixed at one end of a freely pivoted arm. The whole arm was mounted on a spring cantilever, whose horizontal displacement was measured by a non-contact displacement sensor. The output voltage was measured using a digital multimeter. The displacement sensor was calibrated to obtain the relationship between the horizontal force applied on the blade and from a voltage measured by the multimeter. As shown in Figure 4-2, a good linear relationship was obtained. The other side of the arm was attached to a simple dashpot damper. The purpose of the damper was to reduce the vibration which was caused from the sliding of the blade over the sample. The vibration could be quite large in an un-damped system when the abrasion pattern was coarse.

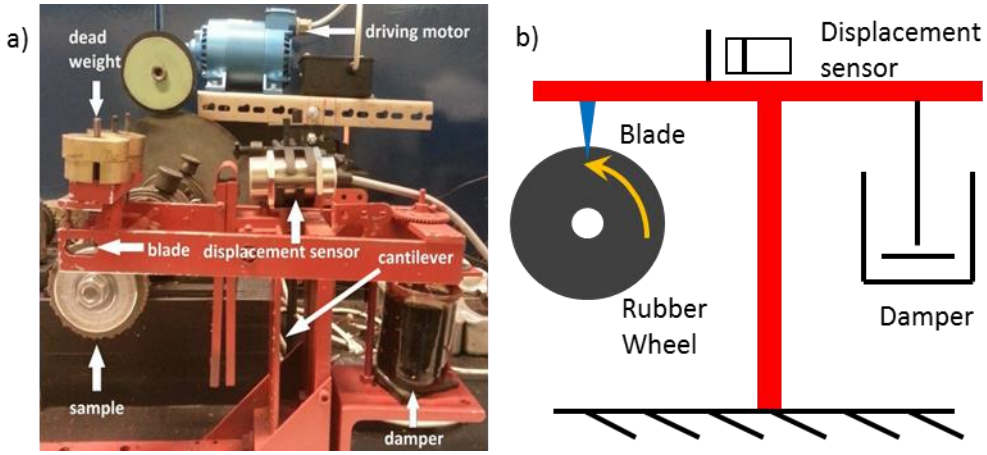

Figure 4-1. a) Blade abrasion apparatus and b) schematic diagram.

A rubber wheel was compression moulded with an internal diameter of 12.5 mm, an external diameter of 68 mm and having a thickness of 12.5 mm using a hot press with the optimal curing conditions determined by the rheometer at the appropriate temperature. The rubber wheel was fixed on a shaft, which was driven by an induction motor through a gearbox. The rubber wheel was rotated against a stationary razor blade edge at 21 rpm, which corresponded to an average sliding velocity of 70 mm/s. Dead weights exactly on the top of the blade were used to apply the normal force. Most of wear debris dropped off automatically during the test. The residual debris was removed by carefully brushing of the abraded surface using a natural bristle brush before each weight measurement was made. The weight of the sample was measured using an electronic analytical balance with 0.1 mg tolerance.

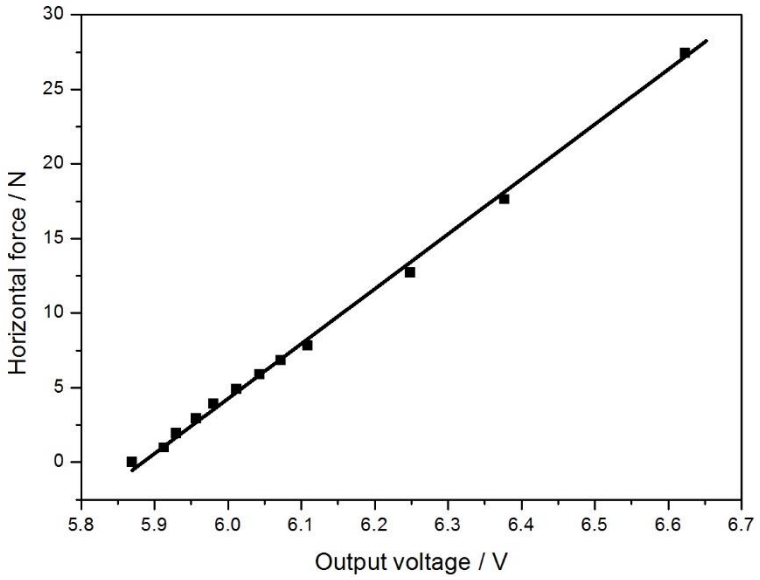

Figure 4-2. Relationship between applied horizontal force and output voltage of the displacement sensor.

4.2.4 Pure Shear Fatigue Crack Growth Test

Pure shear fatigue crack growth tests were carried out to characterise the cyclic crack growth under dynamic loading conditions. Pure shear deformation was achieved by stretching a rubber strip in the vertical direction, normal to the long dimension, whilst maintaining the length in the longer transverse dimension unchanged by virtue of the use of long test piece clamps. Therefore, the length of the specimen, w, has to be at least 8 times longer than the specimen height, h, to keep the constraints imposed by the grips in the uncracked region in approximately a pure shear deformation. The specimen used had a dimension of 175 $\times$ mm $\times$ 20 mm$\times$ (2-3) mm with a pre-cut crack introduced using the method described by Liang (2007) and Busfield (2002). A schematic of pure shear fatigue crack growth test specimen is shown in Figure 4-3.

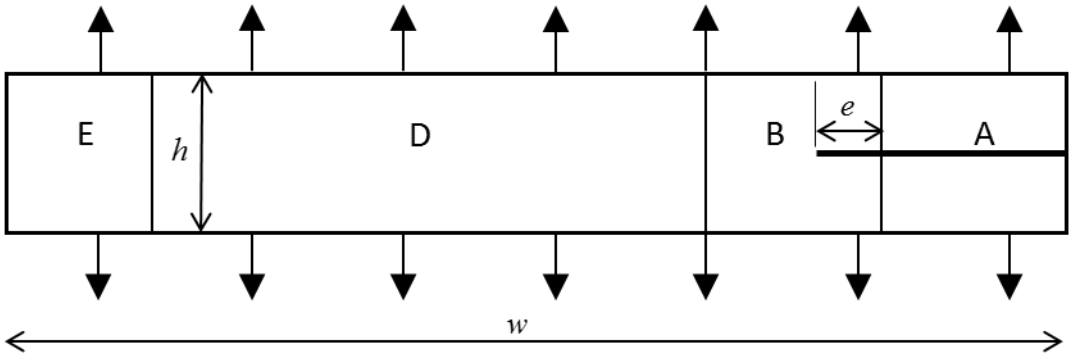

Figure 4-3. Schematic of the various deformation regions in a pure shear fatigue crack growth specimen.

Region A is the unstrained region. The length of the introduced pre-cut crack was more than 40 mm long to ensure this free region was of sufficient length prior to the start of the testing. Region B is the complex deformation region around the tip. It is considered to remain constant in size and simply translates along with the crack as the crack propagates. Region D is deformation in the test piece that is considered to act under pure shear conditions and region E is in a more complex strain due to the edge effect that remains constant at each specific strain throughout the test. As the crack propagates, the net effect is to transfer pure shear region D to unstrained region A. Therefore, the tearing energy is given (Rivlin and Thomas, 1953):

$$T = Wh \qquad \text{Equation 4-1}$$

where W is the stored energy density of the deformed pure shear test specimen far removed from the crack tip.

De (1994) found that a strip of width e of the specimen as shown in Figure 4-3 was not totally energy free. He measured experimentally that e was around 28% of the original height h and also independent of the crack length. Therefore, tearing energy can be expressed directly from the maximum measured energy in a loading cycle during the testing as:

$$T = \frac{U}{t_0\left(w - c + e\right)} \qquad \text{Equation 4-2}$$

where U is the total elastic stored energy in the test specimen at a specific cycle; t_0 is the initial unstrained specimen thickness; and c is the length of the crack. Equation 4-2 was used in this work to calculate the tearing energy for the pure shear fatigue crack growth test.

An Instron Electropuls E1000 machine equipped with 10 kN load cell was used to impose the cyclic deformation. Three loading profiles were carried out to investigate the effect of loading profile on the crack growth rate. Sinusoidal waveforms with two different frequencies of 2 Hz and 5 Hz were applied. Another load case applied a pulse-like loading configuration which was to closer to the loading conditions encountered during abrasion. This loading condition is known throughout as the pulse loading condition and its loading pattern is shown in Figure 4-4, as a triangle shape displacement applied for 0.2 s and the specimen was in a relaxed condition for 0.3 s. All of the tests were conducted under fully relaxed conditions at the temperature of the test laboratory, which was maintained at around 22 °C. The total stored energy was calculated by integrating the stress-strain curve during the loading cycle after the maximum stress attained in each loading cycle reached equilibrium. The pre-cut crack was induced by a razor blade with the initial length more than 40 mm. The length of the crack in the horizontal direction (crack depth) was recorded by a web camera throughout the test. An initial picture of the crack was taken with an appropriate length scale to calibrate the pixel resolution of the image. Images of the crack progression were then taken regularly throughout the test at specific numbers of recorded cycles under the fully extended conditions. All the pictures were processed using ImageJ software to calculate the crack length by measuring the number of pixels in the crack depth direction. A razor blade was used to re-direct the crack to the middle if it had deviated to the edge of the sample.

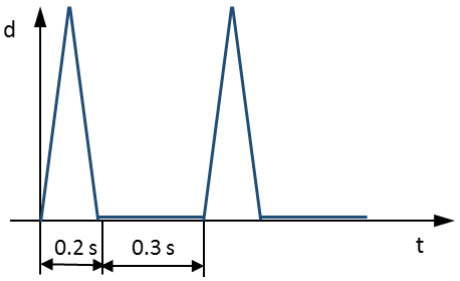

Figure 4-4. Pulse like loading profile (Pulse loading).

4.3 Results and Discussion

4.3.1 Stress-Strain Behaviour

Figure 4-5 shows the stress strain curve for both the unfilled and filled rubbers. SBR0 has a slightly higher modulus at a low strain (below 2) and a significantly lower tensile strength compared to NR0. NR0 exhibits a higher tensile strength due to the onset of strain induced crystallisation above 250% strain. Under the same filler loading conditions, the silica filled SBR compounds typically have a slightly higher modulus than the carbon black filled rubbers, since the silica used in this study has a larger surface area and smaller aggregate size than the carbon black used. SBR/BR80CB has the lowest modulus probably due to the lower T_g of BR.

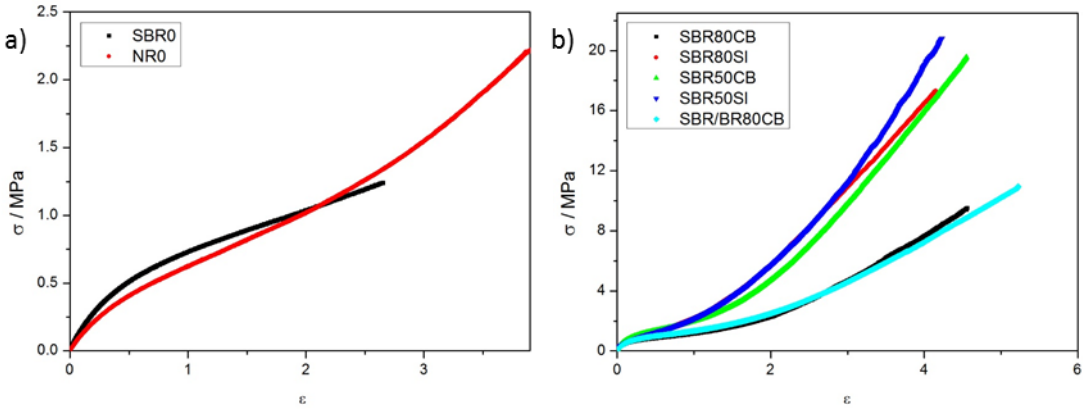

Figure 4-5. Stress strain curve for the a) unfilled rubbers and b) filled rubbers.

4.3.2 Initiation State for Blade Abrasion

Figure 4-6 shows the accumulative weight loss for NR0 under a 20 N normal force. The behaviour shown is typical for the abrasion weight loss for the unfilled rubber material

tests. The initial material loss rate at the start of the abrasion process was reduced, because it takes time for an abrasion pattern to develop on the smooth moulded surface. The rate increased and remained at a constant, once the abrasion reached steady state.

The abrasion pattern developed slowly the initiation state. When the abrasion reached steady state, the abrasion pattern with constant geometry was fully developed on the rubber surface. As an example, the development of the abrasion pattern for SBR0 under a 20 N normal force is shown in Figure 4-7. For the NR0, there was a sticky and gooey layer formed on the surface during the initiation phase, as shown in Figure 4-8. As the abrasion developed, this sticky layer was eventually overtaken by the formation of an abrasion pattern. The final abrasion patterns of SBR0 and NR0 under different normal loads are shown in Figure 4-9. The coarseness of the pattern increased as the normal load increased.

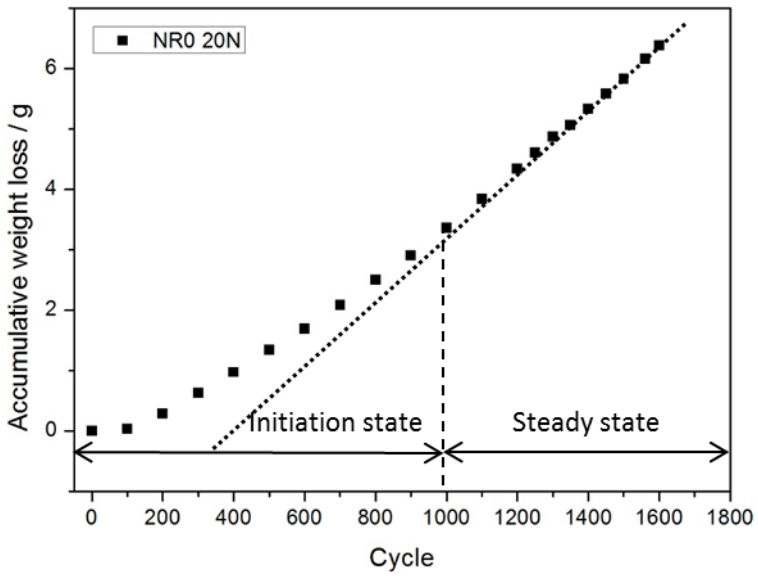

Figure 4-6. Blade abrasion weight loss for NR0 at 20 N normal force.

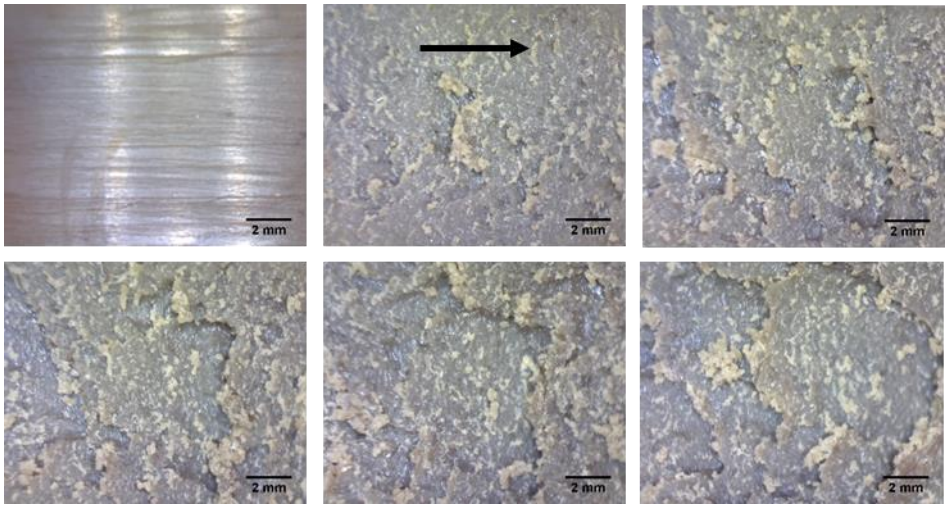

Figure 4-7. The abraded surface for SBR0 under 21 N normal load from left to right at 0, 90, 150 cycles for the first line and at 200, 250, 550 cycles for the second line; the arrow shows the sliding direction.

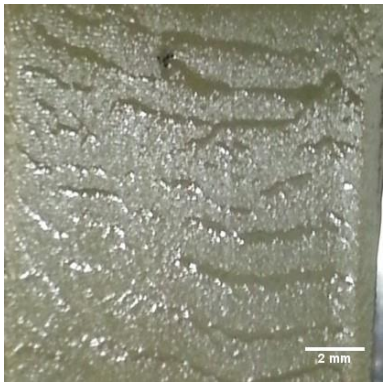

Figure 4-8. Sticky surface of abraded NR0 during the initiation state of blade abrasion.

The filled rubbers also formed a sticky layer on the rubber surface during the initiation state similar to the initiation phase with NR0. The abrasion pattern observable in Figure 4-11 developed eventually for most of the filled materials and overtook the formation of a sticky surface once steady state abrasion was reached. Figure 4-10 shows the morphology of the rubber surface for SBR80SI at different stages of abrasion along with the weight loss at 26 N normal force. The steady state patterns for each of the different rubbers at different normal force is shown in Figure 4-11. The only exception being SBR/BR80CB, where there was no abrasion pattern formed even though many cracks were formed on the abraded surface as shown in Figure 4-12.

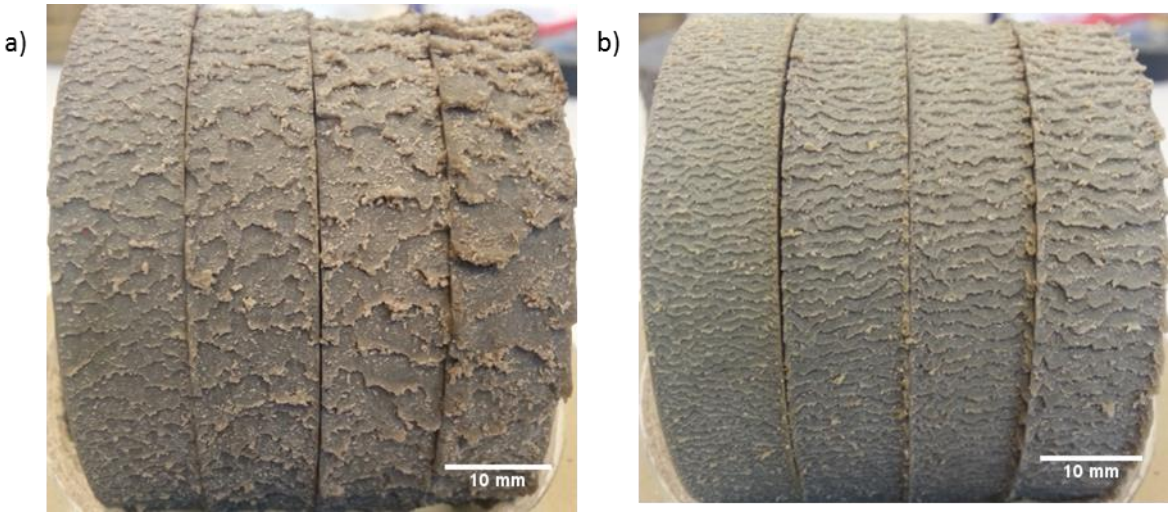

Figure 4-9. The fully developed abrasion pattern under 8 N, 12 N, 16 N and 20 N from left to right for a) SBR0 and b) NR0.

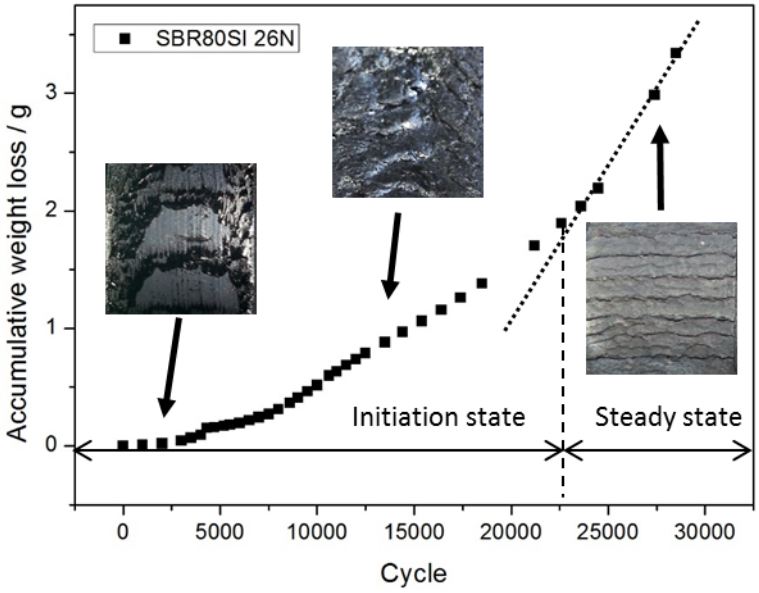

Figure 4-10. The weight loss and the morphology of abraded surface forSBR80SI.

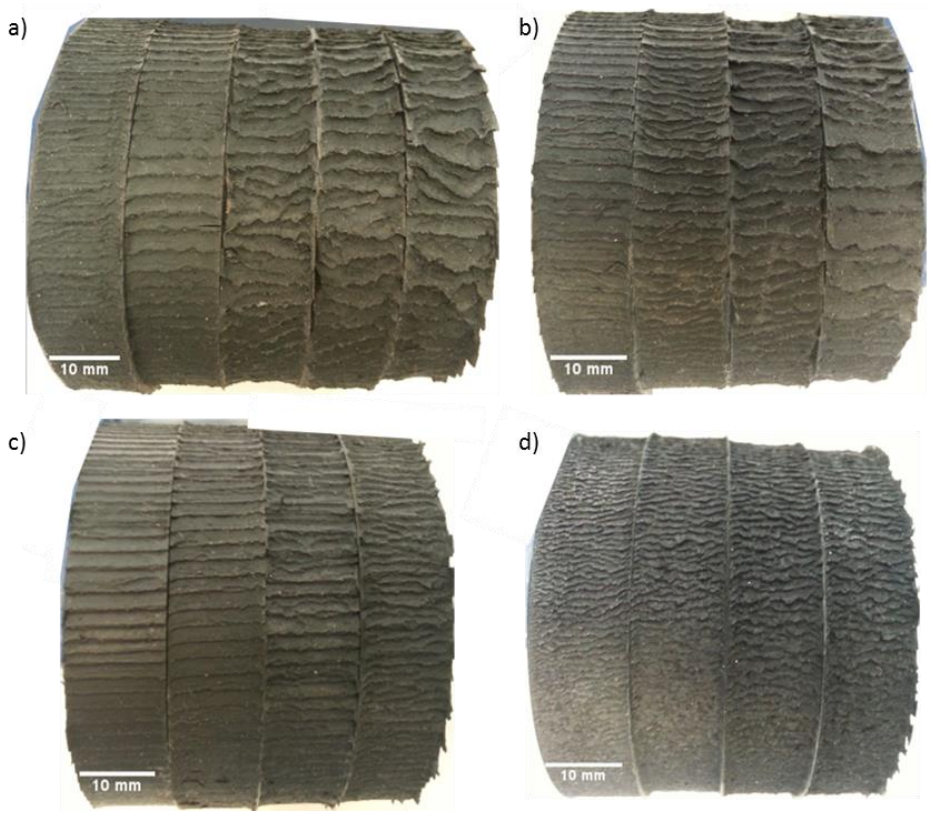

Figure 4-11. Fully developed pattern for four of the filled rubbers: a) SBR80CB at 12 N, 16 N, 20 N, 26 N, 31 N normal force from left to right; b) SBR80SI at 16 N, 20 N, 26 N, 31 N normal force from left to right; c) SBR50CB at 20 N, 26 N, 31 N, 36 N normal force from left to right; d) SBR50SI at 26 N, 31 N, 36 N, 41 N normal force from left to right.

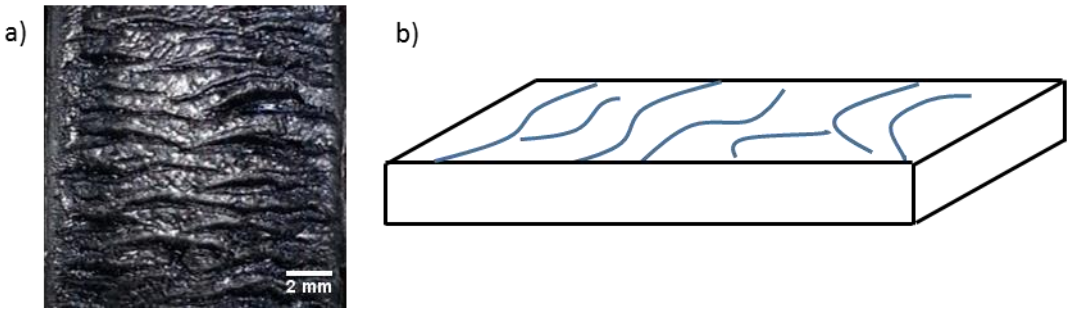

Figure 4-12. a) Abraded surface for SBR/BR80CB and b) schematic graph of the abraded surface (blue lines indicate cracks on the surface).

It is clear that there are two different mechanisms of material loss present during blade abrasion. The first being the formation of the sticky layer is most likely due to the mechano-chemical degradation (Gent and Pulford, 1983). This is often known as smearing wear as is discussed in the chapter 3. The other being a fatigue wear

mechanism as a result of cyclic crack growth, where an abrasion pattern is fully generated. The development of abrasion pattern gives rise to the greater rate of abrasion weight loss.

These two abrasion mechanisms are competitive with each other. Filled rubber compounds have a greater resistance for cracking. It takes longer for cracks to arise at the abraded rubber surface. This allows more time for the temperature to build-up and for chemical oxidation processes to commence. Accordingly, a sticky layer is formed on the rubber surface at the beginning of blade abrasion. As soon as the crack develops on the surface, a fatigue wear process starts to develop and under certain conditions as the abrasion speeds up this process gradually overtakes the much slower smearing wear. Eventually the sticky layer is replaced by an abrasion pattern. For unfilled rubbers, as they have lower strength and fatigue resistance, the cracks can more easily be formed on the rubber surface perhaps after only a few cycles. There is insufficient time for a sticky layer to be generated on the rubber surface and an abrasion pattern is quickly established. The reason that SBR/BR80CB never develops abrasion patter is probably due to the lower T_g, which is less likely to form abrasion pattern (Nah and Han, 1998).

4.3.3 Abrasion Crack Growth Angle and Abrasion Crack Growth Rate at Steady State

Once the steady state was reached, the crack growth angle and the crack growth rate were determined as follows. First before each test, the geometry of the sample wheel was measured carefully using a Vernier calliper with 0.02 mm accuracy. The internal and external diameter and the thickness of the wheel were measured at three distinct positions and these measurements were averaged to minimise the geometrical errors resulting from the eccentricity of the test wheel. The initial volume v_0 is given by:

$$v_0 = \frac{\pi}{4}\left(D_0^2 - d_0^2\right)h_0 \qquad \text{Equation 4-3}$$

where D_0 and d_0 are the external and internal diameter; h_0 is the thickness. The density was derived as:

$$\rho = \frac{m_0}{v_0}$$ Equation 4-4

where m_0 is the initial mass of the sample. The weight loss of the rubber wheels was converted to the radius reduction using the following equation:

$$\frac{\mathrm{d}r}{\mathrm{d}n} = -\frac{r_{i+n} - r_i}{n}$$ Equation 4-5

where n is the number of cycles and r_i is the sample radius at i th cycle expressed by:

$$r_i^2 = \frac{m_i}{\pi h_0 \rho} + \frac{d_0^2}{4}$$ Equation 4-6

Simultaneously the movement of a single ridge of the abrasion pattern was recorded using a digital microscope. Figure 4-13 shows the distance from an individual ridge to a reference line before and after being abraded for 2000 cycles. The advancement of the ridge per cycle $\frac{\mathrm{d}p}{\mathrm{d}n}$ is given as:

$$\frac{\mathrm{d}p}{\mathrm{d}n} = -\frac{p_{i+n} - p_i}{n}$$ Equation 4-7

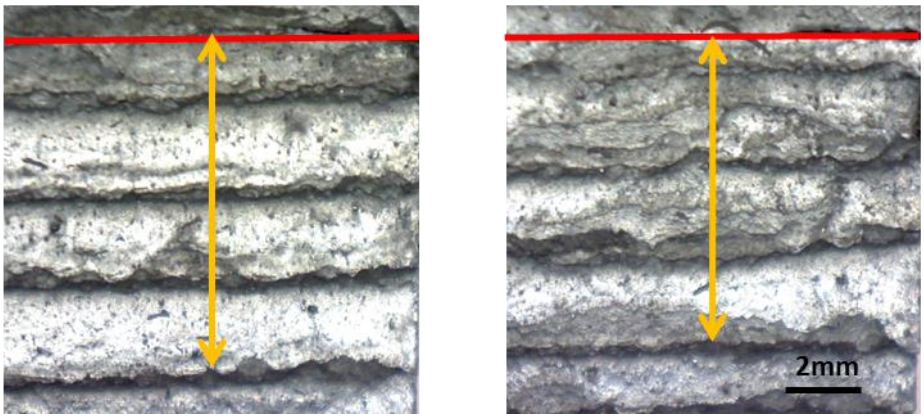

Figure 4-13. The ridge movement of SBR50CB after 2000 cycles. Red line is a reference line.

As shown in Figure 4-14 the relationship between $\frac{\mathrm{d}c}{\mathrm{d}n}$, $\frac{\mathrm{d}r}{\mathrm{d}n}$, and $\frac{\mathrm{d}p}{\mathrm{d}n}$ can be expressed by:

$$\left(\frac{\mathrm{d}p}{\mathrm{d}n}\right)^2 + \left(\frac{\mathrm{d}r}{\mathrm{d}n}\right)^2 = \left(\frac{\mathrm{d}c}{\mathrm{d}n}\right)^2$$ Equation 4-8

Therefore, the crack growth angle during the steady state is given as:

$$\tan\theta = \left(\frac{\mathrm{d}r/\mathrm{d}n}{\mathrm{d}l/\mathrm{d}n}\right) \qquad \text{Equation 4-9}$$

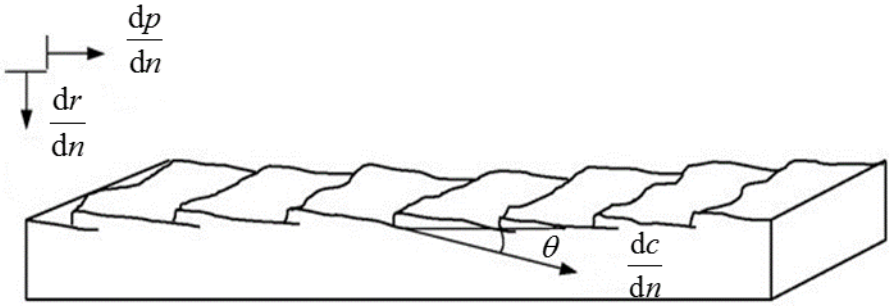

Figure 4-14. Sketch of an abrasion pattern (Muhr and Richards, 1992).

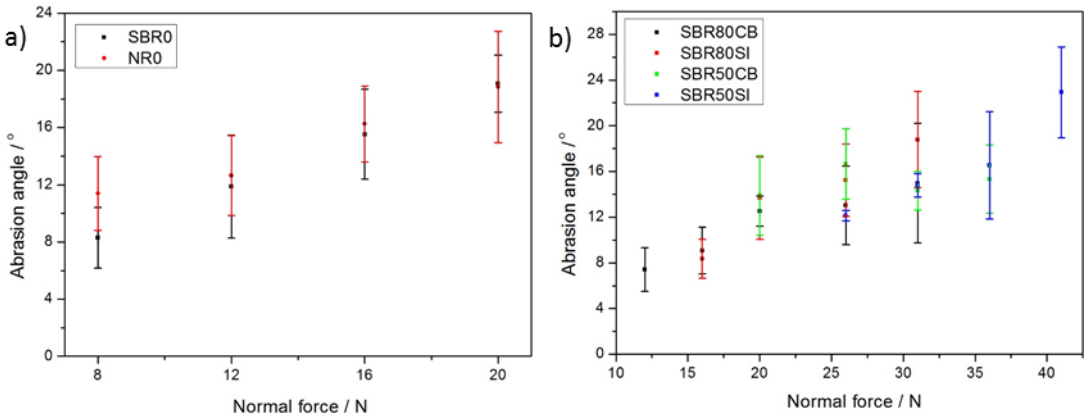

Figure 4-15. Abrasion angle as a function of normal force: a) for unfilled rubbers and b) for filled rubbers.

Figure 4-15 shows the abrasion angle as a function of normal force for unfilled rubber and filled rubber compounds which form an abrasion pattern. In general, the abrasion angle increased with the normal force for both unfilled and filled rubber compounds. The filled rubber materials have a much lower abrasion angle compared to the unfilled rubber under the same normal force possibly due to the reinforcement of the filler. The crack growth rates during the steady state of blade abrasion are shown in Figure 4-16. As expected, the crack growth rates rise with the normal load. Although SBR0 and NR0 have a similar abrasion angle, the crack growth rate for NR0 is greater than that for SBR0, which is probably a consequence of the abrasion process being too fast for the

reinforcing effects of strain induced crystallisation to be developed (Southern and Thomas, 1978).

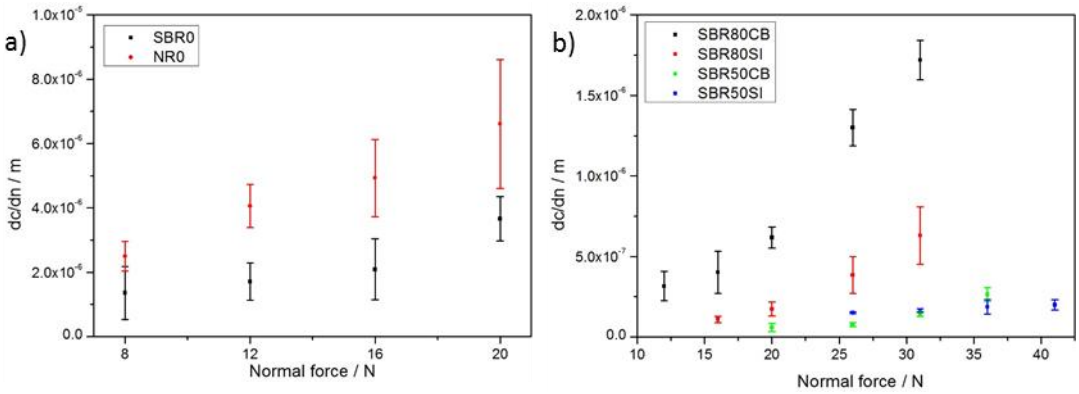

Figure 4-16. The crack growth rate as a function of normal force at steady state of blade abrasion: a) for unfilled rubbers and b) for filled rubbers.

4.3.4 Frictional Force and Derived Tearing Energy

The mean friction force was used to calculate the tearing energy during the blade abrasion using Equation 4-12 as proposed by Southern and Thomas (1978). Figure 4-17 shows the average friction coefficient for different normal forces. The friction coefficient decreases with the normal force. Since the blade has a wedged shape and the blade surface is quite blunt and smooth, the decrease of the friction coefficient is due to the limited increase of the real contact area between the blade and the rubber samples.

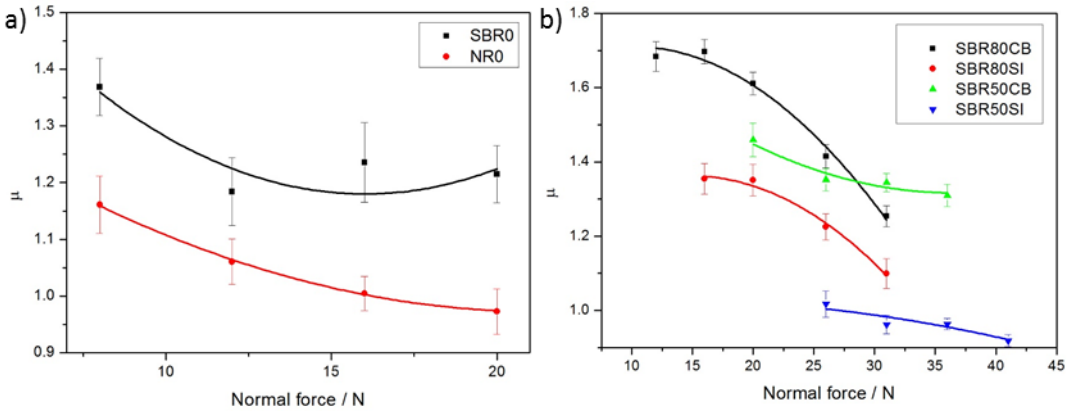

Figure 4-17. Friction coefficient as a function of normal force: a) for unfilled rubbers and b) for filled rubbers.

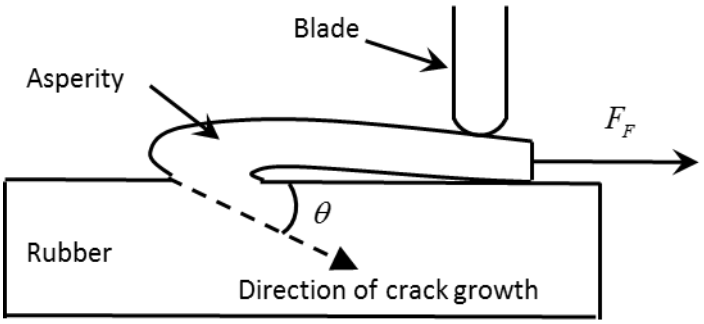

Figure 4-18. Fracture mechanics model of a blade pulling on an individual ridge under friction force F_F (re-drew from Southern and Thomas, 1978).

Table 4-2. Derived tearing energy during blade abrasion.

T / Jm^{-2}	Normal force / N							
	8	12	16	20	26	31	36	41
SBR0	1738	2236	3097	3781	-	-	-	-
NR0	1471	2012	2521	3030	-	-	-	-
SBR80CB	-	3215	4568	5094	5788	6122	-	-
SBR80SI	-	-	3449	4323	5098	5451	-	-
SBR50CB	-	-	-	4628	5544	6564	7403	-
SBR50SI	-	-	-	-	4185	4691	5431	5786

When the abrasion pattern is generated on the rubber surface, the abrasion process can be simplified into a simple model as shown in Figure 4-18. The rubber asperity which is assumed to be uniform across the rubber surface is deformed by the friction force F_F. If the crack at the root of the asperity propagates by $\mathrm{d}c$ at an angle θ, the distance that the friction force drive the asperity to move is $\mathrm{d}c\times(1+\cos\theta)$. The released stored energy $\mathrm{d}U$ is equal to the work done by the friction force. Therefore, $\mathrm{d}U$ can be expressed by:

$$\mathrm{d}U = F_F \times \mathrm{d}c \times (1+\cos\theta) \qquad \text{Equation 4-10}$$

The tearing energy can be derived as:

$$T = \frac{\mathrm{d}U}{h_0 \times \mathrm{d}c} \qquad \text{Equation 4-11}$$

where h_0 is the width of the specimen. Finally, the tearing energy for blade abrasion can be expressed as:

$$T = \frac{F_F}{h_0}(1+\cos\theta) \qquad \text{Equation 4-12}$$

The calcualted tearing energy is given in Table 4-2.

4.3.5 Effect of Loading Profiles on Cyclic Crack Growth Rate

The pure shear fatigue crack growth test results with three different loading profiles for SBR0 and NR0 are shown in Figure 4-19. As is the convention the crack growth rate per cycle is plotted against the maximum tearing energy achieved in a specific loading cycle using logarithmic scales. The broad behaviour for each of these three loading conditions on the crack growth rate for both SBR0 and NR0 is similar. In the case of non-strain crystallizing SBR, the crack growth during each cycle can be divided into two components, the time dependent contribution and cyclic contribution (Lake and Lindley, 1964). In this study, the time dependent contribution is responsible for the differences in the crack growth rate per cycle for the three different loading patterns. For NR0 which exhibits strain induced crystallisation at the large strains around the crack tip, the cyclic component dominates the crack growth behaviour and this has the effect of pulling the three different curves closer together. The crack growth rates at a specific tearing energy for these three loading profiles are therefore broadly equivalent, since the frequency difference is not significant.

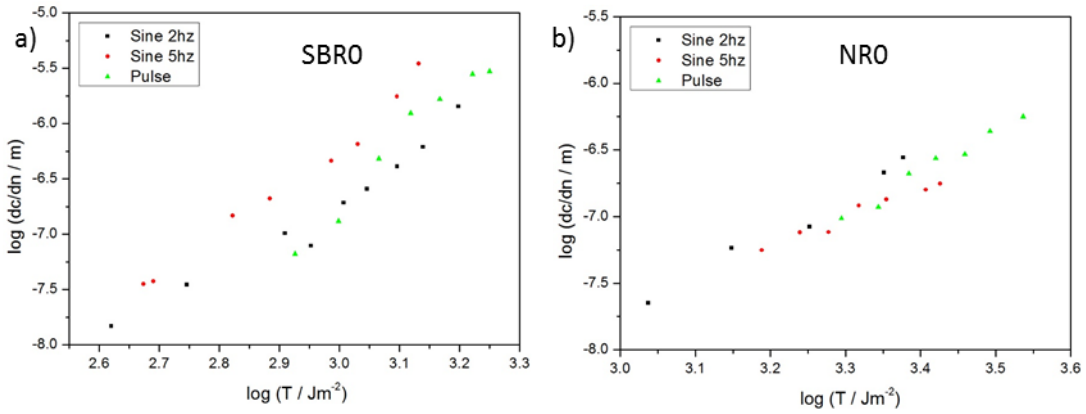

Figure 4-19. Effect of loading profile on cyclic crack growth rate for unfilled rubbers: a) SBR0 and b) NR0.

Figure 4-20 gives the effect of various loading configurations on the crack growth rate for filled rubber compounds. The detailed shape of the loading profile has a more complicated effect on the crack growth rate versus maximum tearing energy per cycle behaviour for the filled materials. The first observation being that the data points are much more scattered for the filled materials. There are often significant complications encountered whilst making these measurements whereby cracks split in multiple directions (which is known as crack tip branching) or the crack may even suddenly moves towards the clamps (which is known as knotty tearing). All these effects serve to make the crack propagation unsteady. The reasons for this are complicated but it is thought that the rubber molecules or the filler agglomerates become highly oriented at the tip of the crack. This strain induced anisotropy of the material results in the material becoming significantly weaker in a direction perpendicular to the direction that would be expected to release the maximum energy. This causes a deviation of the crack path from the obvious direction perpendicular to the applied strain to a direction that is parallel to the applied strain. This type of knotty tearing is shown in Figure 4-21. The introduction of these changes in the direction of the crack propagation significantly toughens the material and serves to reduce the cyclic crack growth rate. Therefore, the crack growth rate becomes unstable and becomes dependent upon the extent of any crack tip deviations. Figure 4-22 shows the increase in the horizontal crack length when this knotty tearing occurs with an R squared value of 0.97. For steady crack growth, the R squared value is over 0.99. This effect appears to be more significant for silica filled rubbers possibly due to the higher surface area of the silica used. Figure 4-23 shows the fracture surface for SBR0 and SBR50SI. As a consequence of these crack tip deviations during fatigue tearing the roughness of the fracture surface for the filled rubber is much larger than that for SBR0.

Cyclical loading to the same maximum displacement has a significant effect on lowering the stiffness of filled rubber compounds. This effect is known as cyclic stress softening. This significantly changes the stress distribution within the test specimen, especially around the crack tip where significant large stresses occur. As a fatigue test progresses, the local stress around the crack tip becomes lower from cycle to cycle and the stress

distribution becomes more uniform. This may result in a lower crack propagation rate, which may result in an unsteady crack growth rate.

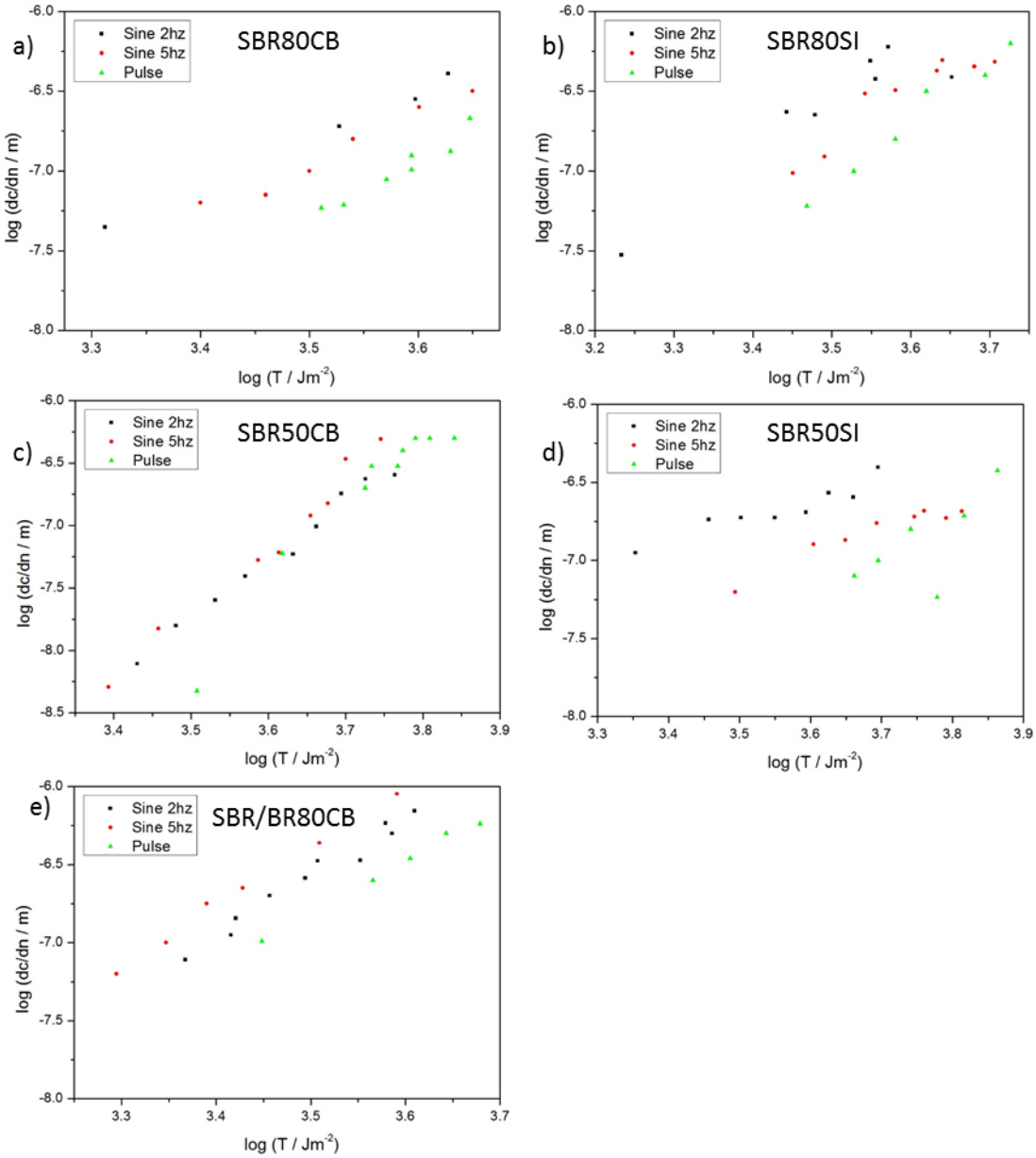

Figure 4-20. Effect of loading profile on cyclic crack growth rate for filled rubbers: a) SBR80CB, b) SBR80SI, c) SBR50CB, d) SBR50SI, and e) SBR/BR50CB.

The temperature effect is another factor that can influence the crack propagation for filled rubbers, since they are much more viscous than the unfilled rubbers. The temperature build up around the crack tip can significantly soften the material. As the loading rate increases, there is less time for heat dissipation. As a consequence, it can increase the crack growth rate. In addition, as a consequence of the viscoelastic mature

of the rubber, a higher loading rate can result in a much higher stress, which may also increase the crack growth rate. Both the strain induced anisotropy, cyclic stress softening and the temperature build up at the crack tip affect the crack propagation for the filled materials.

With all this considered though it is clear that the general trend for most of the filled materials is that the pulse loading is the least damaging per cycle compared to both sinusoidal loading cases. Also when the experimental difficulties have been considered it is also clear from the sinusoidal tests for SBR80CB, SBR80SI and SBR50SI that the slower loading rate is the more damaging of the two sinusoidal loading patterns. This also suggests that a time-dependent contributions to the fatigue is important to these materials. For the other two materials, the temperature effect at the crack tip possibly balance out the effect of the increased frequency.

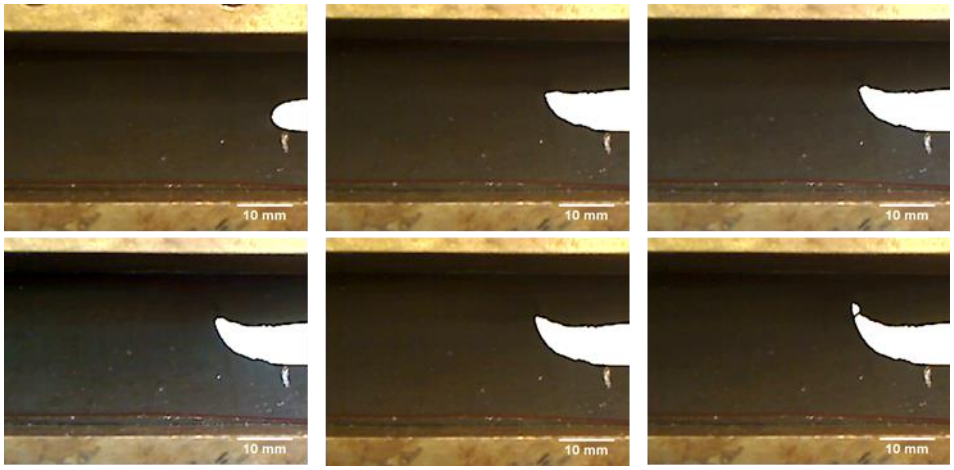

Figure 4-21. Change of the direction of crack growth path for SBR80CB during the pure shear fatigue crack growth test.

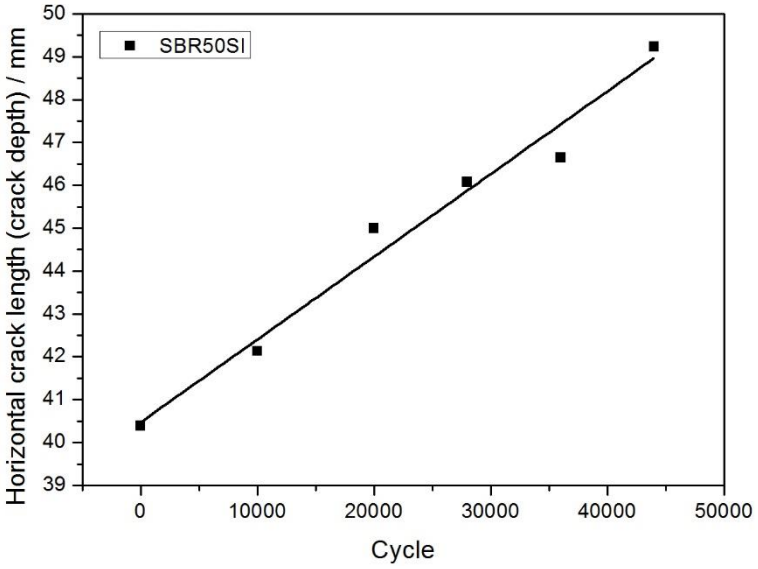

Figure 4-22. Horizontal crack length (crack depth) against number of cycles when knotty tearing occurs.

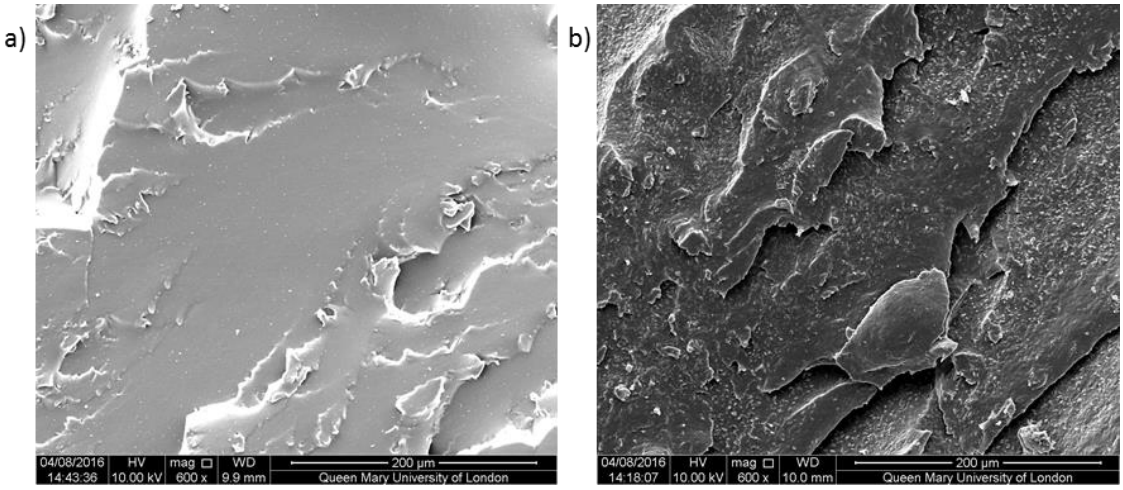

Figure 4-23. SEM images of fracture surface of pure shear fatigue crack growth test for a) SBR0 and b) SBR50SI.

4.3.6 Correlation of Blade Abrasion with Pure Shear Fatigue Crack Growth Test

An attempt has been made to correlate the blade abrasion results to the pure shear fatigue crack growth test results. Since the three different loading configurations only had a modest effect on the crack growth rate. The pulse loading configuration was chosen as the representative data from the pure shear fatigue crack growth test. The correlation for the SBR0 and NR0 is shown in Figure 4-24. In these graphs the best fit line

from the crack growth data is shown together with experimental data points that are taken from the abrasion tests. In this case, the tearing energy is calculated during abrasion using Equation 4-12 and the crack growth rate is measured experimentally as described in section 4.3.3. For four filled compounds which generated abrasion patterns, the correlation is given in Figure 4-25.There was a reasonable correlation for SBR0 as shown in Figure 4-24 a), which indicated that the fundamental abrasion mechanism was one of fatigue crack growth. However, for NR0 shown in Figure 4-24 b) the crack growth rate during abrasion was much greater than that measured from the fatigue test. For filled compounds, the agreements are also relatively reasonable since they are all SBR based rubber materials.

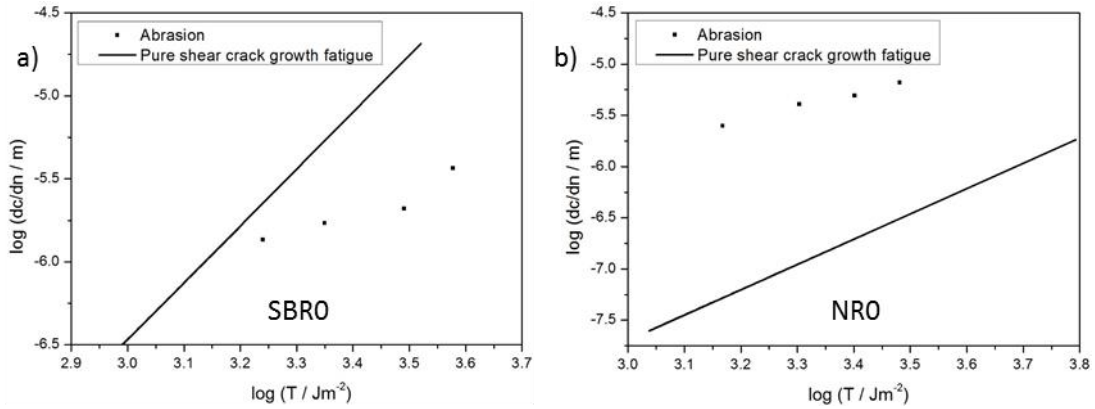

Figure 4-24. Correlation between the blade abrasion results and pure shear fatigue results for a) SBR0 and b) NR0.

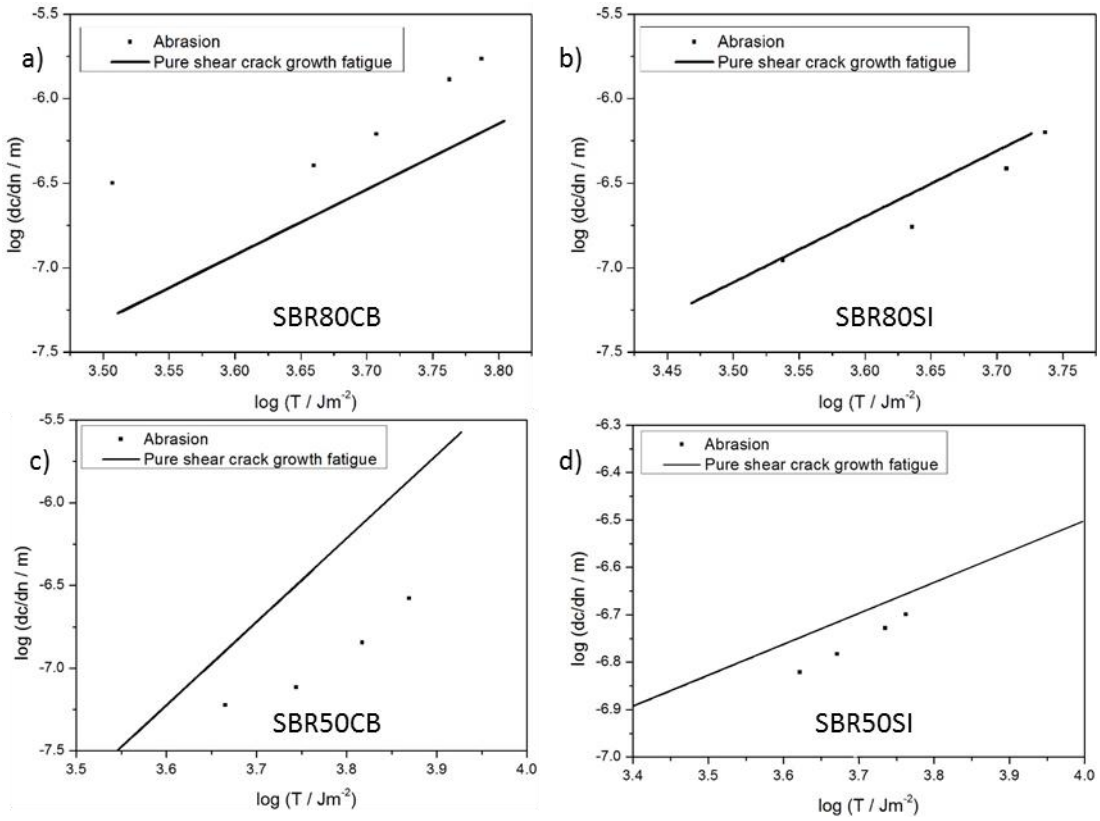

Figure 4-25. Correlation between the blade abrasion results and pure shear fatigue results for a) SBR80CB, b) SBR80SI, and c) SBR50CB.

The discrepancy between the two set of data might arise in two parts, non-identical loading conditions and an inaccurate approximation of the tearing energy. The loading rate during abrasion is extremely high. For NR materials, that gives insufficient time for crystallization to occur (Southern and Thomas, 1978, Liang et al., 2009). Alternatively, the substantial initial compression during the abrasion test is not reproduced in the pure shear fatigue crack growth tests. It is possible that this compression might also help suppress any crystallization. The other potential reason for a poor correlation might result from the equation given by Southern and Thomas being only an approximate relationship for the tearing energy. Since friction is directly linked with abrasion, the frictional force between the tongue and the blade has to be correctly accounted for as the driving force the crack growth. Large abrasion loss usually results from large friction force, otherwise no abrasion would occur such as for material polytetrafluoroethylene (PTFE) which has a very low friction coefficient. To make a better correlation a more

accurate method of determining the tearing energy using a FEA technique is required, which is developed in the next chapter.

4.4 Summary and Conclusions

Two mechanisms were observed during for blade abrasion. Smearing wear occurred during the initiation state and a fatigue wear mechanism dominated the abrasion process whereby an abrasion pattern was generated on the rubber surface. It was proposed that the two mechanisms were competitive with each other. When the crack growth resistance was poor as was the case for SBR0, the abrasion pattern was easily formed and no smearing wear was observed. Otherwise, initial smearing wear was slowly overtaken by the fatigue wear pattern. Both the abrasion angle and the abrasion rate increased with the normal load. There was a generally good agreement between the blade abrasion results and the pure shear fatigue crack growth results for a non-crystallizing SBR material. For NR0, probably due to the suppression of the crystallization during the very rapid abrasion process, the correlation was worse. The effect of the loading profiles on the crack growth rate for the three different loading profiles used in this study was only modest with the broad ranking being as expected for materials that contains a time dependent contributions to crack growth in each loading cycle. On reflection it would have been better to have had a much wider range between the various loading configurations that were evaluated. However that would have presented experimental difficulties as testing at lower frequencies can take a very long time to complete and a loading at faster than the pulse rate applied in this study would not be possible using our existing fatigue test machines.

5 Chapter Five: Estimation the Tearing Energy for Fatigue Wear Using Virtual Crack Closure Technique

5.1 Introduction

The previous chapter described an apparent discrepancy between the measured abrasion crack growth and that predicted from the fatigue crack growth data. This discrepancy is potentially partly due to the imprecision of determining the tearing energy at the asperity during blade abrasion. The rapid and complicated deformation of the rubber asperity results in a big challenge. Although the equation proposed by Southern and Thomas (1978) gives an approximate indication of the tearing energy, it is only an approximation and it is still of importance to calculate the tearing energy during abrasion precisely.

Using FEA, it is possible to solve these types of complex problem without the necessity of applying too many gross simplifications required to derive a suitable analytical equation. This technique has been used in the past to predict crack growth behaviour in rubber materials reliably using a fracture mechanics approach (Busfield et al., 1996, Busfield and Thomas, 1999, Coveney and Menger, 1999, Busfield et al., 2005). There are three finite element based approaches for the calculation of tearing energy: the J-integral, energy balance and crack tip closure approaches (Busfield et al., 1999). Liang (2009) used an energy balance approach to calculate the tearing energy at the steady state during blade abrasion. In this approach two theoretically identical models were created, without a crack and with a crack. The difference between the total stored energy in these two models was taken as the energy available to propagate the crack. However, in practice it was impossible to have two virtually identical models. As a consequence, the energy difference might be due to the mesh difference between the two models. In addition, the energy difference had to be significantly larger than the artificial energy (energy required to stabilise the simulation) to have a reasonable result. The J-integral method is another widely used approach to calculate the tearing energy. However, it is only implemented in the ABAQUS Implicit. Since the abrasion processes

involves complex contact issues with rapid deformations, the explicit method is the only option to complete the simulation. Therefore, the J-integral was not used in this study.

In this chapter, for the first time, a Virtual Crack Closure Technique (VCCT) is described that can be used to calculate the tearing energy at the tip of the asperity during a blade abrasion type of process. All the numerical analyses were conducted using the explicit dynamics finite element package ABAQUS Explicit, 6-13. The relationships between the measured rate of abrasion and the calculated tearing energy were compared to the experimentally measured crack growth rate against tearing energy for unfilled SBR and NR under fully relaxing pure shear fatigue test to validate this method.

5.2 Introducing the Virtual Crack Closure Technique (VCCT)

5.2.1 One-step VCCT and Two-step VCCT

The principal assumption when using the VCCT is that the energy released when a crack is extended is equal to the energy required to close up the crack (Krueger, 2004). The VCCT is originally developed from the crack closure method, which is also now known as a two-step virtual crack closure technique. The crack closure method is based on Irwin's crack closure integral (Krueger, 2004). For this approach, the crack is modelled at two different lengths during two separate and complete finite element analysis. Figure 5-1 illustrates this approach whereby a crack is extended by a length Δa from node l to node i. The energy ΔU required to close the crack can be calculated as:

$$\Delta U = \frac{1}{2}\left(X_{1l}\Delta u_{2l} + Z_{1l}\Delta w_{2l} \right) \qquad \text{Equation 5-1}$$

where X_{1l} and Z_{1l} are the nodal force along X and Z directions at point l to be closed as shown in Figure 5-1 a) and Δu_{2l} and Δw_{2l} are the displacement differences between node l and node l' in X and Z directions shown in Figure 5-1 b).

The one-step VCCT assumes that a crack extension Δa does not significantly change the displacement field at the crack tip since Δa is infinitesimally small, when compared to the overall test piece geometry. As a result, the relative displacement at the crack tip

$\Delta v(\Delta a)$ can be treated as the relative displacement behind the crack tip $\Delta v(0)$ as shown in Figure 5-2. Therefore, as shown in Figure 5-3 the energy released when a crack is extended by Δa can be expressed as:

$$\Delta U = \frac{1}{2}\left(X_i \Delta u_l + Z_i \Delta w_l\right) \qquad \text{Equation 5-2}$$

where X_i and Z_i are the forces at nodal point i and Δu_l and Δw_l are the opening displacement at node l as shown in Figure 5-3.

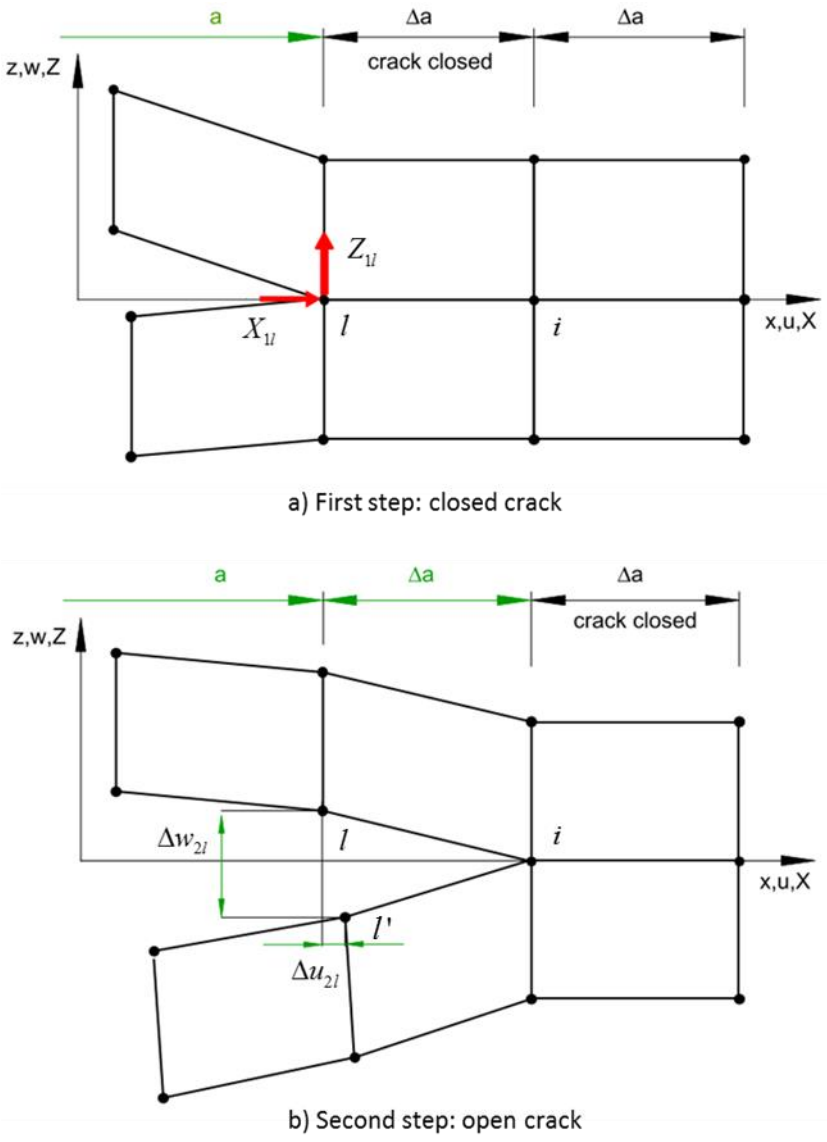

Figure 5-1. Two-step VCCT (Krueger, 2004).

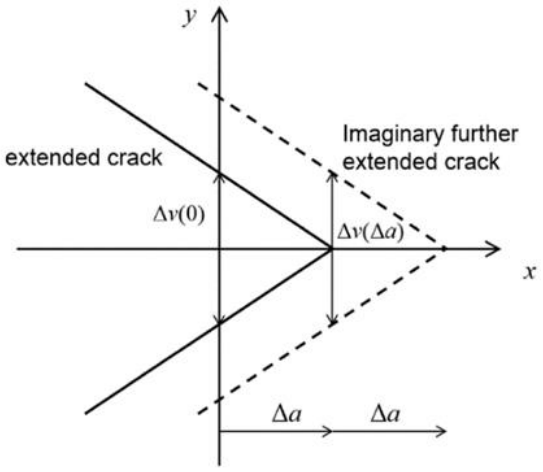

Figure 5-2. Self-similarity assumption in one-step VCCT (Mukaiyma, 2014).

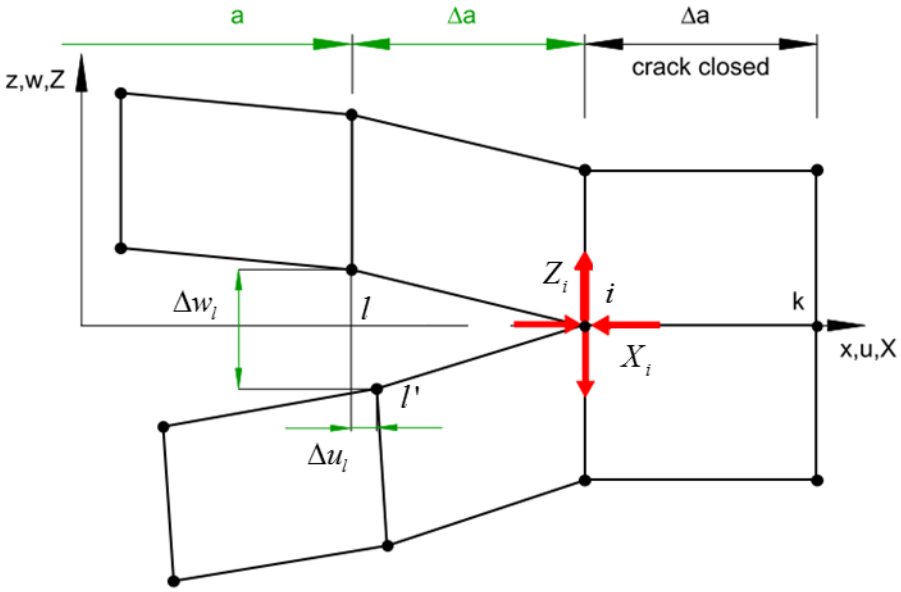

Figure 5-3. One-step VCCT (Krueger, 2004).

5.2.2 Nonlinear Analysis

There are two factors that contribute to the nonlinearities to a FEA model of rubber abrasion. One arises from the nonlinear elasticity of rubber material. The other arises from the geometric nonlinearity effect at the crack tip where a large deformation arises. In the case of geometric nonlinear analysis, both forces and displacements obtained in the global coordinate system need to be transformed into a local coordinate system,

which originates at the crack tip as shown in Figure 5-4 (Krueger, 2004). Thus the energy released as the crack is extended is expressed as:

$$\Delta U = \frac{1}{2}\left(X'_i \Delta u'_l + Z'_i \Delta w'_l \right) \qquad \text{Equation 5-3}$$

where X'_i and Z'_i are the forces at the crack tip in the local crack tip coordinate system, and $\Delta u'_l$ and $\Delta w'_l$ are the relative displacements behind the crack tip also in the local crack tip coordinate system. Taking into account the materials nonlinearities from the rubber itself, the equation requires a full integration as given here:

$$\Delta U = \int X'_i du'_l + \int Z'_i dw'_l \qquad \text{Equation 5-4}$$

The tearing energy is then calculated as the rate of energy change per unit increase in the crack length using Equation 2-24.

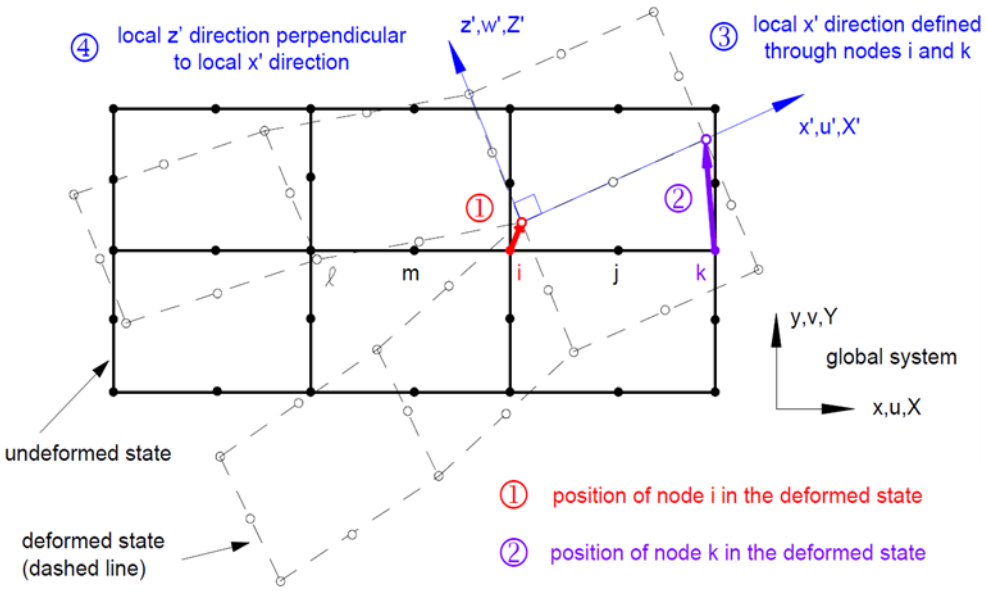

Figure 5-4. Definition of local crack tip coordinate system (Krueger, 2004).

5.3 Defining the Finite Element Model for Blade Abrasion

5.3.1 Model Assumption

Some assumptions have been made in order to simplify the analysis for the FEA models, as suggested by Liang (2007).

- All the materials for FEA models are assumed to be fully elastic and the viscoelastic contribution is ignored;
- No material is removed from the FEA model;
- The frictional force applied at the interface between the abrader and the rubber is a combination of surface adhesion and the ridge deformation;
- The crack is presumed to propagates at the root of the rubber asperity when the tearing energy reaches a maximum;
- The deformation of the abrasion pattern ridge is similar all around the rubber surface.

5.3.2 Material Modelling

Since all the materials in FEA model are assumed to be hyperelastic, only the unfilled rubber materials SBR0 and NR0 were modelled to minimise the viscoelastic contribution. The detailed formulation of the materials used is given in Table 4-1. Simple hyper-elastic Mooney-Rivlin SEFs were used to model the unfilled rubbers as recommended by Kumar et al. (2007). As discussed in section 2.4, this SEF is given as:

$$W = C_1(I_1 - 3) + C_2(I_2 - 3) \qquad \text{Equation 2-9}$$

In the case of uniaxial extension, the relationship can be rearranged as:

$$\sigma^* = \frac{\sigma}{\left(\lambda - \lambda^{-2}\right)} = 2\left[\left(\frac{\partial W}{\partial I_1}\right) + \frac{1}{\lambda}\left(\frac{\partial W}{\partial I_2}\right)\right] \qquad \text{Equation 5-5}$$

where σ is the engineering stress given as the force divided by the unstrained cross section area of the test pieces; σ^* is known as the reduced stress. Substituting Equation 2-9 into Equation 5-5, half of the reduced stress can be expressed as:

$$\frac{\sigma^*}{2} = \frac{\sigma}{2\left(\lambda - \lambda^{-2}\right)} = C_1 + \frac{C_2}{\lambda} \qquad \text{Equation 5-6}$$

The stress-strain behaviour for SBR0 and NR0 is plotted in the form of the engineering stress versus extension ratio as shown in Figure 5-5. Then the data is replotted as half of the reduced stress against to the reciprocal of the extension ratio as shown in Figure 5-6.

The SEF coefficient C_1 and C_2 was determined as the intercept and the slope of the approximately linear region in Figure 5-6. A finite compressibility was introduced in the material model as bulk compliance, D_{com}, shown as:

$$D_{com} = \frac{2}{E_B} \qquad \text{Equation 5-7}$$

where E_B is the bulk modulus of the rubber materials. The coefficients for SBR0 and NR0 are shown in Table 5-1.

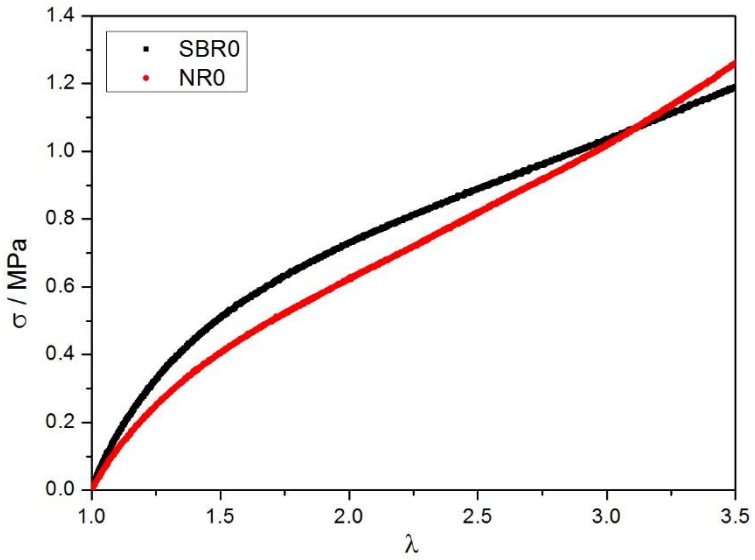

Figure 5-5. The engineering stress versus extension ratio for SBR0 and NR0.

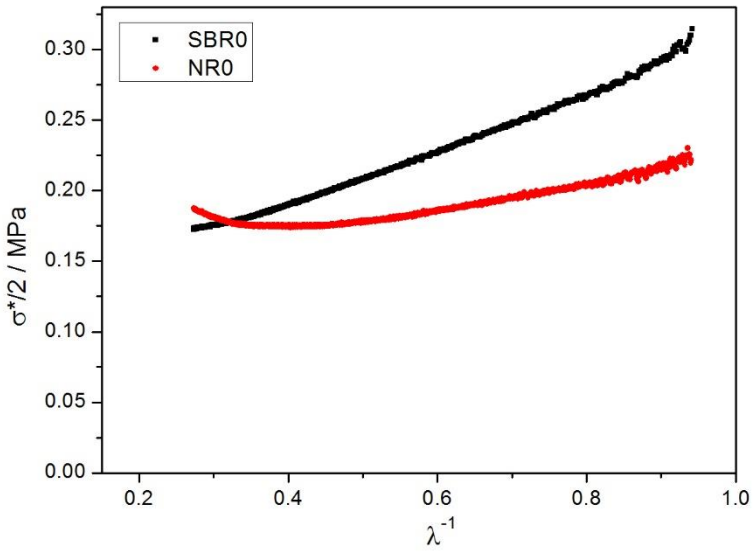

Figure 5-6. Half reduced stress against to reciprocal of extension ration.

Table 5-1. Mooney-Rivlin SEF coefficients, bulk compliance and density.

Materials	C_1 / MPa	C_2 / MPa	D_{com} / MPa^{-1}	ρ / 10^3 kgm^{-3}
SBR0	0.145	0.174	0.07	0.996
NR0	0.188	0.072	0.065	0.998

5.3.3 Model Dimensions

Once the abrasion pattern was fully developed on the rubber surface at the steady state, a photograph of the cross section of the abrasion pattern was taken to measure the dimensions of asperities as shown in Figure 5-7. Only one asperity was taken as a representative for the FEA model as shown in the Figure 5-8. The asperity was modelled as being on the upper surface of a rectangular rubber block. To avoid edge effects, the length of the rectangular rubber block was 10 times bigger than the width of the maximum width of the ridge. Therefore, for NR0 the block of rubber is 10 mm long and 5 mm high. And for SBR0 it is 20 mm long and 10 mm high as SBR0 produced a larger asperity size. The geometry of the model is presented in Figure 5-8.

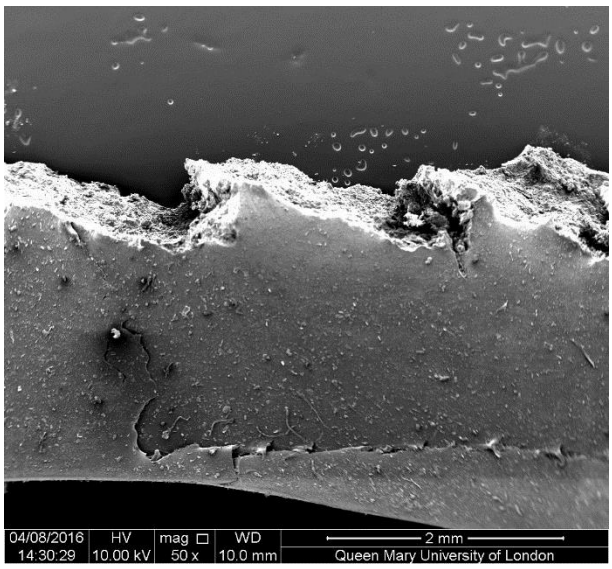

Figure 5-7. Typical asperities of the abrasion pattern of NR0 under 20 N normal force.

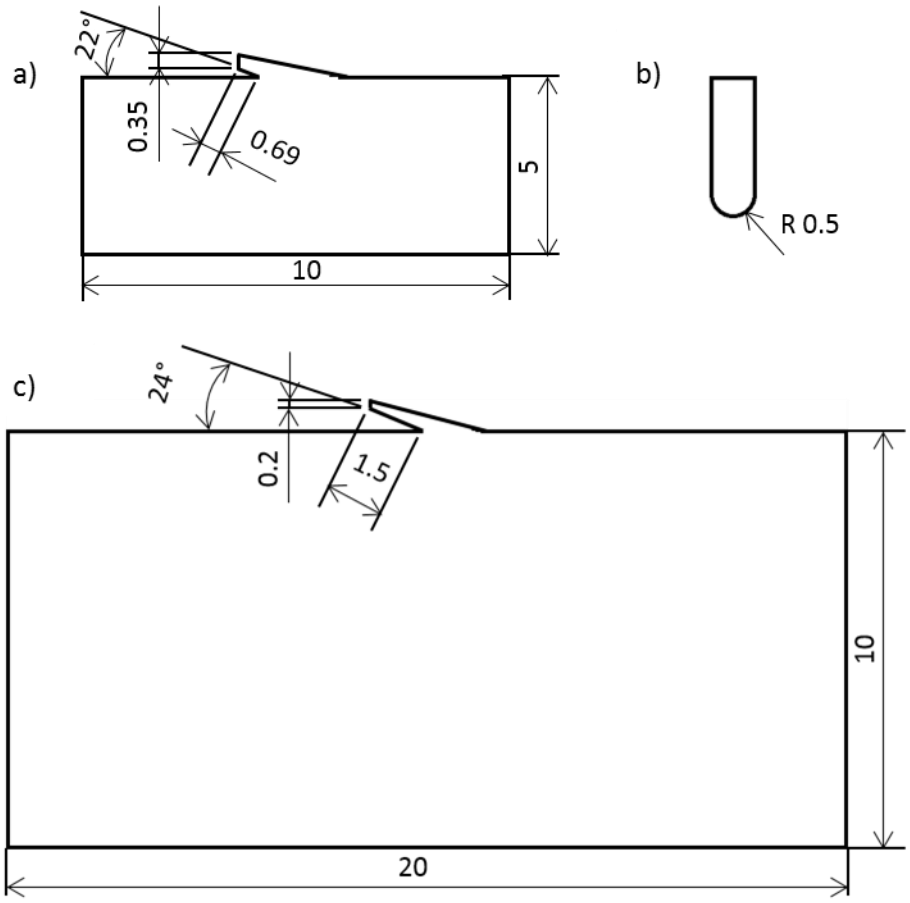

Figure 5-8. Dimensions of FEA models in mm; a) NR0, b) blade, c) SBR0.

As the blade is much stiffer than the rubber materials, it was modelled as an analytical rigid surface. In the actual blade abrasion experiment, a razor blade was used as the abrader. However, it was found that a sharp edged blade significantly increased the instability of the model due to the mesh resolution issues (Liang, 2007). Since the tip sharpness has little effect on the abrasion rate once the abrasion pattern is formed as discussed in section 3.3, the blade was modelled semi-circle slider with 0.5 mm radius.

Since the thickness of the sample was far greater than the cross sectional dimension for one single asperity, the change in thickness due to Poisson's ratio effects was negligible. In other words, a plane strain approach was used whereby the strain only exist in the x-y plane. Therefore, all the models were created using two dimensional plane strain elements with a prescribed element thickness that reflects the thickness of the wheel of 12.5 mm.

5.3.4 Boundary Conditions

The bottom side of the rubber block was restricted in motion in both the x and y directions. On both vertical edges, the displacement was only allowed in the vertical direction and the horizontal displacement of the nodes was restricted. The top surface was set to be free to allow any kind of deformation. Boundary conditions were also imposed to the abrader to implement the abrasion process in two steps. The first step was the indentation, which the abrader was initially moving down vertically to compress the rubber surface until the required normal force was reached. In the second step the abrader was set to slide against to the rubber asperity at 70 mm/s while maintaining the vertical displacement.

5.3.5 Contact Conditions

As the FEA models are assumed to be fully elastic, the friction force only comes from two contributions, adhesion friction and deformation friction, respectively. The adhesion component is decided by the friction law applied to the model. A surface to surface contact pair was defined between the surface of the abrader and the top surface of the rubber. A classical isotropic Coulomb friction model with 0.2 friction coefficient was used. The reason for choosing 0.2 is given in section 5.4.2. A self-contact constraint was also defined to the rubber surface with the friction coefficient of 1.0 as suggested by Liang (2009).

5.3.6 Algorithms and Element Selection

All the numerical models in this study are implemented in the finite element software ABAQUS. ABAQUS provides several algorithms for solving different problems. For rubber materials, since it involves dramatic nonlinear effects, only direct integration methods, implicit and explicit methods are suitable (Sun et al., 2000).

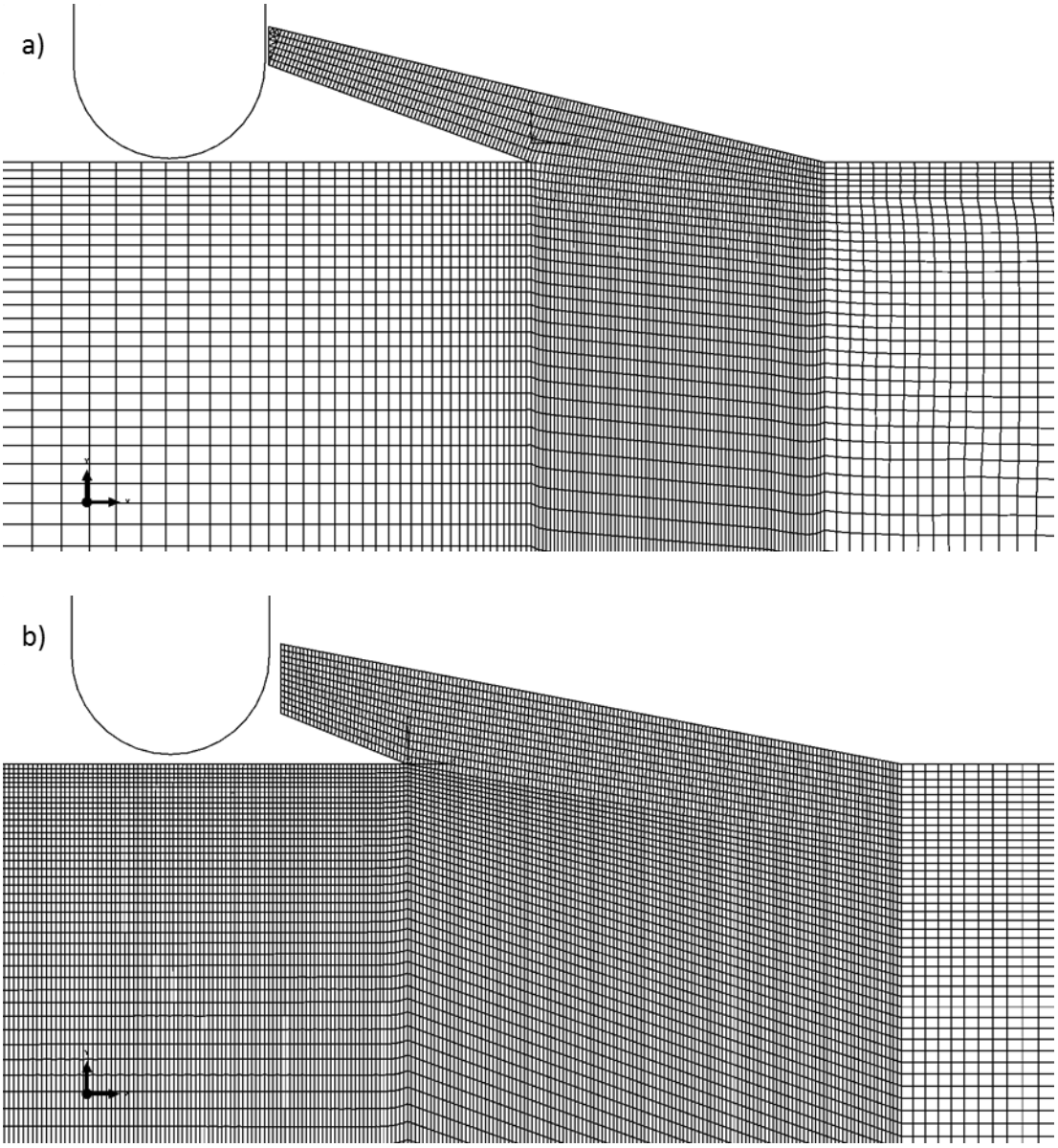

Figure 5-9. Meshed model of single rubber asperity with a blade for a) SBR0 and b) NR0.

The implicit method uses an automatic increment strategy based on the success rate of a full Newton iterative solution method. This method has been applied previously to investigate fracture behaviour in rubber materials for example to predict the fatigue life of three dimensional elastometric components (Busfield et al., 2005). However, when applying implicit scheme to this particular problem, there were significant mesh convergence difficulties due to the complicated contact conditions in combination with the rather rapid loading rate.

To overcome these difficulties an explicit scheme was developed, which was based on the implementation of an explicit integration rule along with the use of diagonal element mass matrices. This approach proved more suitable for solving these types of complex contact problem under rapid deformations. Therefore, all the numerical analyses were conducted using the explicit dynamics finite element package ABAQUS Explicit, 6-13. Two dimensional plane strain reduced integration elements with hourglass control (CPE4R) were mainly assigned to the mesh. The finite element meshes used are shown in Figure 5-9.

5.3.7 Crack Tip Modelling

The extended crack was modelled by opening one element at the root of the rubber asperity at an abrasion angle θ to the horizontal. This was done by introducing a seam at the crack tip, which allowed two nodes to have identical coordinates as shown in Figure 5-10. The abrasion angle θ modelled was determined from the blade abrasion experiment at each different normal force.

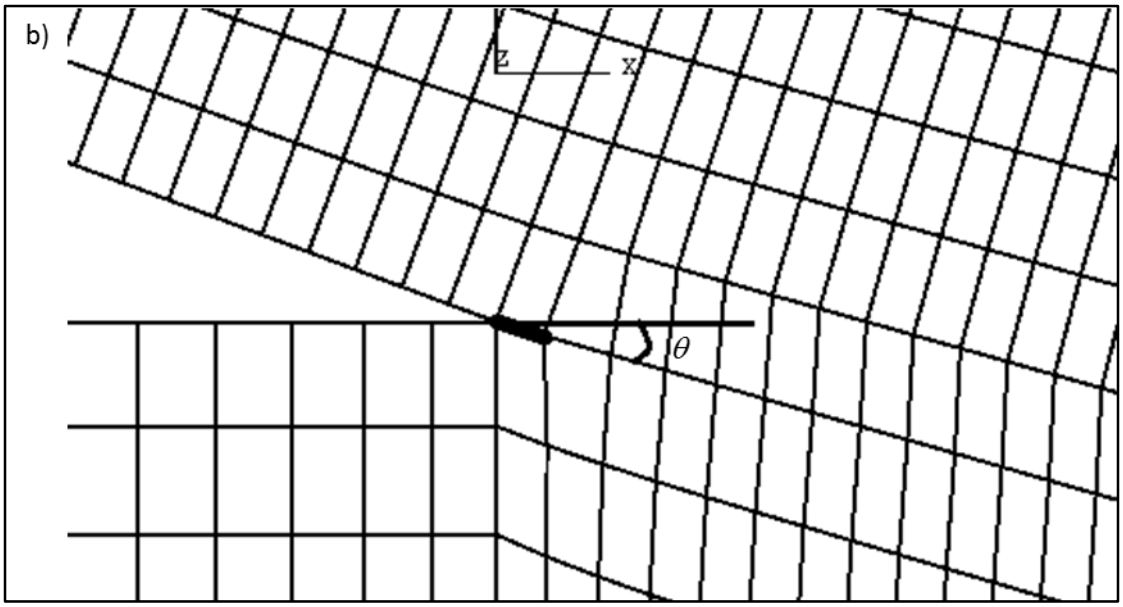

Figure 5-10. Zoom in of the root of the asperity with extended crack indicated by the thick line.

5.4 Results and Discussion

5.4.1 The Rubber Asperity Deformation

Figure 5-11 to Figure 5-14 show the deformation of the rubber asperity as the blade slider passes through with the friction coefficient set at 0.2 in the model to reproduce the experimentally measured value for frictional force, which is explained in the next section. The slider was moving down vertically to indent the rubber until the required normal force was achieved. Next the asperity contacted the abrader, as the abrader was sliding against the rubber surface at a velocity of 70 mm/s whilst maintaining the required vertical displacement. The rubber asperity eventually buckled and the tail was compressed at the point where the horizontal force reached a maximum. Finally the asperity was released from beneath the abrader.

A high speed camera was used to record the actual deformation of a single asperity during the blade abrasion. The video captured images are shown in Figure 5-15. Although only one side of the blade can be seen, the actual deformation of the rubber asperity during blade abrasion is very similar to that predicted using the FEA. Therefore, it was anticipated that the FEA model can simulate the actual deformation of the rubber asperity.

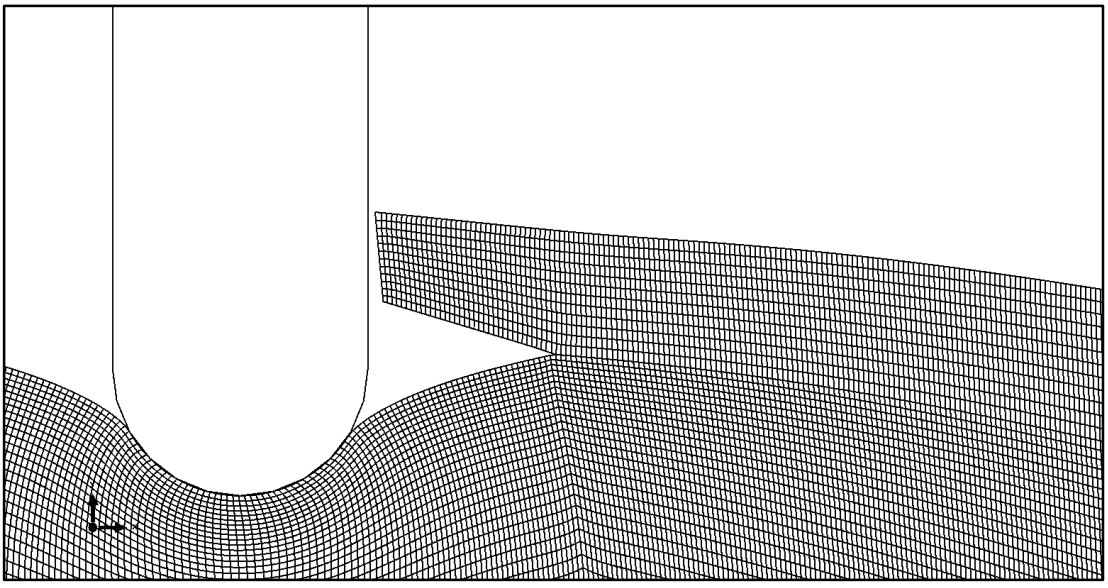

Figure 5-11. The abrader indented the rubber to apply normal force.

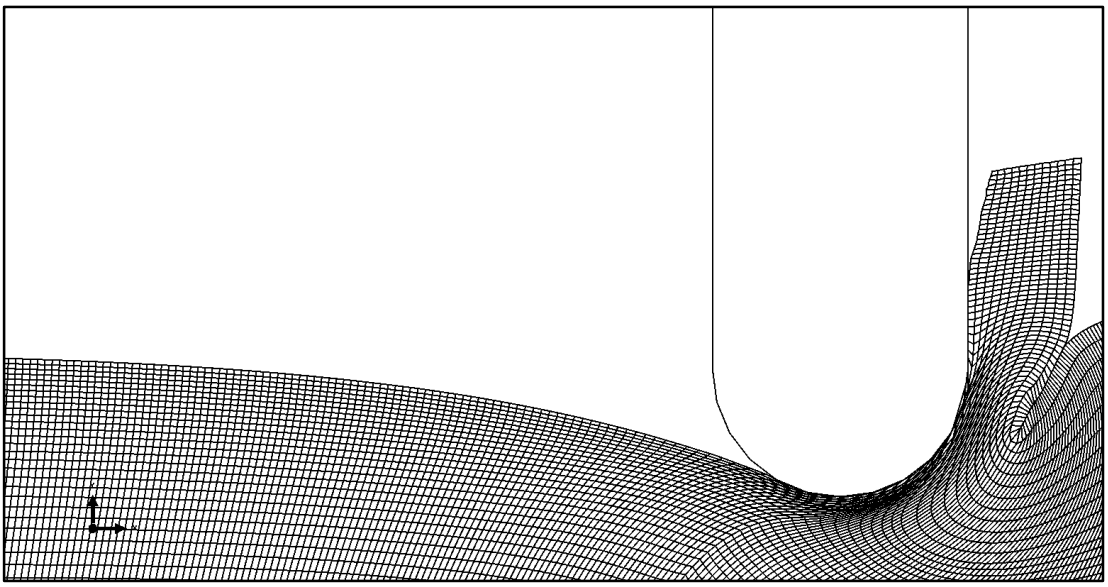

Figure 5-12. The abrader slid horizontally to stretch the asperity.

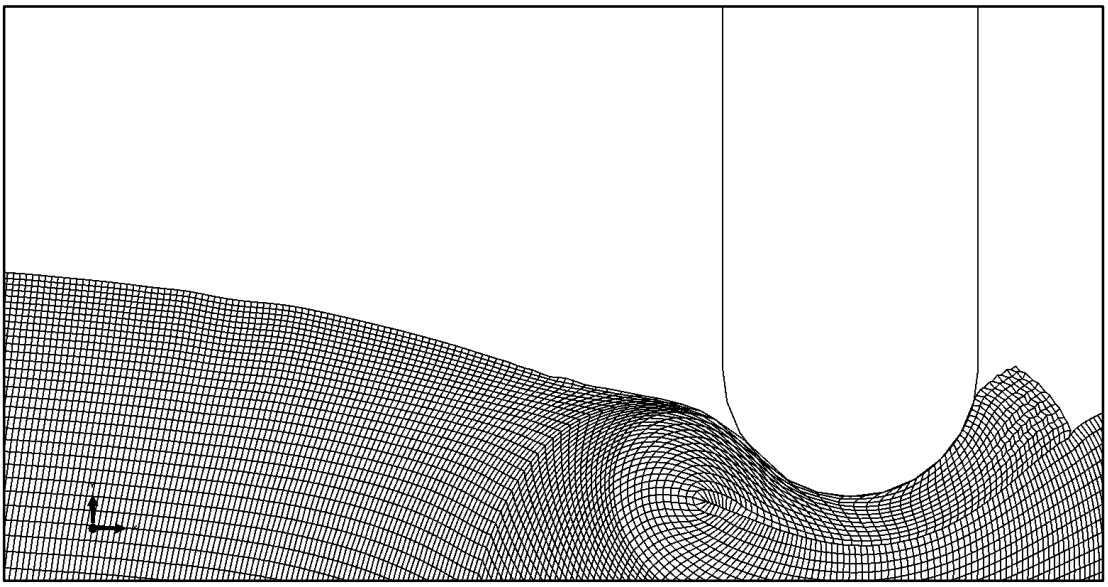

Figure 5-13. The asperity was bulked and compressed by the abrader.

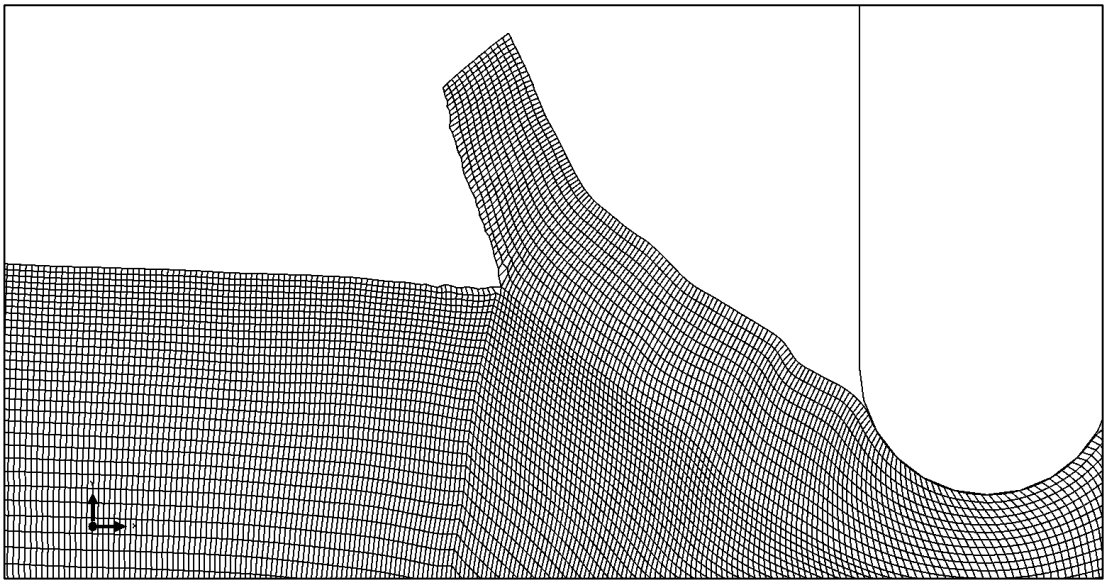

Figure 5-14. The asperity was released from the bottom of the abrader.

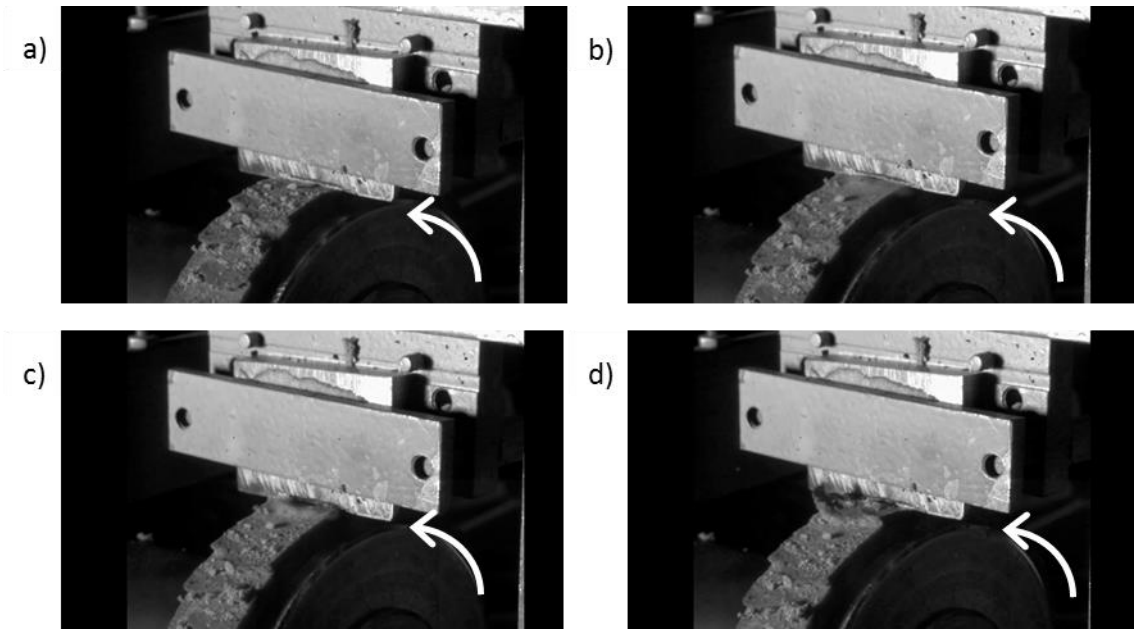

Figure 5-15. Images captured using a high speed video camera (arrow shows the rotation direction of the wheel): a) the blade was reaching an asperity; b) blade was stretching the asperity; c) the asperity was just releasing from the blade; d) the asperity fully was released.

5.4.2 Frictional Behaviour in FEA Models

The friction force between the blade and rubber during the abrasion tests is represented as the horizontal reaction force in the FEA model. As discussed before, the total friction force consists of two different components, the adhesion contribution μ_{ad} and the

deformation contribution μ_{def} . The adhesion contribution is defined by the Coulomb friction law between the abrader and rubber surface. The deformation friction results from the deformation of the rubber, since all the rubbers are assumed to be perfectly elastic.

Different values of μ_{ad} were tried in the FEA model in order to generate a reasonable friction force that reflected the value measured experimentally. Figure 5-16 shows the output friction force as a function of the horizontal displacement of the abrader for SBR0 at 8 N normal force, when the μ_{ad} is 0.2. The friction force reached maximum just before the asperity buckled. This maximum friction point also correlates the largest value for the tearing energy, as is discussed in the next section. Therefore, the maximum friction value deduced from this model is taken throughout to correlate the measured friction force during the abrasion test. Figure 5-17 gives the correlation of the predicted force and the measured friction force for SBR0 with the μ_{ad} equal to 0.2. A good correlation is obtained. As a result, the friction coefficient between the abrader and the rubber is chosen as 0.2 for both SBR0 and NR0.

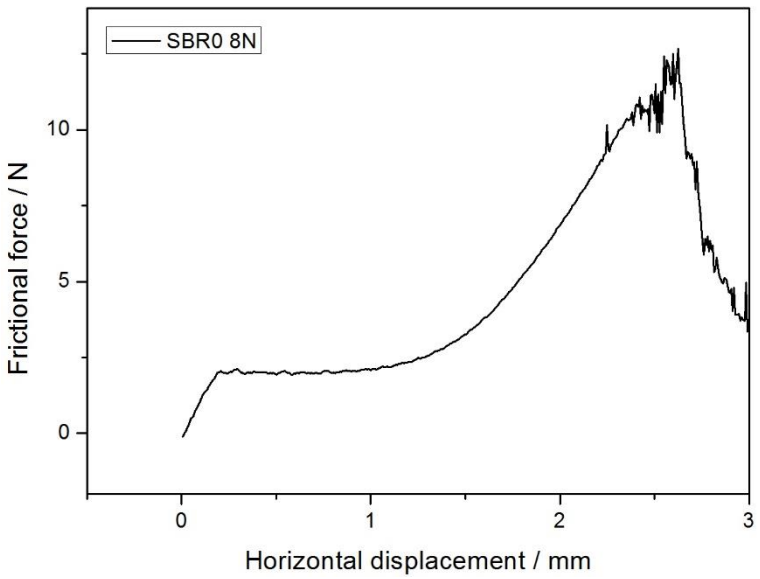

Figure 5-16. Frictional force as a function of horizontal displacement for SBR0 for 8 N normal force, $\mu_{ad} = 0.2$.

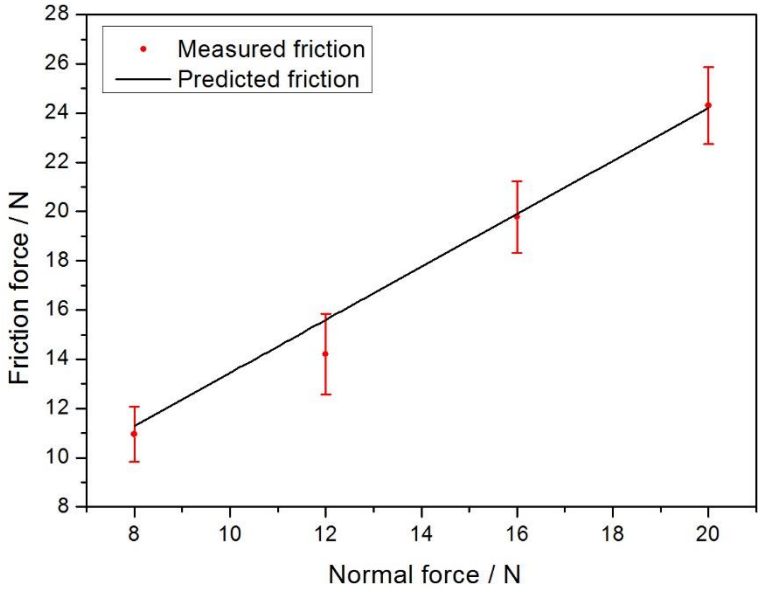

Figure 5-17. Correlation of the predicted friction force and the measured friction for SBR0.

5.4.3 Tearing Energy Derived Using VCCT

Prior to using the derived tearing energy from the VCCT approach, the mesh convergence of the FEA model was checked to validate that an appropriate mesh density was being applied. The VCCT was used to predict the tearing energy of models using a different mesh density. Table 5-2 shows the effect of mesh sensitivity on the tearing energy for the SBR0 model at a 16 N normal force. The tearing energy was independent of the mesh density of the model when the number of elements was more than 8000. Therefore, a mesh density with 8480 element was used in this model to predict the tearing energy. Similar procedures were used to validate all the models for each material under all the loading conditions to determine the mesh density.

Table 5-2. Mesh sensitivity for the model of SBR0 at 16N normal force.

Global seed size / mm	Total elements	Tearing energy / kJm^{-2}
0.2	6760	2.1
0.15	8480	2.6
0.1	11420	2.5

The final tearing energy was calculated as described in Section 5.2.2 using Equation 5-4 and Equation 2-24. The elastic stored energy during the abrasion process is shown for example in Figure 5-18 for NR0 at 12 N. It started to increase when the abrader compressed the asperity and reached the maximum just before the asperity buckled. The maximum stored energy was chosen for the calculation of the tearing energy. The tearing energy derived from VCCT was compared to that calculated using Equation 4-12 proposed by Southern and Thomas (1978). Both of them were then used to correlate the pure shear fatigue tests as shown in the previous chapter. The results of this comparison are shown in Figure 5-19 and Figure 5-20 for SBR0 and NR0 respectively.

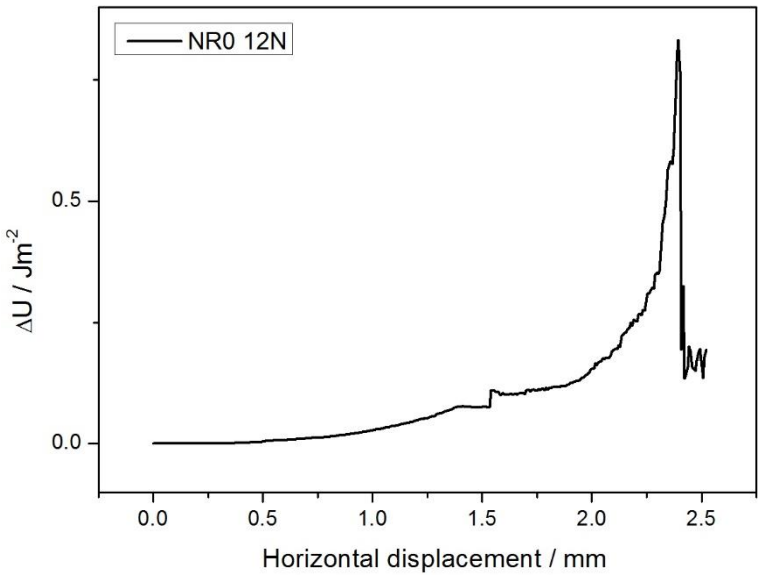

Figure 5-18. Elastic stored energy as a function of horizontal displacement of the slider for NR0 at a 12 N normal force.

A better correlation for the tearing energy calculated from VCCT to the pure shear fatigue test is obtained for SBR0, which suggests that the VCCT approach predicts the tearing energy more reliably than Equation 4-12. Equation 4-12 assumes all the friction forces during the abrasion are applied to drive the propagation of the crack at the root of the abrasion pattern. However, a contribution to the friction is also used to deform the rubber asperities. Therefore, the contribution of the friction force to the crack growth is probably overestimated (Liang, 2007). In the case of NR0, although the tearing energy derived from VCCT gives relatively less agreement to the pure shear fatigue test than SBR0, it still works better than the equation. As discussed in Chapter 4, it is possible

that the strain induced crystallisation is not fully developed during the very rapid abrasion test, which could explain the poor correlation.

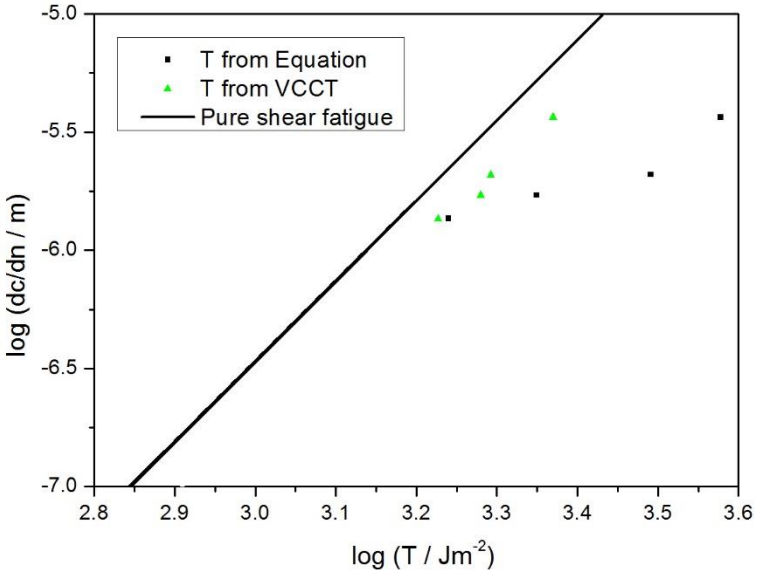

Figure 5-19. The correlation of the tearing energy derived from VCCT, Equation 4-12, and pure shear fatigue test for SBR0.

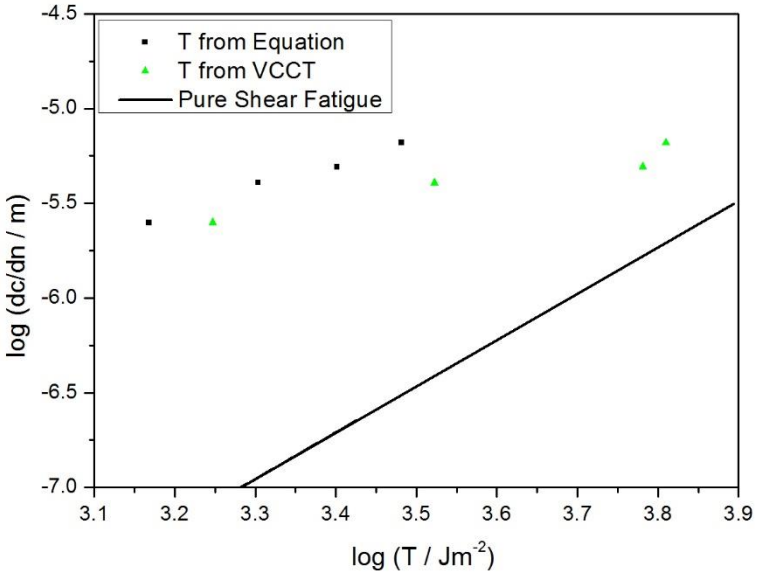

Figure 5-20. The correlation of the tearing energy derived from VCCT, Equation 4-12, and pure shear fatigue test for NR0.

5.5 Summary and Conclusions

The tearing energy during the blade abrasion was estimated using FEA techniques. The geometry of the abrasion asperity, material property, boundary conditions, and contact

conditions were carefully modelled in order to simulate the real abrasion behaviour. For the first time a VCCT was applied to calculate the tearing energy during abrasion. The predicted tearing energy gives a better correlation to the pure shear fatigue test for unfilled SBR material, which indicates that the dominant abrasion mechanism for blade abrasion at steady state is fatigue abrasion. For NR material, the stain induced crystallisation reinforces the fatigue crack growth resistance for the pure shear fatigue test, whilst it is possible that during abrasion the processes are too fast to allow strain induced crystallisation to fully develop due to the rapid deformation during the abrasion. As a consequence the correlation is less good. VCCT provides an alternative way to calculate the tearing energy for rubber fracture in FEA simulation, since it only considers the local force and displacement at the crack tip. It is a much simpler, more reliable, and a faster approach than other methods such as energy balance as it required only a single model to be used to calculate the tearing energy value.

6 Chapter Six: Rubber Wear Mechanisms on Sharp Abrasive Surface

6.1 Introduction

So far in this thesis fatigue wear has been investigated using the blade abrasion apparatus and the tearing energy at an individual asperity has been examined using a FEA modelling technique. In real wear applications such as is encountered during tyre wear on a road surface, the irregular topology of the road surface typically leads to a series of irregularly shaped and potentially jagged points of contact with the tyre's rubber surface. In this chapter, rubber abrasion against a sharp counter surface is explored. Normally, the abrasion of a series of sharp and hard asperities during sliding contact is a very severe testing configuration, potentially even more demanding than that encountered during blade abrasion. As is discussed in chapter 3, abrasive wear is the dominant abrasion mechanism under these conditions. Under the most extreme conditions the failure is a result of local stress concentrations exceeding the fundamental strength of the rubber. In this case, rubber abrasion is similar to the abrasion of higher modulus materials such as plastics and metals. For these types of materials there is extensive micro-cutting and longitudinal scratches formed on the abraded rubber surface. The formation of a master curve for this type of abrasive wear at different velocities and over a range of testing temperatures essentially demonstrates that this form of abrasive wear is essentially a viscoelastic process (Grosch and Schallamach, 1966).

However, only relatively low velocities, below 3 cm/s, have been reported previously as there is a significant issue at higher rates resulting from a significant temperature rise on the surface as a consequence of hysteretic energy dissipation. As a part of this investigation a bespoke surface contact abrasion machine was designed and built to investigate the rate of rubber abrasion potentially against any of a wide range of surfaces. In this chapter, the wear of the rubber against silicon carbide sandpaper under both dry and wet conditions is reported. The effect of much greater sliding velocities that could range from 20 cm/s to 200 cm/s was investigated. Since the heat raised during

this high velocity abrasion test has to be taken account, an infrared (IR) camera was used to record the rubber surface temperature. The aim of this chapter is to understand the effect on rubber abrasion of a high sliding velocity and the resulting higher rubber surface temperature for both lubricated and non-lubricated wear conditions.

6.2 Experiment

6.2.1 Materials

Since the test severity was greater than that encountered during the blade abrasion, only five filled rubber materials that are shown in Table 4-1 were used. The five compounds were cured into the same size rubber wheels using the same moulding conditions that are described in Chapter 4.

6.2.2 Surface Contact Abrasion

Figure 6-1 shows the schematic diagram and the apparatus of the surface contact abrasion. The rubber wheel was driven by a servo-motor. The rotation speed of the motor was adjustable from 60 rpm to 600 rpm, which corresponded to the sliding velocity from 20 cm/s to 200 cm/s. Rubber wheels were rotated against a flat platform on which there was a silicon carbide sandpaper of 400 grit. The 400 grit size sandpaper has an average particle diameter of 0.023 mm, which is much sharper than the blade used for blade abrasion which has a blade tip radius of 0.3 mm. The platform was positioned more slowly by another motor, which allowed it to move at between 0.1 cm/s to 1 cm/s in order to continuously provide a fresh contact surface during the test. The ratio of the rubber rotating velocity to the platform moving velocity was kept to the same (100) to maintain an equivalent relative velocity. A geometry torque sensor was used to record the moment imposed on the wheel and by knowing the normal force and the test specimen geometry it was possible to calculate the frictional force.

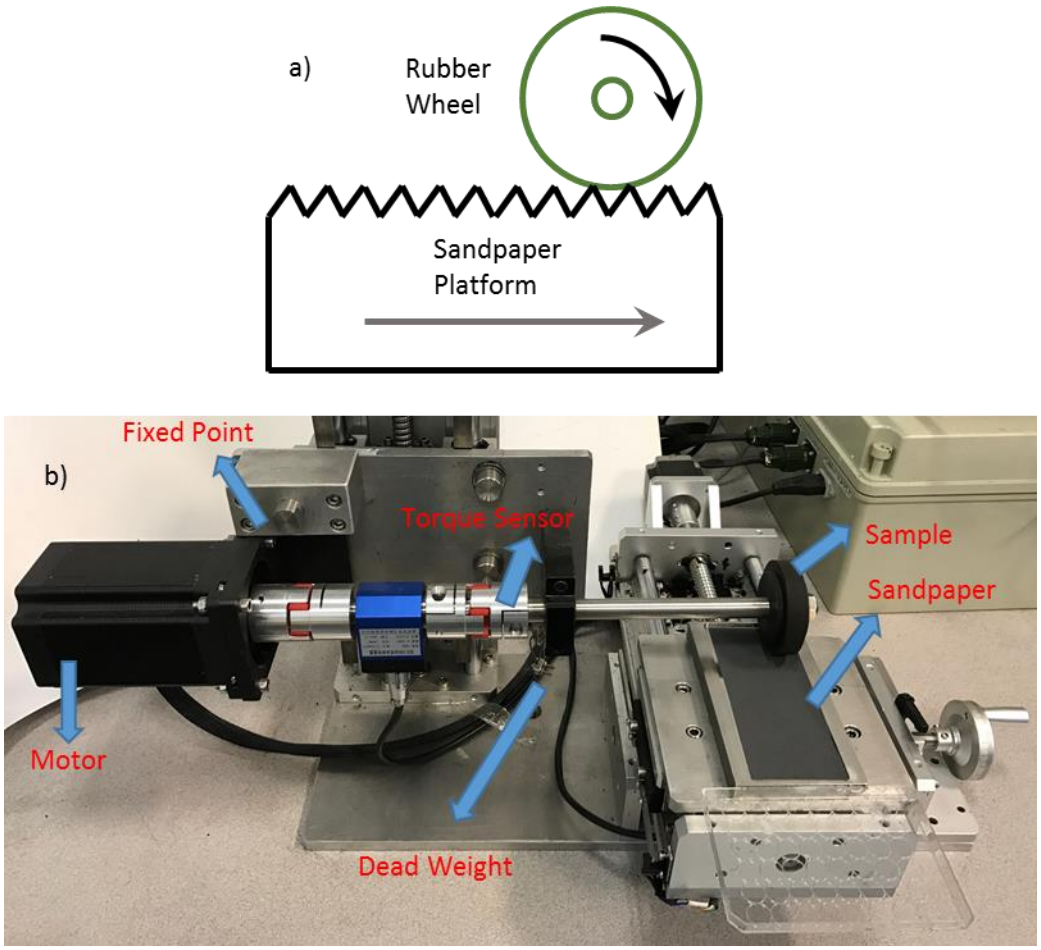

Figure 6-1. a) Schematic diagram and b) apparatus of surface contact abrasion test rig.

The main shaft was fixed at one end and a dead weight of 5 kg was applied in between the fixed point and rubber wheels to apply constant normal force approximately 35 N. The contact area was calculated by dying the surface of the sample wheel and measuring the dimension of the inked rectangular area of the counter face, which was approximately 12.5 mm in width and 14 mm in length. Therefore, the corresponding contact pressure was approximately 0.2 MPa. For each test undertaken, the test specimens were abraded from one end of the sandpaper to the other end as the platform moved, which was roughly 120 revolutions. Then rubber wheels were carefully weighed to measure their mass (and hence mass loss rate) using an electronic analytical balance with 0.1 mg tolerance. Before each new test the used sandpaper was removed and a new one was replaced on the substrate in order to minimise the effect of wear debris on the contact area. This was repeated for at least 8 cycles in order to ensure that the measured abrasion rate was stable for each sample. For wet conditions, deionised

water at room temperature was added onto the platform. An infrared camera (FLIR A35) was used to measure the rubber surface temperature during this investigation. The temperature rise at nine points along the surface of the rubber was recorded.

6.3 Results and Discussion

6.3.1 Define the Abrasion Loss

Figure 6-2 shows the total mass loss as a function of number of revolutions for all five materials, when the sliding velocity is 20 cm/s and platform's moving velocity is 2 mm/s. There is a good linear relationship for all the materials except SBR80SI. For SBR80SI, at the beginning the weight loss was large. Then it significantly reduced when the abrasion extended beyond 500 revolutions. The slope of the steady state regime after more than 500 cycles was presumed to be the measured abrasion rate. The R square value was always greater than 0.99. One obvious comment regarding the testing as shown in Figure 6-2 is that the rates from one compound to another are quite significantly different. This is clear when considering the scale of the y-axis being nearly two orders of magnitude between the fastest worn rubber compound and the slowest. Thus, the abrasion rate can vary more than one order magnitude for the test conditions depending on different compounds.

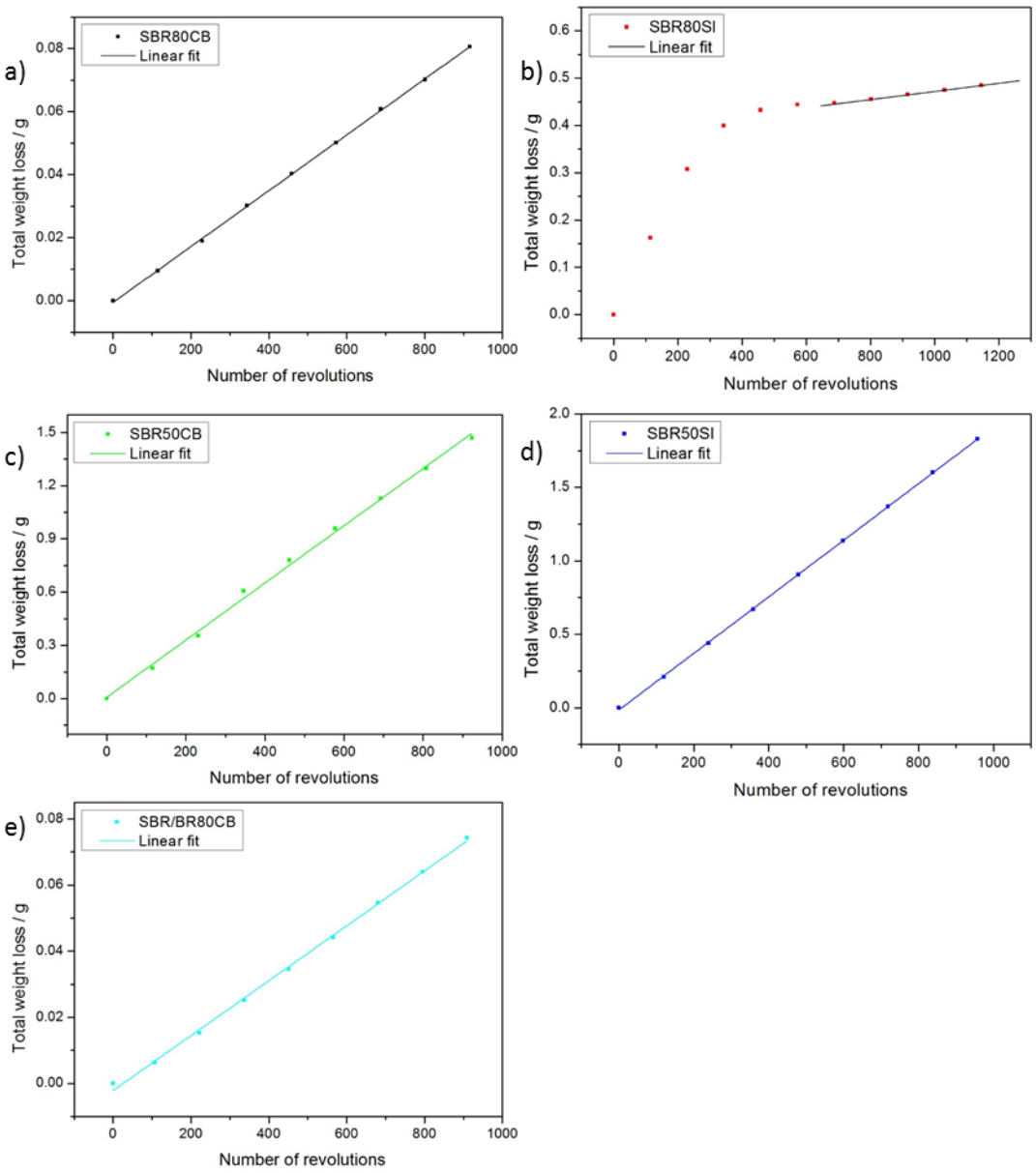

Figure 6-2. The total mass weight loss as a function of number of revolutions when the rubber sliding velocity was 20 cm/s and the platform sliding velocity was 2 mm/s; a) SBR80CB, b) SBR80SI, c) SBR50CB, d) SBR50CB, and e) SBR/BR80CB.

6.3.2 Wear Debris and Abraded Surface

Figure 6-3 shows the wear debris deposited on the sandpaper after 120 cycles before it was replaced with a fresh one. The abraded debris has two distinct morphologies. For materials with a rapid rate of abrasion as was the case with the wheels made from SBR50CB or SBR50SI, the debris was large and dry. The wear debris has a particular structure and morphology is shown Figure 6-3 a). However, the debris formed with

materials with a much lower rate of abrasion loss such as SBR80CB was oily and stuck to the surface of sandpaper as is shown in Figure 6-3 b), which indicated that a completely different type of abrasion mechanisms had occurred.

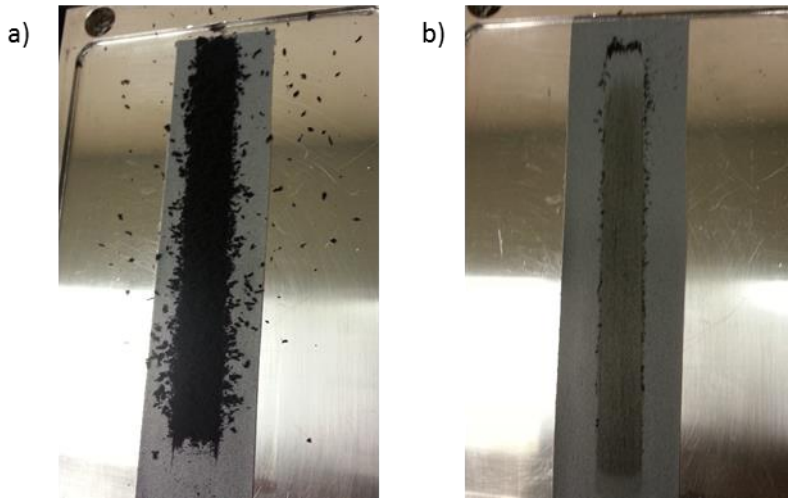

Figure 6-3. The abraded debris at 20 cm/s for a) SBR50SI and b) SBR80CB.

The SEM images of the abraded surface also highlight the differences between the two abrasion mechanisms as shown in Figure 6-4. The abraded surface for SBR80SI at the beginning of the abrasion tests displayed ploughed lines parallel to the sliding direction. However, as the abrasion process was allowed to develop using the same compound after about 500 revolutions the scratched rubber surface became more like the liquid type of surface. Although the parallel lines from the initial rapid abrasion remain, there depth of the scratches are reduced and the surface becomes much smoother. The small particles on the surface are either grit from the sandpaper or reincorporated wear particles.

Similar to the blade abrasion described in earlier chapters, it is clear that two abrasion mechanisms operate under different testing conditions when using this type of sharp contact abrasion. Despite the relatively severe contact conditions, for some rubber compounds abrasion due to polymer degradation develops a sticky debris. The abrasion mechanism in this case is the smearing wear as discussed earlier. The degraded sticky debris deposited on the surface of both the sandpaper and the rubber wheel as a transfer layer. This transfer layer changes the original contact conditions and produces

a low rate of abrasion loss. Abrasion due to a cutting type of mechanical failure generates conventional debris. The debris is dry and results in the formation of large particulates. The score lines on the rubber surface indicates that an abrasive wear mechanism dominates the abrasion behaviour in this case.

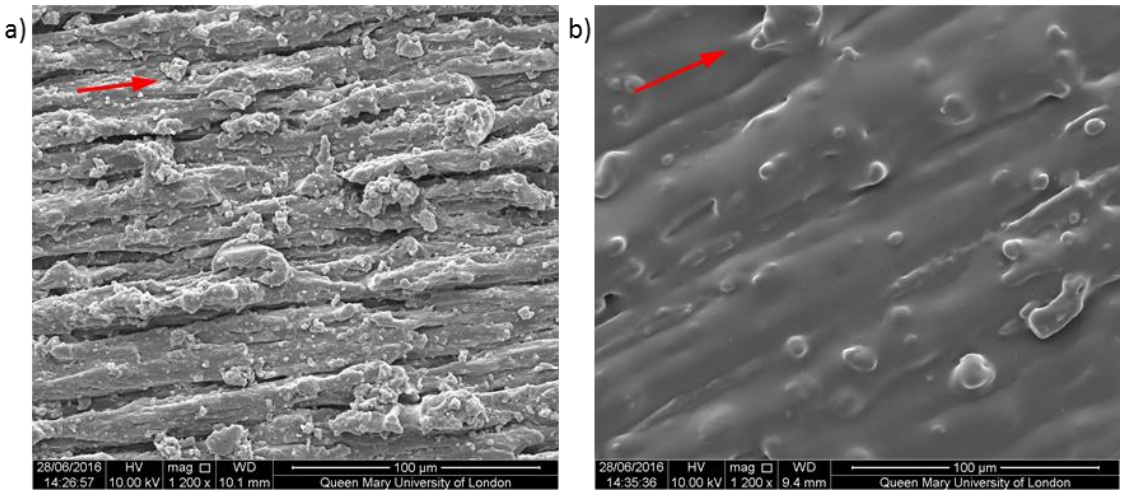

Figure 6-4. SEM images of abraded rubber surface for SBR80SI: a) at 200 cycles and b) at 800 cm/s. (red arrow indicating the sliding direction)

6.3.3 Effect of Sliding Velocity on the Abrasion Behaviour

The abrasion rates as a function of the relative sliding velocity for the five different rubber compounds are shown in Figure 6-5. There was more than one order of magnitude difference between the abrasion rates depending upon the rubber compound and the sliding velocity. For SBR80CB, SBR80SI and SBR/BR80CB, the abrasion mechanism appeared to be one of smearing wear. The sticky transfer layer that was generated was deposited on both the rubber surface and the abrasive surface, which significantly changed the original contact conditions. As the abrasive surface was covered by the transfer layer, the abrasive surface profile became less sharp. This possibly significantly decreased the test severity which resulted in a reduced abrasion rate. However, for the other two compounds SBR50CB and SBR50SI, the rate of abrasion loss was much greater at a low sliding velocity, as abrasive wear processes were the dominant abrasion mechanism in this regime. At faster sliding rates above 100 cm/s, then there was a significant decrease in the rate of abrasion for these materials. In particular for SBR50CB there was a transition in the wear mechanism and at the fastest

rates it exhibited the lowest abrasion rates, lower than SBR80CB, SBR80SI and SBR/BR80CB at a sliding velocity of 180 cm/s. The reduction of the abrasion rate for SBR50SI with sliding velocity was less significant. The dramatic reduction of the rate of abrasion is a result of a change in the abrasion mechanism to smearing wear at these high velocity.

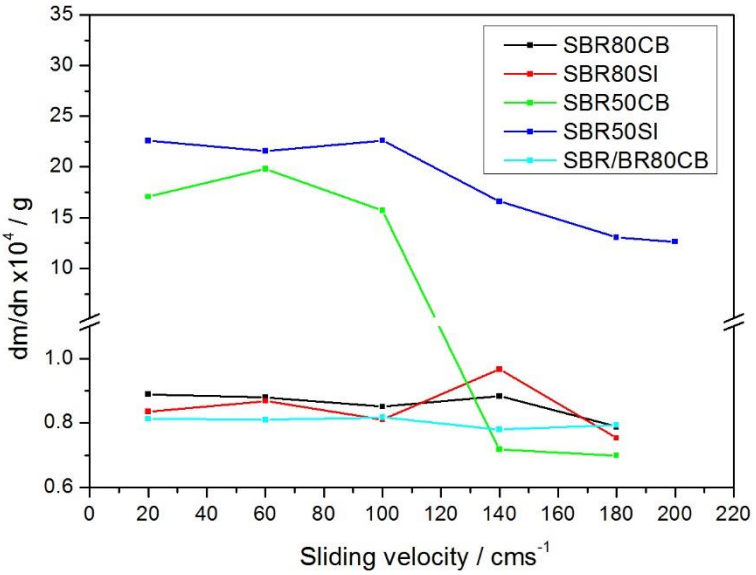

Figure 6-5. Abrasion rate as a function of sliding velocity for dry contact conditions.

It was plausible that the changing of the abrasion mechanism with the sliding velocity might be due to a change in the contact surface temperature. Although it is difficult to directly measure the local contact temperature at the point or time of contact, an Infra Red (IR) camera is used to record the free surface temperature of rubber compounds during abrasion. Figure 6-6 shows the instant surface temperature profile of SBR80CB at 20 cm/s velocity at 20 cycles. The slightly uneven distribution is probably due to the small asymmetry of contact of the wheel. Figure 6-7 gives the surface temperature against revolution cycles for SBR80SI at sliding speed of 100 cm/s as an example. The rubber surface temperature increased from room temperature up to around 120 °C before the first mass measurement. Then the test was stopped at 100 cycles in order to measure the weight loss. The test was continued in this stepwise fashion until 800 cycles.

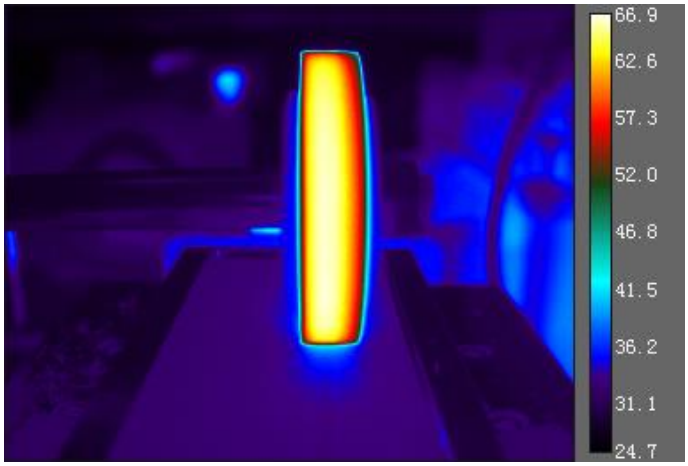

Figure 6-6. The instant IR camera image of SBR80CB at 20 cm/s.

The whole temperature profile as shown in Figure 6-7 was averaged as the average surface temperature during the test. The abrasion loss data shown in Figure 6-5 is replotted against to the average surface temperature as shown in Figure 6-8. For the smearing wear as presented by SBR80CB, SBR80SI and SBR/BR80CB, the surface temperature had little effect on the rate of abrasion. The surface temperature increased with the sliding velocity, up until an average surface temperature of around 120°C was reached. Of course the temperature in the actual contact region of the interface could be much higher and this temperature is clearly sufficient to cause the thermal degradation of the rubber. As a result, for the rest two rubber compounds the dominant wear mechanisms changed from abrasive wear to smearing wear as the temperature increased.

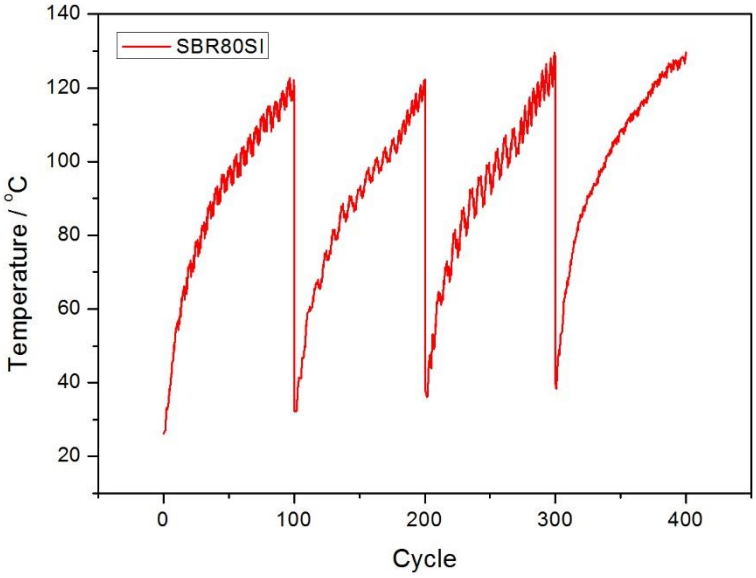

Figure 6-7. The raised surface temperature of SBR80CB at 100 cm/s.

By comparing the results for SBR80CB and SBR80SI, it appears that carbon black filled rubber is more likely to produce smearing wear than silica filled rubber, since SBR80CB exhibits smearing wear immediately when the abrasion starts and SBR80SI shows abrasive wear initially which slowly develops into a sticky surface as shown in Figure 6-2. It is the same conditions for SBR50CB and SBR50SI, as SBR50CB transforms to smearing wear at much lower surface temperature than SBR50SI as shown in Figure 6-8. Although the exact reason is not yet clear, it might be because the silica filled rubber compounds are stiffer than the carbon black shown in Figure 4-5 due to their smaller particles in the compound. This might help promote the abrasive wear behaviour just like abrasion of hard materials such metal and plastic. Conversely, the SBR/BR80CB blend tended to become sticky potentially owing to its reduced stiffness.

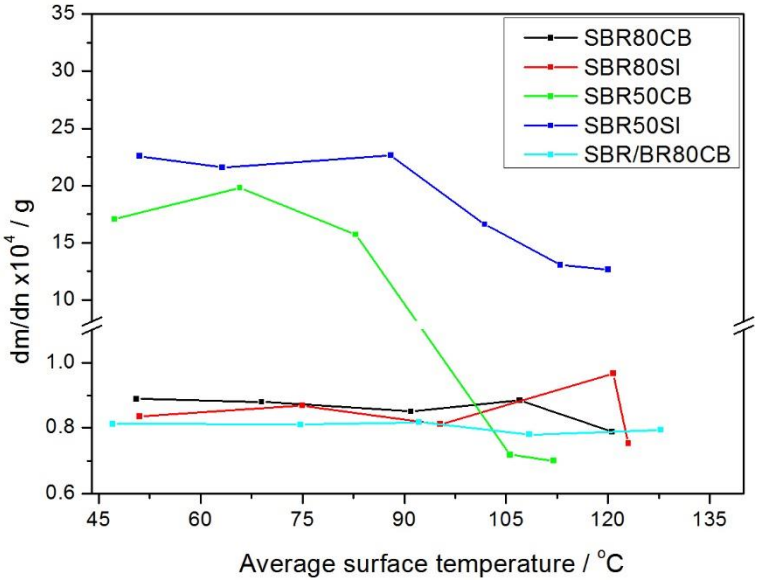

Figure 6-8. Abrasion rate as a function of the average surface temperature.

The polymer used in the SBR80CB, SBR80SI and SBR/BR80CB compounds are, similarly to a number of tyre tread compounds, made from are oil-extended SBR with 37.5 phr process oil to facilitate the mixing process. For 50 phr filler loading compounds, SBR50CB and SBR50SI, there was no process oil incorporated and they are stiffer than their more highly loaded equivalents SBR80CB and SBR80SI accordingly. Therefore, the presence of the process oil definitely promotes the smearing wear. In addition, the large strains and the high temperatures at the rubber surface during the abrasion test increase the rate of diffusion of any low molecular weight ingredients such as oils and wax because of their surface blooming effect (Nah and Thomas, 1981).

6.3.4 Effect of Water Lubricant on the Abrasion Behaviour

The abrasion rate as a function of sliding velocity under wet conditions is shown in Figure 6-9. For all five compounds, only abrasive wear behaviour was observed for wet conditions. No smearing wear was present. Therefore, all the abrasion rates for wet conditions were relatively high due to the absence of the transfer-layer to transfer-layer contact. Silica filled rubber compounds had a greater weight loss than carbon black filled rubbers possible due to the higher friction force of silica filled rubbers under these wet conditions, which is discussed in section 6.3.5. The abrasion rate seemed to increase

with the sliding velocity up to 140 cm/s. This is probably because as the rotation speed increases, then the abraded debris is more easily thrown out away from the wheel due to the larger centrifugal force which means that it is not available to help form a protective layer on the rubber surface to prevent it from being further abraded. The slight decrease of the weight loss at 180 cm/s could be due to the formation of a more effective boundary water film layer at the interface.

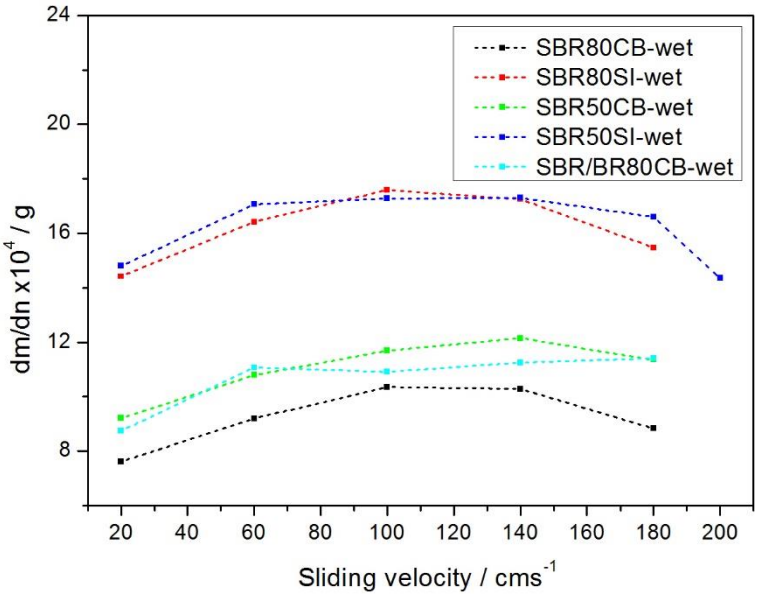

Figure 6-9. The abrasion rate as a function of sliding velocity under wet conditions.

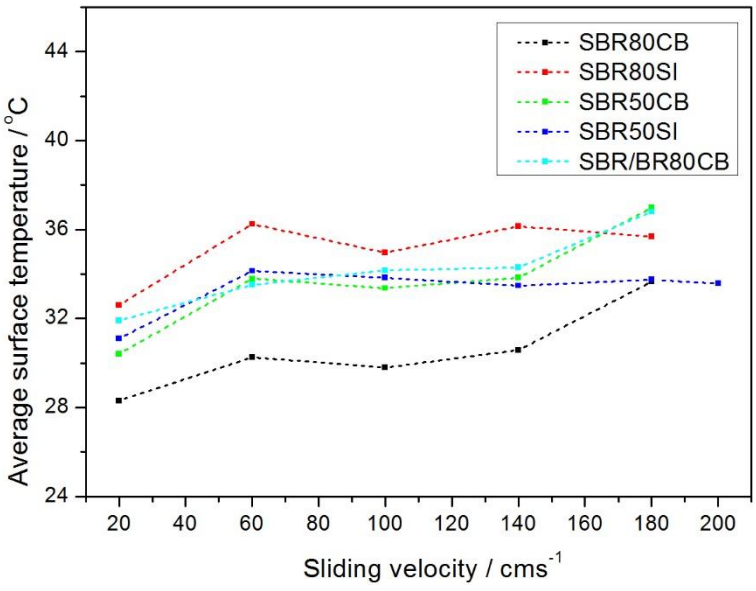

Figure 6-10. The average surface temperature as a function of sliding velocity under wet conditions.

The average surface temperature is plotted against the sliding velocity under wet conditions as shown in Figure 6-10. Under water lubricated conditions, the surface temperature is much lower than that for dry contact conditions and it is less dependent upon the sliding velocity. The increase in temperature was less than 15 °C above the room temperature. It is assumed that the presence of water also significantly reduces the amount and the temperature of any hot spots that might form at the interface between the rubber and the sandpaper. Therefore, no smearing wear initiates under water lubricated condition even at the highest velocities.

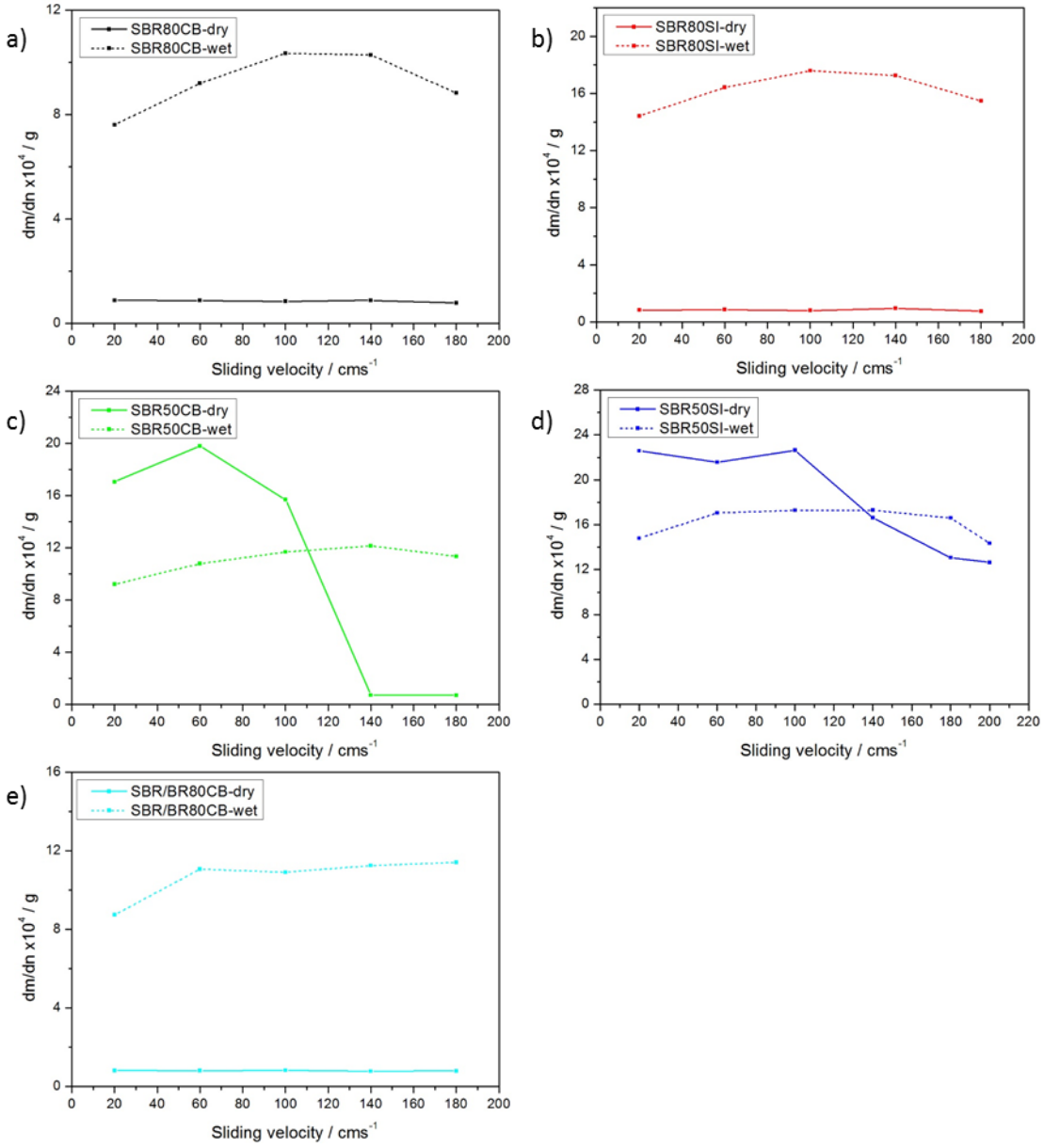

Figure 6-11. The comparison of abrasion rate under dry and wet contact conditions.

The abrasion rates for both dry and wet conditions are plotted together for the comparison as shown in Figure 6-11. It is interesting and immediately apparent that water based lubrication does not always reduce the rate of abrasion loss. As a consequence of the lubrication the abrasion mechanisms for SBR80CB, SBR50SI, and SBR/BR80CB changed from smearing wear to an abrasive wear mechanism when adding water at the interface. As a consequence, the abrasion loss for wet conditions was under a wide range of conditions much greater than that for dry conditions. For SBR50CB, and SBR50SI, the water lowered the abrasion rate when the sliding velocity was low. Up to 100 cm/s the dominant abrasion mechanism was primarily one of abrasive wear. The water acted as a limited lubricant, if the wear behaviour remained the same. At high velocity, since the smearing wear started to govern the abrasion behaviour under dry conditions. The abrasion rate for wet conditions became higher.

6.3.5 Friction Behaviour

The friction force for both dry and wet contact conditions during the various tests are shown in Figure 6-12. The friction force under dry conditions decreased with increasing the sliding velocity. The friction under these conditions depends upon the viscoelastic behaviour of the rubber which makes it both frequency and temperature dependent. As the velocity increased from 20 cm/s to 200 cm/s, the average contact surface temperature raised over 70°C as shown in Figure 6-8. As a result it moves further away from the glass transition temperature and hence it results in lower friction. Under wet conditions, the friction force was less dependent on the sliding velocity since the contact surface temperature was much more stable as shown in Figure 6-10. The friction force was mainly influenced by the frequency. As a consequence, there was a slight increase of the friction along with the sliding velocity under wet conditions. Adding water into the contact surface as a lubricant reduced the friction force. However, this effect was more significant, when the sliding velocity was low due to lower temperature generated at the rubber face. At high sliding velocity, the lubrication effect was less effective in this testing since the friction for the dry conditions are significantly lower at high sliding velocity.

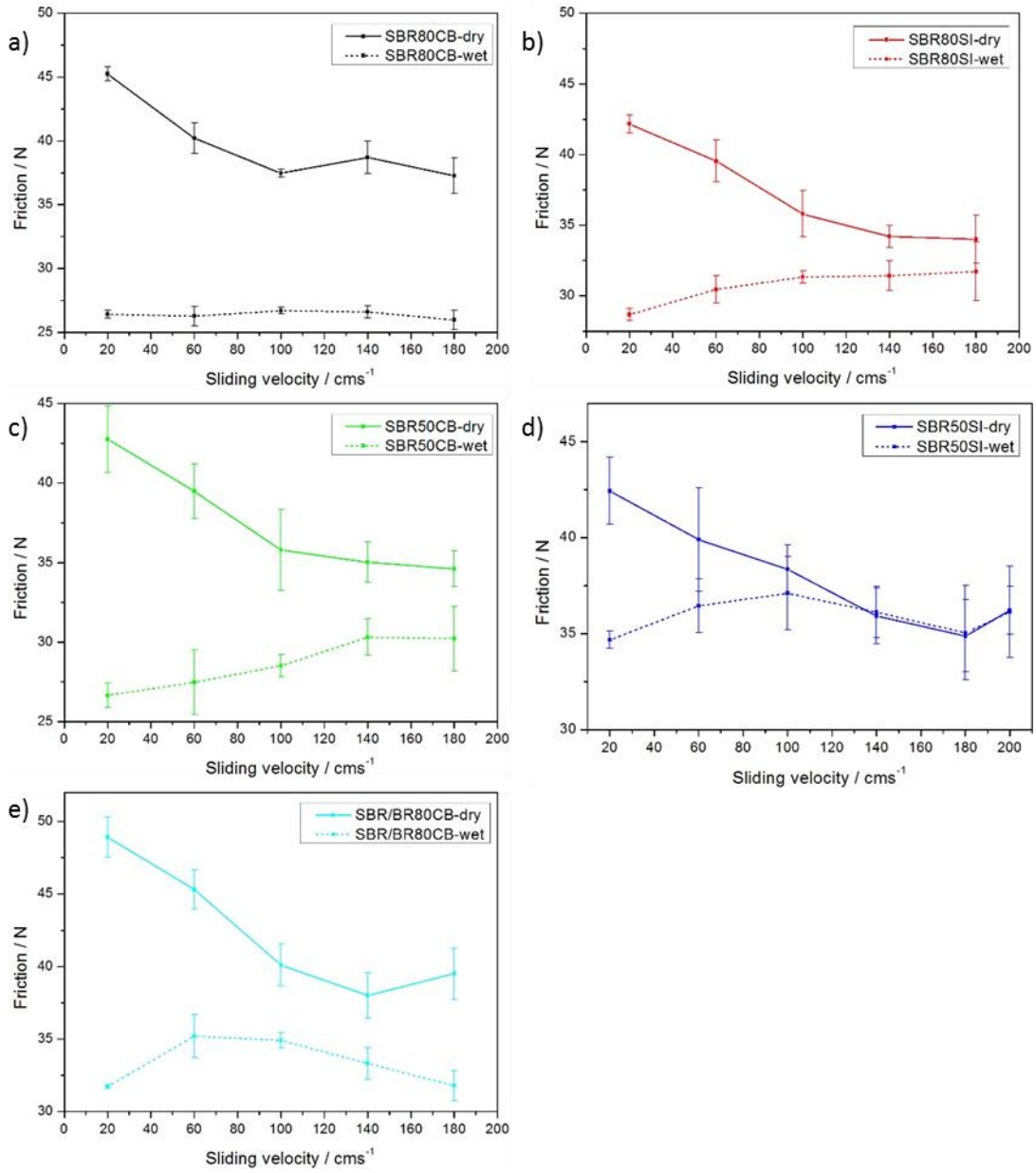

Figure 6-12. Friction force as a function of sliding velocity under both wet and dry conditions.

6.4 Summary and Conclusion

Rubber abrasion on sharp contact conditions was carried out by rotating rubber wheels on silicon carbide sandpaper at various velocities for both dry and wet contact conditions. Two abrasion mechanisms, abrasive wear and smearing wear, can be presented depending on the rubber compounds, contact temperature and contact conditions. Thus, the measured abrasion rate can have a wide range in excess of an order magnitude.

The high velocities encountered during testing can lead to significant temperature rise at the interface under dry conditions. Thus, the high velocity promotes the smearing wear due to mechano-chemical degradation processes. In contrast, the low velocity generates less heat, so that the abrasive wear is easier to develop.

The presence of water can significantly lower the temperature of the interface, which inhibits the formation of the sticky layer on the rubber surface. The abrasion mechanism can shift from smearing wear to abrasive wear by adding water. Accordingly, the abrasion rate is not always reduced for wet conditions. For abrasive wear, water acts as a lubricant to reduce the abrasion losses that arise due to a lower frictional force.

The process oil in the rubber compounds can stimulates the smearing wear due to two effects. Firstly, it reduces the modulus of the rubber. Next any low molecular weight oils or waxes within the rubber can migrate to the rubber surface as a result of blooming effect. Both processes benefit the formation of smearing wear. It seems that carbon black compounds are easier to develop smearing wear than silica compounds. That could be because of the lower stiffness and reduced filler-polymer interaction of carbon black compounds. SBR and BR blend tends to generate smearing wear owing to the low stiffness as well.

7 Chapter Seven: Characterisation of the Transfer Layer Formed during the Smearing Wear

7.1 Introduction

Both the fatigue wear and abrasive wear result from types of mechanical failure in the rubber. For smearing wear, it is clear that a chemical degradation of the rubber controls the abrasion behaviour. This degradation is significantly affected by the local temperature generated during frictional sliding, the oxidative deterioration of the rubber, or the rupture of rubber molecules by the large frictional forces (Gent and Pulford, 1983). Smearing wear occurs for both a blunt contact abrasion test (such as blade abrasion) and a sharp contact test (such as the abrasion of rubber against sandpaper). In practice, it is quite common for this type of abrasion to take place during a range of less severe abrasion tests, especially for tyre tread compounds. Although the exact failure mechanism is not yet clear, there is no doubt that the smearing results from the decomposition of the rubber. Most studies in the literature try to avoid the formation of the sticky layer, since they claim that the sticky layer (Grosch and Schallamach, 1966) produce more erratic measurements for the weight loss during the abrasion test. In fact some tests go out of their way to try and dry the surface using drying agents such as Fuller's earth (attapulgite) to simplify the testing (Schallamach, 1968a).

However, there has been only very limited systematic studies undertaken on the characterisation of this layer. So the fundamental questions remain. What is the actual sticky layer? How does it affect the abrasion and friction behaviour? The work described in this chapter attempts to address these questions. Various techniques were used to characterise the sticky debris with respect to its chemical content, molecular weight, and glass transition temperature. The sticky debris present on the abraded rubber surface has liquid like morphology, which implies an uncrosslinked network with a low molecular weight. The molecular weight of the sticky debris was measured using Gel Permeation Chromatography (GPC). The chemical content of the sticky debris was investigated by Thermogravimetric Analysis (TGA) and Energy-dispersive X-ray

spectroscopy (EDX). A change in the solubility of the sticky debris for the filled rubber in a solvent was observed and the insoluble rubber was measured using the standard method to measure bound rubber. Finally, the effect of the sticky debris on the abrasion and friction properties is discussed.

7.2 Experiment

7.2.1 Materials

All the five filled tread compounds plus NR0 shown in Table 4-1 were used, since all of them generated a sticky layer during blade abrasion. The sticky debris formed on the sample surface during abrasion was pushed to the side of the sample by the abrasion blade as shown in Figure 7-1. Then the sticky debris as shown in Figure 7-2 was carefully collected after a known number of abrasion cycles.

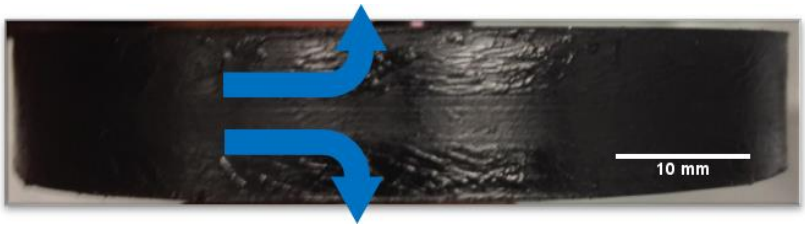

Figure 7-1. Sticky debris being pushed to the side of the sample by the blade.

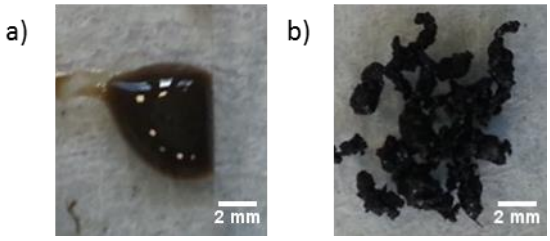

Figure 7-2. The sticky debris of a) NR0 and b) SBR80CB.

7.2.2 Gel Permeation Chromatography (GPC)

The molecular weight of the sticky debris and rubber melts was determined using GPC. The sticky debris and rubber melt were dissolved in Tetrahydrofuran (THF) with 2% Triethylamine (TEA) immediately after abrasion. A filter with 0.1µm pore size was used to filter the solution. After filtration all the filler particles were removed from the

solution. These transparent solutions were used to conduct the GPC on an Agilent 1260 infinity system equipped with Refractive Index Detector (RID) and variable wavelength detector, 2 PLgel 5 µm mixed-C columns (300×7.5mm), a PLgel 5 mm guard column (50x7.5mm) and an autosampler. The columns and the RID were operated at 40 °C. The instrument was calibrated with linear narrow poly(methyl methacrylate) standards in range of 550 to 2136000 g/mol.

7.2.3 Differential Scanning Calorimetry (DSC)

DSC was conducted to measure the glass transition temperature for both sticky debris and unabraded bulk materials. Calorimetry measurements were made using a TA Q2000. Samples of between 5 mg to 10 mg were placed in aluminium crucibles for testing. Samples were cooled to -80 °C and heated up to 20 °C under a flushing nitrogen atmosphere at a rate of 2 °C/min.

7.2.4 Thermogravimetric Analysis (TGA)

TGA performed on TA Q500 was used to characterise the chemical content, thermal stability and amount of degraded rubber of the sticky debris. Both air and nitrogen atmosphere were used. Initially the samples were heated up to 700 °C at 20 °C/min in a nitrogen atmosphere. Following this the atmosphere was changed to air and the temperature was increased from 700 °C to 1000 °C at 50 °C/min. An alternative test was also used on a different sample using an air atmosphere throughout whereby the samples were heated from room temperature to 1000°C at 20 °C/min.

7.2.5 Energy-dispersive X-ray Spectroscopy (EDX)

The SEM-EDX analyses were performed on an FEI Inspect Scanning Electron Microscope (SEM) equipped with an EDX-detector. For NR0, the specimen was coated with carbon to make it conductive. The filled materials, as they were above the filler network percolation threshold, were conductive and no conductive coating was required. The analyses were performed at a 10 kV accelerating voltage and a beam current in the range of 1 to 3 nA for up to 60 seconds.

7.2.6 Bound Rubber Measurement

Bound rubber testing was performed on the aged sticky debris to measure how much rubber remained insoluble in the sticky debris. Test samples of around 20 mg were immersed in 20 ml toluene for 120 hours. The solvent was renewed after 48 hours. After extraction the samples were dried for 24 hours in air at room temperature and then for 24 hours in an oven at 100 °C. The percentage of the bound rubber, R_b, was then calculated according to the following equation:

$$R_b\% = \frac{m_d - m_o \times f_f}{m_o \times f_p} \qquad \text{Equation 7-1}$$

where m_d is the dry mass after extraction, m_o is the mass of the original specimen, f_f and f_p are the filler fraction and polymer fraction according to the compounds original formulation.

7.3 Results and Discussion

7.3.1 Glass Transition Temperature of the Sticky Debris

The DSC trace of sample NR0 and SBR80CB is shown in Figure 7-3. The glass transition temperature is defined as the mid-point of the change of the heat capacity. There is no significant difference in the DSC trace between the bulk material and sticky debris. The glass transition temperature is similar in the bulk behaviour and also for the debris as well at approximately -61 °C for NR0 and -30 °C for SBR80CB.

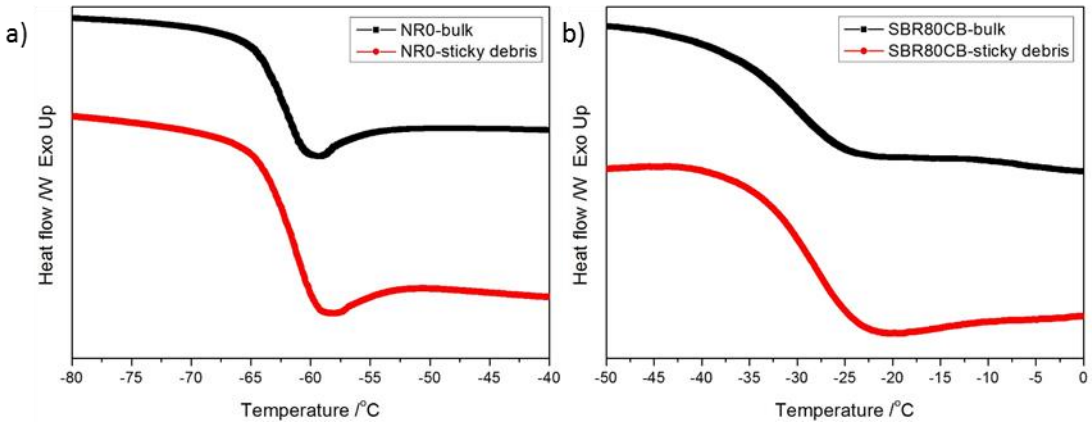

Figure 7-3. DSC trace of the sticky debris and bulk materials for a) NR0 and b) SBR80CB (exotherm up).

7.3.2 Chemical Content and Thermal Stability of the Sticky Debris

Figure 7-4 shows the TGA weight loss curves in nitrogen until 700 °C and in air from 700 °C to 1000 °C for NR0 and SBR/BR80CB. All the volatile content and the polymer content were degraded in nitrogen up to 500 °C. Then the remaining carbon based fillers were further burnt out in the air above 700 °C. The TGA curve of the sticky debris performed in this way is very similar to that of bulk material. The sticky debris consisted of the same amount of filler as the bulk material. However, the thermal stability of the sticky debris was inferior, since it decomposed at a faster rate in the nitrogen atmosphere. This probably results from a lower molecular weight of the sticky debris, since it is known that an increase in molecular weight increases thermal stability (Hacaloglu et al., 1997). The molecular weight of the sticky layer is shown section 7.3.3.

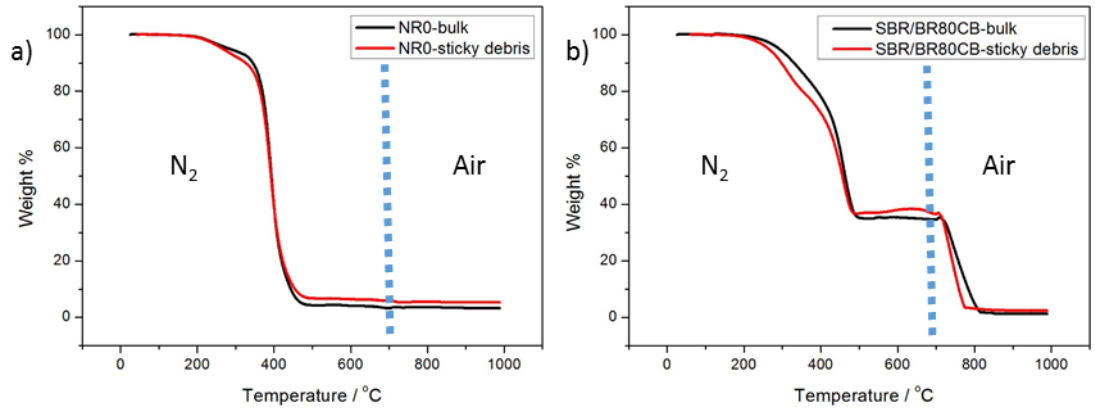

Figure 7-4. TGA weight loss in nitrogen up to 700°C and in air from 700 °C to 1000 °C of a) NR0 and b) SBR/BR80CB.

TGA was also performed in air atmosphere over the entire temperature range. The results are shown in Figure 7-5. Under thermo-oxidative conditions, there were three steps clearly identified for the rubber decomposition. For NR0 the volatile low molecular weight materials degraded first below 320 °C. Following this, the polymer itself started to degrade. The last step was the degradation process of the char formed during the second step. For SBR/BR80CB, the volatiles degraded first below 420 °C. Then the polymer decomposed below 500 °C. Finally, the carbon black filler and the char formed by polymer degradation during second step degraded at the highest temperature (Bourbigot et al., 2004).

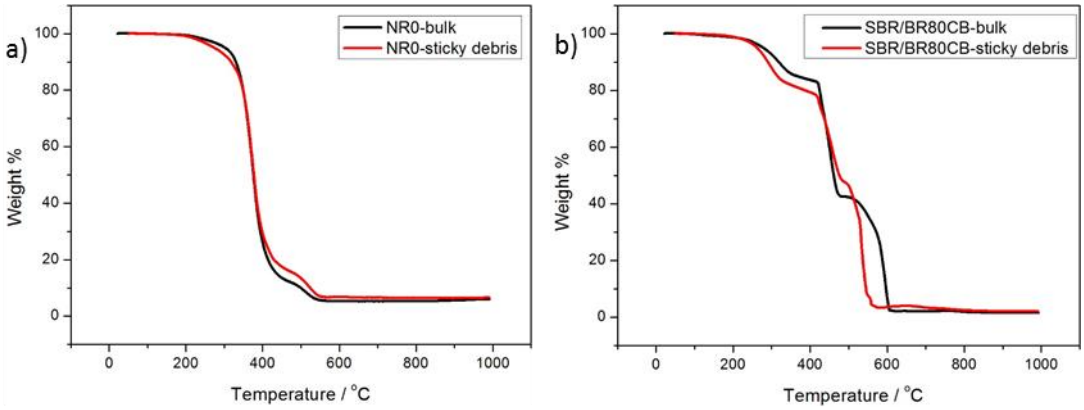

Figure 7-5. TGA weight loss in air of a) NR0 and b) SBR/BR80CB.

Table 7-1. Weight percent loss of thermal-oxidative degradation for NR0 material.

	Volatile (320°C)	Rubber Chains (450°C)	Char (600°C)	Inorganic Ash (1000°C)
NR0-bulk	8.13%	78.21%	8.21%	5.45%
NR-sticky debris	11.12%	71.14%	10.74%	7.00%

Compared with the bulk material, the sticky debris contained a greater volatile content and a lower rubber content. There is a greater charring effect for the sticky debris being degraded in the air. The blooming effect during abrasion is one possible reason for the greater volatile content. In addition, the rubber degradation due to the smearing wear could also break down the high molecular weight materials into lower molecular weight components. The lower rubber content in the sticky debris indicates that the

degradation of rubber molecules during the smearing wear, is at least part of the problem. The greater char probably results from more hydroperoxides forming during the degradation of the sticky debris (Bourbigot et al., 2004), which is possibly formed via thermal oxidation. The weight percentage loss of each step for thermal oxidative degradation is shown in Table 7-1 for NR0 and in Table 7-2 for the filled materials.

Table 7-2. Weight percent loss of thermal-oxidative degradation for filled materials.

	Volatile (420°C)	Rubber Chains (500°C)	Carbon Black and Char (800°C)	Inorganic Ash (1000°C)
SBR80CB-bulk	15.98%	41.58%	40.11%	2.33%
SBR80CB-sticky debris	18.50%	37.84%	42.14%	1.51%
SBR80SI-bulk	15.11%	43.21%	9.35%	32.17%
SBR80SI-sticky debris	19.81%	32.55%	16.06%	31.58%
SBR50CB-bulk	8.75%	52.12%	37.77%	1.36%
SBR50CB-sticky debris	10.23%	45.02%	41.90%	2.85%
SBR50SI-bulk	9.35%	50.78%	10.94%	28.93%
SBR50SI-sticky debris	12.65%	43.91%	15.48%	27.96%
SBR/BR80CB-bulk	17.60%	40.13%	40.49%	1.68%
SBR/BR80CB-sticky debris	22.97%	30.36%	44.38%	2.29%

A simple elemental mapping was undertaken using EDX in order to determine the sticky debris. The results are shown in Table 7-3. The sticky debris had more oxygen content compared to the bulk materials. This confirms the oxidative degradation of smearing wear. In addition, the sulphur content was lower in the sticky debris.

Table 7-3. EDX analysis of sticky debris and bulk rubbers.

	Oxygen wt%	Sulphur wt%	Zinc wt%	Carbon wt%	Silicon wt%
NR0-bulk	39.00%	26.09%	34.91%	-	-
NR0-sticky debris	41.66%	25.16%	33.18%	-	-
SBR80CB-bulk	2.00%	2.24%	1.54%	94.17%	-
SBR80CB-sticky debris	9.82%	0.67%	0.09%	89.30%	-
SBR80SI-bulk	23.88%	0.98%	0.12%	67.43%	7.61%
SBR80SI-sticky debris	28.29%	0.85%	0.23%	64.21%	6.39%
SBR50CB-bulk	2.81%	1.48%	1.66%	93.96%	-
SBR50CB-sticky debris	8.50%	0.66%	0.41%	90.38%	-
SBR50SI-bulk	16.38%	0.88%	0.22%	75.50%	6.99%
SBR50SI-sticky debris	24.74%	0.94%	0.72%	66.11%	7.45%
SBR/BR80CB-bulk	2.83%	2.00%	1.19%	93.80%	-
SBR/BR80CB-sticky debris	7.14%	1.10%	0.64%	90.75%	-

7.3.3 Molecular Weight of the Sticky Debris

As described before, the sticky debris has an oily, gooey and liquid like morphology, which implies it has a lower molecular weight. The sticky debris generated during abrasion was dissolved in THF immediately to measure the molecular weight using GPC. The measured result was compared with the original molecular weight of the uncured rubber melt extracted in THF as shown in Figure 7-6. There is no result for the NR0 melt, since the solution blocked the GPC column, which automatically stopped the test.

The GPC trace for the sticky debris shifted to the right compared to the rubber melt, which confirms that there is a longer retention time suggesting smaller molecules of rubber exist in the sticky debris. There were two peaks for the GPC traces of SBR50CB and SBR50SI melts, which was probably because of a non-uniform distribution of the molecular weight. Once being abraded, the molecular weight of the sticky debris became smaller and more uniform. The weight average molecular weight of the sticky debris was almost one order magnitude lower than that of the original rubber melts as

shown in Figure 7-7. Although there is no result for NR0, the molecular weight of normal NR is thought to be above 200,000 Da. This is far greater than that of the sticky debris. Clearly, the rubber molecules are broken into small fractions during abrasion, which results in this sticky liquid like debris being produced with this very low molecular weight.

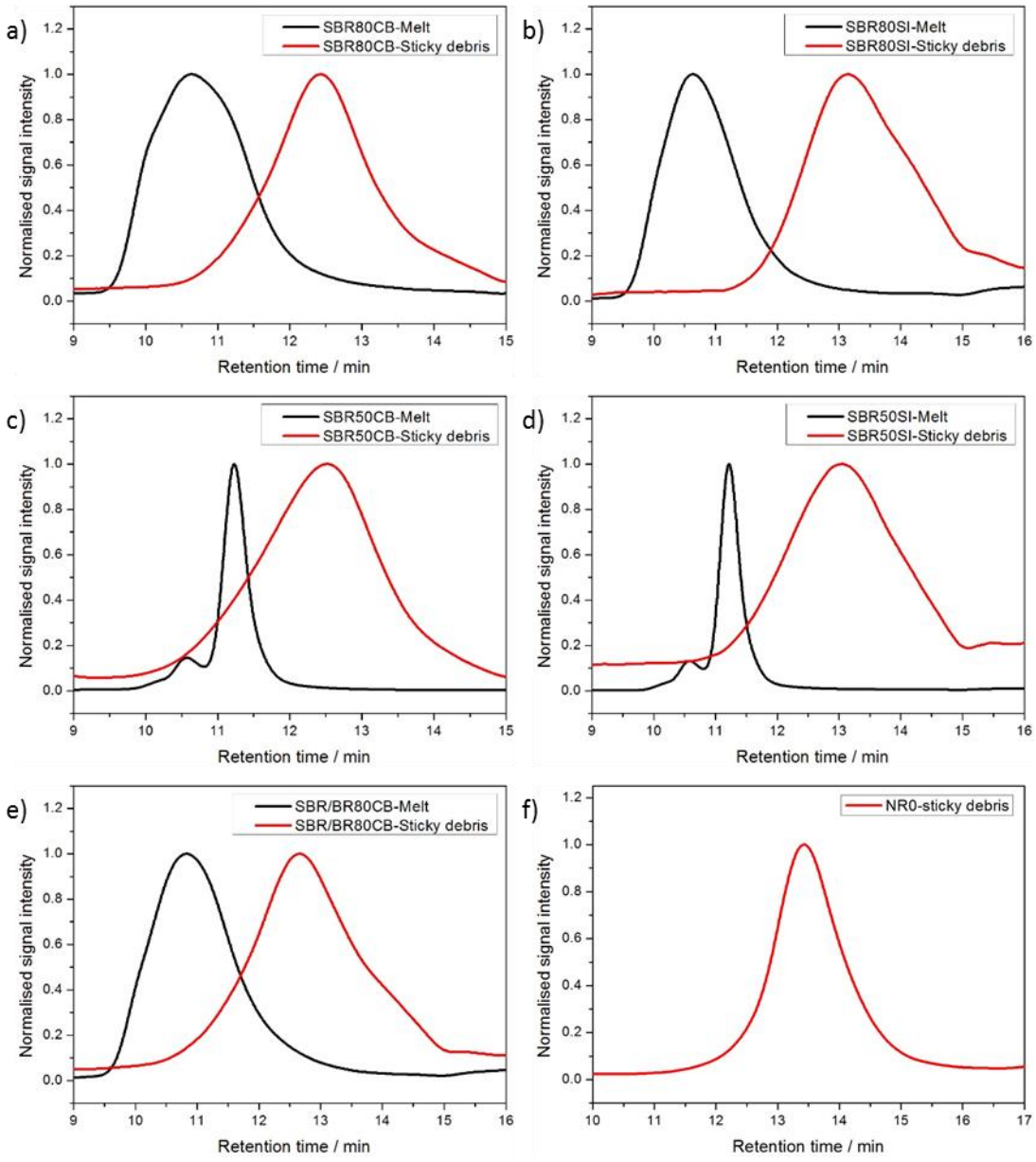

Figure 7-6. GPC trace of the rubber melt and sticky debris for a) SBR80CB, b) SBR80SI, c) SBR50CB, d) SBR50SI, e) SBR/BR80CB, and f) NR0.

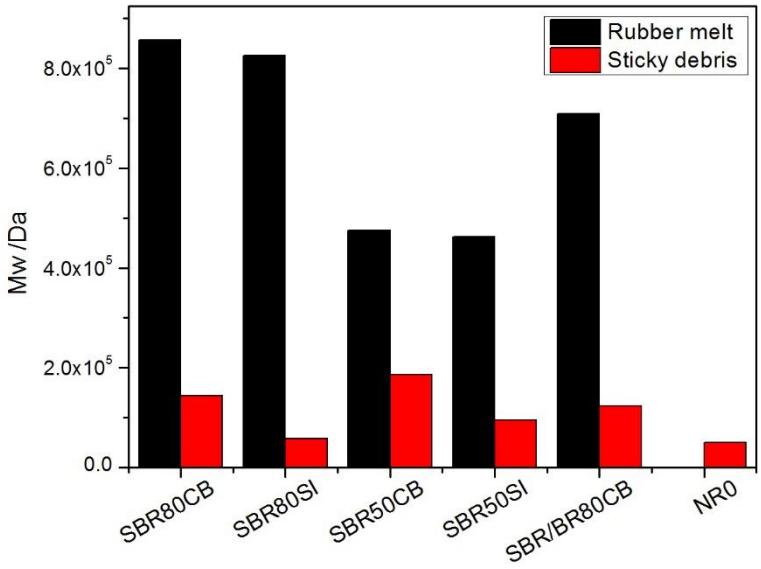

Figure 7-7. Weight average molecular weight for the uncured rubber melts and the sticky debris.

7.3.4 Fresh Sticky Debris vs Old Sticky Debris

One interesting phenomenon was observed for all of the filled rubbers, after leaving the sticky debris for a time period in excess of 24 hours. Figure 7-8 a) shows the fresh sticky debris of SBR80CB in toluene. The debris appeared to be completely soluble in the solvent. The undissolved carbon black formed a suspension, which resulted in the solution becoming completely black. Figure 7-8 b) shows the old sticky debris in the same solvent. Large insoluble debris were clearly visible at the bottom. The solution still remains transparent. It was apparent that the solubility of the sticky debris was significantly reduced with the dwell time.

It was confirmed by the GPC result that the molecular rubber chains were being broken into smaller pieces or fragments due to the large shear force encountered during the abrasion. Since the crosslinking points between the rubber chains, the polysulphidic bonds, are much weaker than the C-C bonds of the polymer backbone, it is suggested that some extend of devulcanisation processes occurred during the smearing wear. As a consequence, the fresh sticky debris can be dissolved in a toluene.

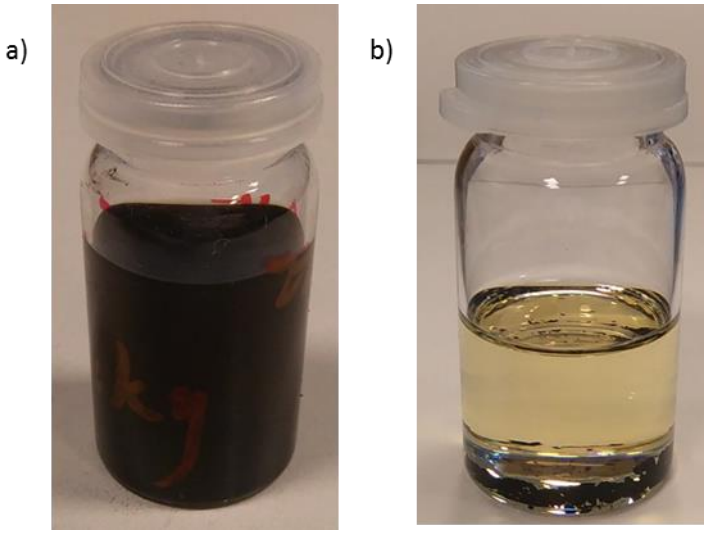

Figure 7-8. a) Fresh sticky debris of SBR80CB dissolved in toluene and b) old sticky debris of SBR80CB dissolved in toluene.

The change of the solubility of the sticky debris could be ascribed in principle to two mechanisms. The first one is that the broken crosslinks can somehow recover and reform 3-D polymer network. However, this seems to be unlikely, since the vulcanisation process requires energy to be activated and the sulphur content in the sticky debris is reduced when examined using EDX characterisation. Another possible mechanism might be that the filler network in the sticky debris can recover with time in a similar manner to the flocculation process during melt processing and the polymer chain fragments can easily be reabsorbed onto the filler surface forming “bound rubber” (Garten et al., 1956). During the abrasion process, the fracture of either polymer backbone or crosslinks results in the formation of free radicals. The filler particles act as strong radical scavengers due to their high surface energy, which can trap free radicals and stabilise them. Therefore, the solubility of the old sticky debris decreases. The amount of the insoluble rubber in the old sticky debris was determined using the same technique used to measure the bound rubber content of an unvulcanised rubber melt. The results are shown in Figure 7-9. The amount of insoluble rubber of the old sticky debris was more than the bound rubber of the uncured rubber melt.

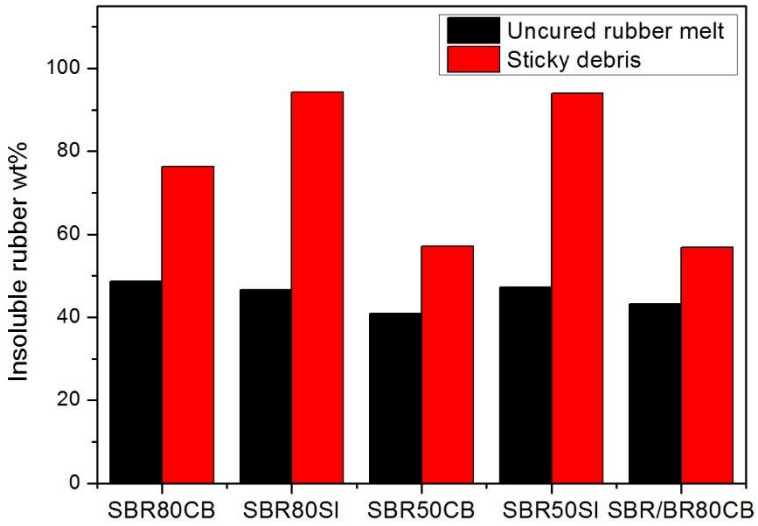

Figure 7-9. Amount of insoluble rubber for the sticky debris and uncured rubber melt.

7.3.5 Effect of the Sticky Layer on Rubber Friction

Figure 7-10 shows the friction behaviour of SBR/BR80SI during abrasion. The friction force increased slowly as the sticky layer was formed. It reached an equilibrium plateau after about 2000 revolutions. If the test was interrupted and then restarted as is shown in Figure 7-10 b), the initial restart value was higher than before but then a decrease in the friction was observed until the steady state friction value was eventually reached again. The differences in behaviour might be attributable to the time required to establish the steady state temperature profile again. As the temperature drops then the friction value increases. As the temperature builds-up at the sample surface then the friction is reduced. The initial increase of the friction force is countered this theory and so it is ascribed to the formation of the sticky layer on the surface increasing the friction behaviour. Figure 7-11 shows the averaged friction force of every 110 revolutions for SBR80SI at 20 cm/s sliding on sandpaper under dry contact conditions. The friction force was raised by around 10 N as the sticky layer was developed on the rubber surface. Once formed the subsequent changes under steady sliding conditions may all be attributed to changes in the surface temperature.

The increase of the friction as the sticky layer is developed is probably due to two effects. On the one hand, as the sticky layer is essentially a viscous liquid polymer, the low

modulus of the sticky layer presented on the rubber surface could give a greater contact area between the rubber surface and the counterpart. On the other hand, the devulcanisation processes as discussed above may make the sticky layer more viscous. Therefore, there are both adhesive and viscous contribution of the friction which might both be increased as the sticky layer is formed.

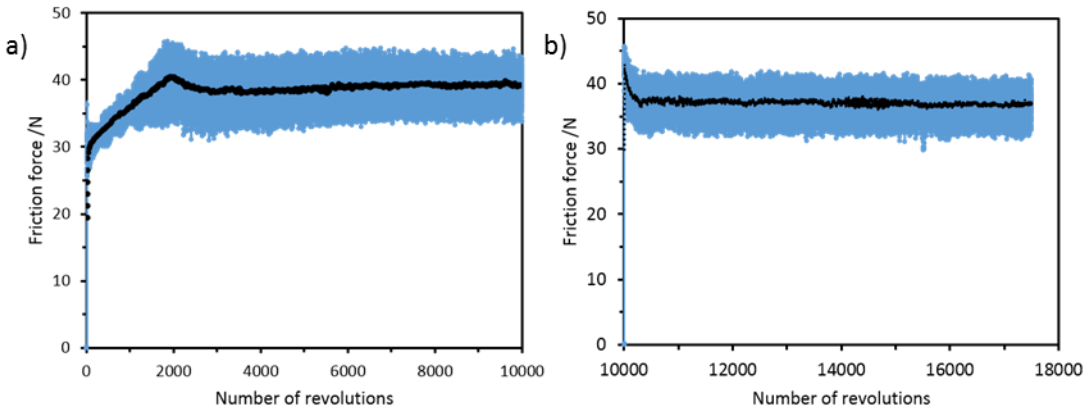

Figure 7-10. Friction profile during blade abrasion for SBR/BR80CB at 26 N normal force, blue line: the measured data and the black line: the average moving trend, a) 0 to 10000 revolutions and b) 10000 to 17000 revolutions.

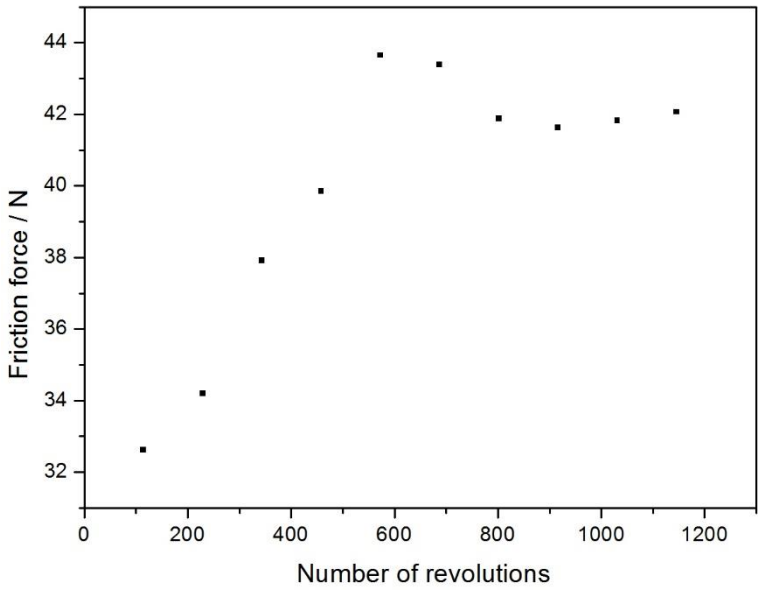

Figure 7-11. Averaged friction force of every 110 revolutions as a function of number of revolutions of surface abrasion for SBR80SI at 20 cm/s under dry contact.

7.3.6 Effect of the Sticky Layer on the Rate of Rubber Abrasion

The surface abrasion test that is described in Chapter 6 was repeated under the same rotation speed (sliding velocity), but using different platform translation velocities. This allowed the formation of the sticky layer on the rate of abrasion loss to be investigated. Figure 7-12 shows the abrasion rate for two rubber compounds as a function of platform moving velocity at a 20 cm/s sliding velocity. As discussed before SBR50SI presented abrasive wear at a rotational speed required to create a 20 cm/s sliding velocity. The rate of translating the platform had no significant effect on the measured rate of abrasion loss. However, for SBR80CB smearing wear determined the abrasion behaviour. The abrasion loss in this case was dependent upon and was seen to increase with the platform's sliding velocity.

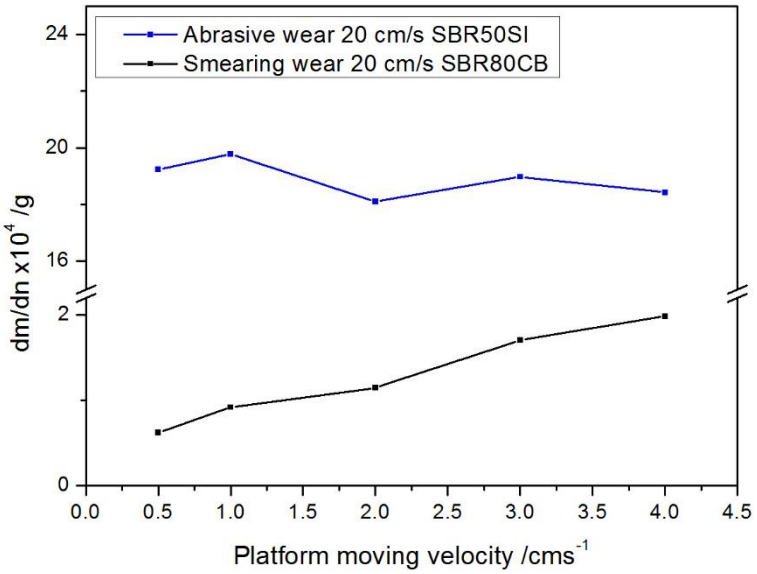

Figure 7-12. Abrasion loss as a function of platform moving velocity (each data point was measured using a new abrasive sandpaper).

Since for smearing wear the wear debris is in the form of sticky degraded rubber, the final abrasion rate depends on how fast this sticky debris can be removed from the rubber's surface. The faster the speed of the moving platform then the greater the contact surface provided for the sticky debris to be deposited. Therefore, the rate of abrasion increases. It is the same reason that people use fine drying powders to prevent smearing wear in certain types of laboratory testing (Grosch and Schallamach, 1966, Schallamach, 1968a). The small particles have a large surface area to adsorb the sticky

debris, which leads to an increase in the abrasion rate. Of course, adding a third party contact could also alter the fundamental abrasion mechanisms.

When the sticky layer generated on the rubber surface is allowed to age in air as described in section 7.3.4, then it becomes much easier to abrade off the bulk rubber wheel. Figure 7-13 shows the blade abrasion loss for SBR50CB at a 26 N normal force. The mass was measured every 500 revolution until the end of each day. Then the sample was left in the lab overnight prior to additional testing on the subsequent day. Each jump in the weight loss resulted from the very first measurements taken at the start of each day after just 500 additional revolutions. Clearly, leaving the sample overnight allowed the fresh sticky layer to age or become old. This ageing clearly resulted in a faster rate of abrasion loss for the first few revolutions. Then as the new sticky layer developed, the rate of abrasion loss was reduced.

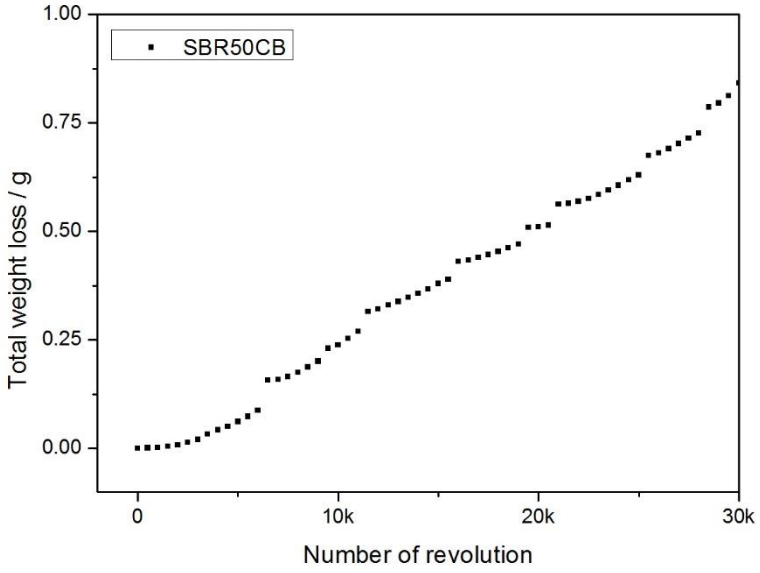

Figure 7-13. Abrasion loss of blade abrasion test for SBR50CB under 26 N normal force.

7.4 Summary and Conclusion

The sticky layer generated due to the smearing wear was systematically characterised in this thesis for the first time. Due to the raised temperature and the input mechanical energy, both rubber chains and crosslinks can break down during abrasion to form sticky debris. The sticky debris is a form of degraded rubber, which has a greater volatile content and forms more char during thermo-oxidative degradation possibly due to the

greater number of free radicals being present. There is more oxygen present in the sticky debris according to the EDX measurement, which confirms the thermo-oxidative effect during smearing wear.

Although there is no significant change of the glass transition temperature, the molecular weight of this sticky debris is almost one order magnitude lower than that of the original rubber, which gives the sticky and liquid like morphology. The degraded rubber chain fragments and broken filler network in the sticky layer can recover. As a consequence, the solubility of the sticky debris decreases with time.

The initial formation of the sticky layer on rubber surface during abrasion increases the friction force, since the sticky layer with both a lower modulus and a higher viscosity enhances both adhesive and viscous contribution of the rubber friction. The abrasion loss for the smearing wear depends on how fast the sticky debris can be removed. The faster it is removed, the greater abrasion rate is. The old sticky layer with lower solubility can be easily abraded off, which leads to a higher rate of abrasion loss.

8 Chapter Eight: Summary and Future Work

8.1 Summary

In this thesis the fundamental abrasion mechanisms for materials sliding against both smooth and rough surfaces under various different contact conditions have been investigated. Unlike most other solid materials, rubbers exhibit different abrasion mechanisms under different conditions due to their viscoelastic nature. Three different abrasion mechanisms have been confirmed. The experiments revealed that the abrasion losses for different mechanisms were significantly different by more than an order of magnitude from the fastest to the slowest. This presents a significant difficulty when trying to predict the real tyre wear behaviour. Each of these mechanisms has been examined using different abraders and various different characterisation techniques. The key findings are summarised as following.

Chapter 4 investigated the rubber abrasion under relatively smooth contact conditions. Two abrasion mechanisms are presented during blade abrasion. Smearing wear occurs during the initiation stage and a fatigue wear dominates the abrasion process when an abrasion pattern is fully developed at steady state on the rubber surface. There is some correlation between the crack growth behaviour observed during abrasion and that measured using pure shear fatigue testing for these SBR materials, which confirms that the dominant mechanism for fatigue wear is one of fatigue crack growth. The discrepancy between the measured rate of abrasion and that predicted from the fatigue crack growth test results is probably due to the differences between the different loading conditions. In particular the strain rate achieved during the blade abrasion test and that encountered during the fatigue crack growth test. An attempt to investigate this showed only a modest effect when testing the crack growth rate of the rubber using a range of different test piece loading rates. It is possible that the difference between these various different loading configurations was insufficient to make a significant effect. Another issue results from the inaccuracy of the approximate equation used to calculate the tearing energy during blade abrasion.

In Chapter 5 a FEA model was created to derive the tearing energy for fatigue wear. The VCCT approach was applied for the first time to calculate the tearing energy for rubber abrasion. The predicted tearing energy gave a closer correlation between the measured abrasion rate and the one predicted from the pure shear fatigue test data for an unfilled SBR material. For the various NR materials, it was likely that the strain rate during abrasion was sufficiently fast that any reinforcing strain induced crystallisation was suppressed. As a consequence, the correlation between the abrasion rate predicted from the fatigue crack growth and the measured rate was much worse than that for the SBR rubbers. It was confirmed that the VCCT provides an alternative method to calculate the tearing energy for rubber fracture in FEA simulations, as it accurately considers the local stresses and strains at the crack tip.

Chapter 6 discussed an investigation into the abrasion of rubber by a sharper contact surface by rotating rubber wheels on silicon carbide sandpaper at various velocities under both dry and wet conditions. Two types of abrasion mechanisms, abrasive wear and smearing wear, were present depending upon the specific rubber compounds and testing conditions of sliding velocity and lubrication conditions. The higher sliding velocities resulted in a significant temperature rise at the interface, which promoted the smearing wear. As a result of transfer layer to transfer layer contact, the abrasion rate for smearing wear was very low. In contrast, the lower sliding velocities produced the more rapid type of abrasive wear as a result of a lower heat generation. Adding water lubrication does not always reduce the abrasion rate. It can change the wear mechanism from smearing wear to abrasive wear, which serves to increase the abrasion rate. It appears that the smearing wear is easier to develop for carbon black compounds potentially due to their lower stiffness and lower filler-polymer interactions when compared to the silica compounds.

Chapter 7 characterised the sticky debris generated during blade abrasion in order to understand the smearing wear in greater detail. Both the rubber molecules and the crosslinks were broken down during the smearing wear, which resulted in a soluble, liquid like degraded rubber with a much lower molecular weight. The sticky debris had a greater volatile content and lower rubber content. The charring effect during the

thermo-oxidative degradation was larger for the sticky debris probably due to the presence of more free radicals left over from the abrasion. It appeared that the degraded rubber chain fragments and broken filler network in the sticky debris slowly recovered after abrasion. As a result, the solubility of the sticky debris decreased with time. This sticky debris with a lower solubility could more easily be abraded off, which resulted in a higher overall rate of abrasion loss. The sticky transfer layer also initially increased the friction force during abrasion.

8.2 Future Work

This thesis has carried out a detailed investigation on various mechanisms for rubber abrasion. However, there are still some aspects that can be explored further. For the fatigue wear, it would be worthy to match the exact identical loading conditions encountered during abrasion for the fatigue tests, especially for NR materials to see if strain induced crystallisation is suppressed or not. This requires more advanced fatigue test machines than were available throughout these studies, which can perform a more rapid loading and unloading. It might also require new fatigue test configurations, which can perform complex loading conditions, since both tension and compression are present at the same time during rubber abrasion. The additional fracture processes that actually remove the abrasion pattern tips would be another important aspect to investigate. It is this rate that determines the critical size of abrasion patterns for different rubber compounds under each specific loading condition and this significantly affects the measured abrasion rate.

The FEA model used here to calculate the tearing energy during abrasion assumed the rubber was perfectly elastic. It would be good to take into account the viscous contribution for the material model, so that the tearing energy for filled rubbers can be more accurately predicted as well. The model used displacement control to achieve the required normal force. However, force control is more realistic since the actual blade abrasion experiment is more closely related to a force control experiment.

For abrasive wear, sandpaper with only one grit size was used in this work. Abrasion tests on a range of different grit sized sandpaper with various different roughness values could be used to investigate how the surface roughness affects the abrasion mechanisms.

It would also be very interesting to examine the free radicals formed in the sticky debris in more detail. Electro Paramagnetic Resonance (EPR) would a useful technique to examine these free radicals. Preliminary EPR results are shown in Figure 8-1. Both original bulk rubber and sticky debris of SBR/BR60SI were tested over different time periods at room temperature. The decrease of the signal intensity indicates both sticky debris and bulk materials have free radicals. There is no significant decay in the signal intensity with time, which means the free radicals are stable at room temperature. These free radicals may arise from the inorganic fillers such as silica. It is also difficult to quantitatively compare the free radicals, since the effective volume of the EPR measurement in each case is not identical. Therefore, it would be useful to control the effective volume to quantitatively measure the free radicals more carefully.

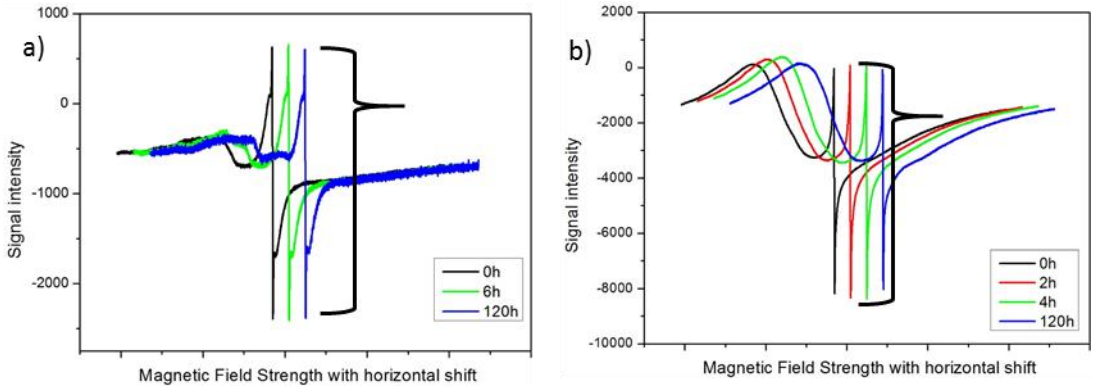

Figure 8-1. EPR curves of SBR/BR60SI: a) bulk material and b) sticky debris.

It would be also useful to measure the residual crosslinks of the old sticky debris to confirm if re-crosslinking was arising with time. Since the sticky debris has an irregular shape and is of very low volume, conventional crosslinking density measurements (swelling test and mechanical test) are impractical. ^{1}H-Double Quantum (DQ)-NMR is a new technique for the study of chain dynamics and structural constraints in rubber materials (Sotta et al., 1996, Berriot et al., 2002, Saalwächter, 2007, Vieyres et al., 2013).

The background theory and signal analysis principle for this NMR technique is presented in detail in the Appendix. Preliminary tests undertaken in collaboration with Prof. Paul Sotta were performed on the sticky debris for NR0 and uncured NR0 melt. For time-domain proton NMR measurement, the old sticky wear debris of NR0 and uncured NR0 melt were put into a test tube and inserted in the measuring probe. Experiments were carried out on a Bruker minispec mq20 proton low-field NMR spectrometer operating at 0.5 T with 90° pulses of 2 µs and a dead time of 12 µs. The experiments were done at 60 °C to insure fast motions and proper time averaging of spin interactions.

Preliminary test results are shown in Figure 8-2 for the reference and DQ signal. It is clear that the sticky debris has a different DQ-NMR response. The DQ signal is smaller and badly shaped, which indicates that a fraction of the material has been de-crosslinked during the abrasion process. This is more obvious when the function $f(t) = I_{ref}(t) - I_{DQ}(t)$ is plotted for both the NR0 melt and the sticky debris as shown in Figure 8-3. The contribution of the long-time tail is also shown in the graph, which corresponds to uncrosslinked network defects such as dangling chains or loops. The defect fraction in the NR0 is about 7.6%, whilst this fraction is around 75% in the sticky debris. This means that in the sticky debris, about 75% of the material is composed of uncrosslinked polymer, which also confirms the smaller polymer chain length of the sticky debris. The structural information about the rubber network can be obtained independently of relaxation effects by normalizing the DQ network to the full magnetization of the sample after subtraction of exponential long time signal tail (I_{def}), which can be expressed as $I_{nDQ} = I_{DQ} / (I_{DQ} + I_{ref} - I_{def})$. The result is shown in Figure 8-4. The crosslinked part of the debris (25%) is more crosslinked than the uncured rubber melt as expected, since crosslinked part in the sticky debris are cured whereas the rubber melt are uncured. Therefore, it can be concluded that in the sticky debris, a large fraction (75%) is uncrosslinked, while in the remaining fraction the crosslinking density remains similar to that before abrasion. The DQ-NMR provides a powerful way to measure the residual crosslinks in the sticky debris for unfilled rubber. It would be worth extending this technique to measure the sticky debris for the filled rubber materials in order to investigate the polymer reabsorption effect in the abraded debris.

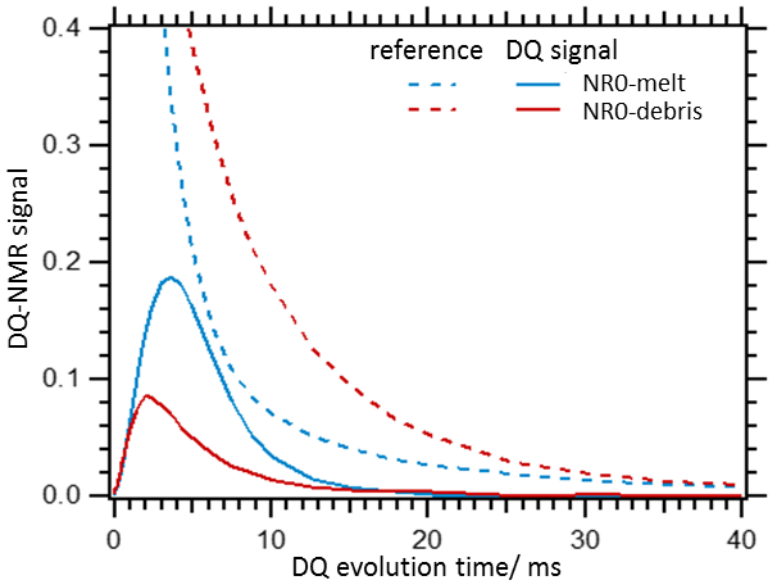

Figure 8-2. Original reference and DQ signal in uncured NR0 melt (blue curves) and NR0 sticky wear debris (red curves)

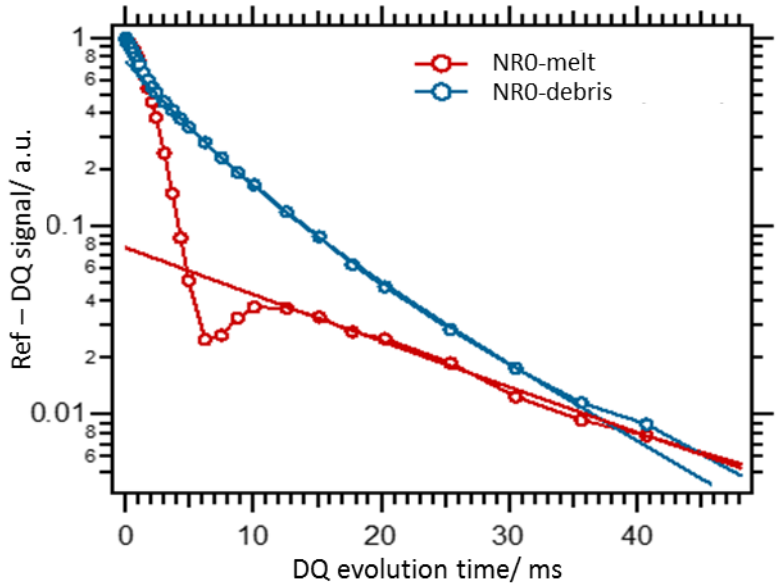

Figure 8-3. Reference – DQ signal for uncured NR0 melt and for NR0 sticky debris. The long time tail contribution is shown for each case.

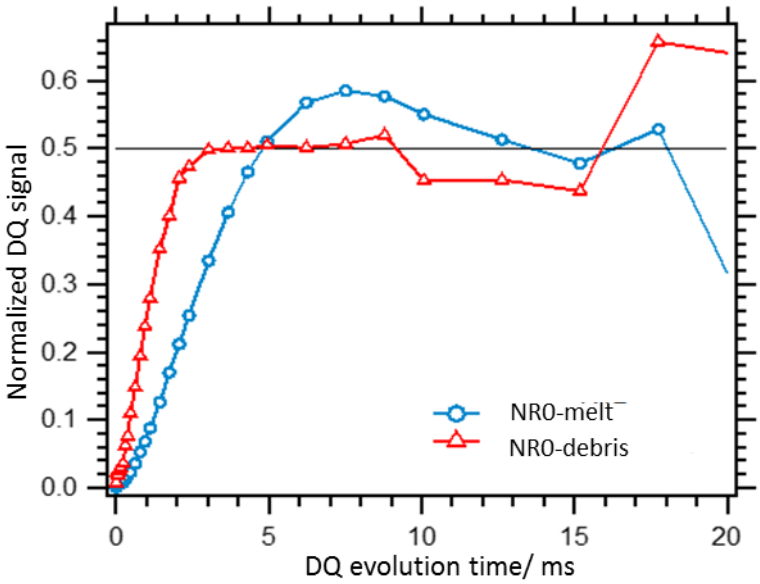

Figure 8-4. Normalized DQ curves for NR0 melt and NR0 sticky debris.

References

ABRAHAM, F. & ALSHUTH, T. 2015. "A new fatigue wear simulation method for road tyre wear" in Constitutive Models for Rubber IX: *Proceedings of the Ninth European Conference on Constitutive Models for Rubber, CRC Press, Prague, Czech Republic, September 2015,* 123. ISBN: 1315658151.

ADAMS, J., REYNOLDS, J., MESSER, W. & HOWLAND, L. 1952. Abrasion Resistance of GR-S Vulcanizates. *Rubber Chemistry and Technology,* 25**,** 191-208.

AKUTAGAWA, K., YAMAGUCHI, K., YAMAMOTO, A., HEGURI, H., JINNAI, H. & SHINBORI, Y. 2008. Mesoscopic mechanical analysis of filled elastomer with 3D-finite element analysis and transmission electron microtomography. *Rubber Chemistry and Technology,* 81**,** 182-189.

ARAYAPRANEE, W. 2012. Rubber abrasion resistance. *Abrasion Resistance of Materials, InTech, Rijeka***,** 147-166.

AUSTRELL, P.-E. & KARI, L. 2005. Constitutive Models for Rubber IV*: Proceedings of the Fourth European Conference on Constitutive Models for Rubber, CRC Press, Stockholm, Sweden, June 2005*, ISBN: 9780415383462.

BARANWAL, K. C. & STEPHENS, H. L. 2001. *Basic elastomer technology*, *Rubber Division (US),* ISBN: 091241507X.

BATEMAN, L. 1963. Chemistry and physics of rubber-like substances, *Elsevier Science Ltd (UK),* ISBN: 0853340609.

BERGSTROM, J. S. & BOYCE, M. C. 1999. Mechanical behavior of particle filled elastomers. *Rubber Chemistry and Technology,* 72**,** 633-656.

BERRIOT, J., MONTES, H., LEQUEUX, F., LONG, D. & SOTTA, P. 2002. Evidence for the shift of the glass transition near the particles in silica-filled elastomers. *Macromolecules,* 35**,** 9756-9762.

BOURBIGOT, S., GILMAN, J. W. & WILKIE, C. A. 2004. Kinetic analysis of the thermal degradation of polystyrene–montmorillonite nanocomposite. *Polymer Degradation and Stability,* 84**,** 483-492.

BUSFIELD, J., DAVIES, C. & THOMAS, A. 1996. Aspects of fracture in rubber components. *Progress in Rubber and Plastics Technology,* 12**,** 191-207.

BUSFIELD, J., JHA, V., LIANG, H., PAPADOPOULOS, I. & THOMAS, A. 2005. Prediction of fatigue crack growth using finite element analysis techniques applied to three-dimensional elastomeric components. *Plastics, Rubber and Composites,* 34**,** 349-356.

BUSFIELD, J., RATSIMBA, C. & THOMAS, A. 1999. Crack growth and predicting failure under complex loading in filled elastomers. *Finite Element Analysis of Elastomers, IMechE (UK),* 235-250, ISBN: 1860581714.

BUSFIELD, J. & THOMAS, A. 1999. Indentation tests on elastomer blocks. *Rubber Chemistry and Technology,* 72**,** 876-894.

BUSFIELD, J., TSUNODA, K., DAVIES, C. & THOMAS, A. 2002. Contributions of time dependent and cyclic crack growth to the crack growth behavior of non strain-crystallizing elastomers. *Rubber Chemistry and Technology,* 75**,** 643-656.

CHAMP, D., SOUTHERN, E. & THOMAS, A. 1974. Fracture mechanics applied to rubber abrasion, in LEE, L. H. (ed.) *Advances in Polymer Friction and Wear. Springer,* ISBN: 1461399424.

CIESIELSKI, A. 1999. An introduction to rubber technology, *Rapra Technology Ltd (UK),* ISBN: 1859571506.

COVENEY, V. & MENGER, C. 1999. Initiation and development of wear of an elastomeric surface by a blade abrader. *Wear,* 233**,** 702-711.

COWIE, J. M. G. & ARRIGHI, V. 2007. *Polymers: chemistry and physics of modern materials*, *CRC press*, ISBN: 1420009877.

DANNENBERG, E. 1986. Bound rubber and carbon black reinforcement. *Rubber Chemistry and Technology,* 59**,** 512-524.

DE, D. K. 1994. *The Effects of Particulate Filters on the Strain Energy Function and Crack Growth in Rubbers. PhD Thesis, Queen Mary University of London (UK)*

DE, S. K. & WHITE, J. R. 2001. *Rubber Technologist's Handbook*, *Rapra Technology Ltd (UK)*, ISBN: 1859572626.

DLUZNESKI, P. R. 2001. Peroxide vulcanization of elastomers. *Rubber Chemistry and Technology,* 74**,** 451-492.

DONNET, J.-B. 1993. *Carbon black: science and technology*, *Marvel Dekker, INC (US)*, ISBN: 082478975X.

DOROZHKIN, V., MOKHNATKIN, A., ZOTOV, A. & MOKHNATKINA, E. 2015. A study of the combined use of carbon black and silicon dioxide in tyre tread formulations. Part 3. Laboratory service tests of tread rubbers. *International Polymer Science and Technology,* 42**,** T35.

EINSTEIN, A. 1906. Eine neue bestimmung der moleküldimensionen. *Annalen der Physik,* 324**,** 289-306.

FLETCHER, W. & GENT, A. 1953. Apparatus for the Measurement of the Dynamic Shear Modulus and Hysteresis of Rubber at Low Frequencies. *Rubber Chemistry and Technology,* 26**,** 181-187.

FLETCHER, W. & GENT, A. 1954. Nonlinearity in the dynamic properties of vulcanized rubber compounds. *Rubber Chemistry and Technology,* 27**,** 209-222.

FRAGIADAKIS, D., BOKOBZA, L. & PISSIS, P. 2011. Dynamics near the filler surface in natural rubber-silica nanocomposites. *Polymer,* 52**,** 3175-3182.

FUKAHORI, Y., LIANG, H. & BUSFIELD, J. J. C. 2008. Criteria for crack initiation during rubber abrasion. *Wear,* 265**,** 387-395.

FUKAHORI, Y. & YAMAZAKI, H. 1994a. Mechanism of Rubber Abrasion 1. Abrasion Pattern Formation in Natural Rubber Vulcanite. *Wear,* 171**,** 195-202.

FUKAHORI, Y. & YAMAZAKI, H. 1994b. Mechanism of Rubber Abrasion 2. General Rule in Abrasion Pattern Formation in Rubbe-Like Materials, *Wear,* 178**,** 109-116.

FUKAHORI, Y. & YAMAZAKI, H. 1995. Mechanism of Rubber Abrasion 3. How is Friction Linked to Frature in Rubber Abrasion. *Wear,* 188**,** 19-26.

GABRIEL, P. 2010. *Investigation and modelling of rubber friction.* PhD Thesis, Queen Mary University of London (UK).

GARTEN, V., EPPINGER, K. & WEISS, D. 1956. Studies on Abrasion and Wear of Rubber. I. The Chemistry of Carbon Black and Its Effect on Abrasion as Determined by the National Bureau of Standards Method. *Rubber Chemistry and Technology,* 29**,** 1434-1444.

GEHMAN, S., WILKINSON JR, C. & DANIELS, R. 1955. Smearing of Vulcanized Rubber. *Rubber Chemistry and Technology,* 28**,** 508-518.

GENT, A. N. 1989. A Hypotheticacl Mechanism for Rubber Abrasion. *Rubber Chemistry and Technology,* 62**,** 750-756.

GENT, A. N. 2012. *Engineering with rubber: how to design rubber components*, Carl Hanser Verlag GmbH Co KG, ISBN: 1569902992.

GENT, A. N. & NAH, C. 1996. Abrasion of rubber by a blade abrader: Effect of blade sharpness and test temperature for selected compounds. *Rubber Chemistry and Technology,* 69**,** 819-833.

GENT, A. N. & PULFORD, C. T. R. 1983. Mechanisms of rubber abrasion. *Journal of Applied Polymer Science,* 28**,** 943-960.

GRIFFITH, A. A. 1921. The phenomena of rupture and flow in solids. *Philosophical transactions of the royal society of London. Series A, containing papers of a mathematical or physical character,* 221**,** 163-198.

GROSCH, K. 1963. The relation between the friction and visco-elastic properties of rubber. *Proceedings of the Royal Society of London A: Mathematical, Physical and Engineering Sciences, The Royal Society*, 21-39.

GROSCH, K. 1974. The speed and temperature dependence of rubber friction and its bearing on the skid resistance of tires, in HAYS. D. (ed.)*The Physics of Tire Traction.* Springer, ISBN: 9781475713725.

GROSCH, K. 2004. Correlation between road wear of tires and computer road wear simulation using laboratory abrasion data. *Rubber Chemistry and Technology,* 77**,** 791-814.

GROSCH, K. 2008. Rubber abrasion and tire wear. *Rubber Chemistry and Technology,* 81**,** 470-505.

GROSCH, K. & SCHALLAMACH, A. 1966. Relation between abrasion and strength of rubber. *Rubber Chemistry and Technology,* 39**,** 287-305.

GUTH, E. 1945. Theory of filler reinforcement. *Journal of applied physics,* 16**,** 20-25.

HACALOGLU, J., ERSEN, T., ERTUGRUL, N., FARES, M. M. & SUZER, S. 1997. Pyrolysis mass spectrometric analysis of styrene-butadiene block and random copolymers. *European polymer journal,* 33**,** 199-203.

HEINZ, M. & GROSCH, K. 2007. A laboratory method to comprehensively evaluate abrasion, traction and rolling resistance of tire tread compounds. *Rubber Chemistry and Technology,* 80**,** 580-607.

HOSLER, D., BURKETT, S. L. & TARKANIAN, M. J. 1999. Prehistoric polymers: rubber processing in ancient Mesoamerica. *Science,* 284**,** 1988-1991.

HOWLAND, L., WHITE, W. & MESSER, W. 1954. The Effect of Masterbatching, Compounding, and Testing Variables on Constant-Slip Abrasion Results. *Rubber Chemistry and Technology,* 27**,** 977-995.

HUANG, M. 2015. *The Strain Dependent Dielectric Behaviour of Carbon Black Filled Natural Rubber.* PhD thesis, Queen Mary University of London (UK).

INSTITUTION, B. S. 1988. Methods of testing vulcanized rubber – Part A9 Determination of abrasion resistance.

ISO4969 2010. Rubber, vulcanized or thermoplastic -- Determination of abrasion resistance using a rotating cylindrical drum device.

IWAI, T., UCHIYAMA, Y., SHIMOSAKA, K. & TAKASE, K. 2005. Study on the formation of periodic ridges on the rubber surface by friction and wear monitoring. *Wear,* 259**,** 669-675.

JOULE, J. P. 1859. On some thermo-dynamic properties of solids. *Philosophical Transactions of the Royal Society of London,* 149**,** 91-131.

KIM, Y. S., BYUN, H. S., KIM, S., KIM, W. Y., HAN, S. C. & GENT, A. N. 1999. Abrasion of selected rubber compounds with a DIN abrader. *Korea Polymer Journal,* 7**,** 116-123.

KRUEGER, R. 2004. Virtual crack closure technique: history, approach, and applications. *Applied Mechanics Reviews,* 57**,** 109-143.

LAKE, G. 1983. Aspects of fatigue and fracture of rubber. *Progress of Rubber technology,* 45**,** 89-143.

LAKE, G. & LINDLEY, P. 1964. Cut growth and fatigue of rubbers. II. Experiments on a noncrystallizing rubber. *Journal of Applied Polymer Science,* 8**,** 707-721.

LAKE, G., LINDLEY, P. & THOMAS, A. 1969. Fracture mechanics of rubber. The second international conference on fracture.

LAKE, G. & THOMAS, A. 1967. The strength of highly elastic materials. Proceedings of the Royal Society of London A: Mathematical, Physical and Engineering Sciences, The Royal Society, 108-119.

LIANG, H. 2007. *Investigating the Mechanism of Elastomer Abrasion.* Doctor of PhD thesis, Queen Mary University of London (UK).

LIANG, H., FUKAHORI, Y., THOMAS, A. G. & BUSFIELD, J. J. C. 2009. Rubber abrasion at steady state. *Wear,* 266**,** 288-296.

LIANG, H., FUKAHORI, Y., THOMAS, A. G. & BUSFIELD, J. J. C. 2010. The steady state abrasion of rubber: Why are the weakest rubber compounds so good in abrasion? *Wear,* 268**,** 756-762.

LINDLEY, P. & THOMAS, A. 1962. Fundamental study of the fatigue of rubbers. Proc. 4th Rubb. Technol. Conf.

LOADMAN, J. 2005. *Tears of the tree: the story of rubber-a modern marvel*, Oxford University Press Oxford, ISBN: 019856840.

LUGINSLAND, H.-D. 2002a. *A review on the chemistry and the reinforcement of the silica-silane filler system for rubber applications*, in Rubber Compounding: Chemistry and Applications. Shaker, ISBN: 1482235501.

LUGINSLAND, H.-D. 2002b. *A Review on the Chemistry and the Reinforcement of the Silica Silane Filler System for Rubber Applications*, in Rubber Compounding: Chemistry and Applications. Shaker, ISBN: 1482235501.

MARK, J. E., ERMAN, B. & ROLAND, M. 2013. *The science and technology of rubber*, Elsevier Academic press (USA), ISBN: 0124647863.

MATHEW, N. & DE, S. 1983. Scanning electron microscopy studies in abrasion of NR/BR blends under different test conditions. *Journal of Materials Science,* 18**,** 515-524.

MEDALIA, A. 1972. Effective degree of immobilization of rubber occluded within carbon black aggregates. *Rubber chemistry and technology,* 45**,** 1171-1194.

MEDALIA, A. I. 1970. Morphology of aggregates: VI. Effective volume of aggregates of carbon black from electron microscopy; Application to vehicle absorption and to die swell of filled rubber. *Journal of Colloid and Interface Science,* 32**,** 115-131.

MITCHELL, G. 1984. A wide-angle X-ray study of the development of molecular orientation in crosslinked natural rubber. *Polymer,* 25**,** 1562-1572.

MOFIDI, M., KASSFELDT, E. & PRAKASH, B. 2008. Tribological behaviour of an elastomer aged in different oils. *Tribology International,* 41**,** 860-866.

MOFIDI, M. & PRAKASH, B. 2010. The Influence of Lubrication on Two-body Abrasive Wear of Sealing Elastomers Under Reciprocating Sliding Conditions. *Journal of Elastomers and Plastics***,**43, 19-32.

MOONEY, M. 1940. A theory of large elastic deformation. *Journal of applied physics,* 11**,** 582-592.

MOORE, D. F. 1972. *The friction and lubrication of elastomers*, Pergamon, ISBN: 0080167497.

MORRIS, M. 2014. Predicting Wear Performance of Tire Tread Compounds. Conference Presentations, TireTech Expo, Cologne, Germany.

MUHR, A. H., POND, T. J. & THOMAS, A. G. 1987. ABRASION OF RUBBER AND THE EFFECT OF LUBRICANTS. *Journal De Chimie Physique Et De Physico-Chimie Biologique,* 84**,** 331-334.

MUHR, A. H. & RICHARDS, S. C. 1992. ABRASION OF RUBBER BY MODEL ASPERITIES. *Kautschuk Gummi Kunststoffe,* 45**,** 376-379.

MUHR, A. H. & ROBERTS, A. D. 1992. RUBBER ABRASION AND WEAR. *Wear,* 158**,** 213-228.

MUKAIYMA, A. 2014. *Numerical analysis and validation of energy release rate in rubber abrasion.* Master of Science Master's dissertation, Queen Mary University of London (UK).

NAH, C. & HAN, S. C. 1998. Morphology of worn surfaces of rubber compounds. *Korea Polymer Journal,* 6**,** 396-404.

NAH, S. H. & THOMAS, A. G. 1981. Migration and Blooming of Waxes to the Surface of Rubber Vulcanizates, *Rubber Chemistry and Technology,* 54**,** 255-265.

O'BRIEN, J., CASHELL, E., WARDELL, G. & MCBRIERTY, V. 1976. An NMR investigation of the interaction between carbon black and cis-polybutadiene. *Macromolecules,* 9**,** 653-660.

PAL, K., DAS, T., RAJASEKAR, R., PAL, S. K. & DAS, C. K. 2009. Wear characteristics of styrene butadiene rubber/natural rubber blends with varying carbon blacks by DIN abrader and mining rock surfaces. *Journal of applied polymer science,* 111**,** 348-357.

PAYNE, A. 1963. The Dynamic Properties of Carbon Black Loaded Natural Rubber Vulcanizates. Part II. *Rubber Chemistry and Technology,* 36**,** 444-450.

PAYNE, A. & WHITTAKER, R. 1971. Low strain dynamic properties of filled rubbers. *Rubber Chemistry and Technology,* 44**,** 440-478.

PERSSON, B. N. 1998. On the theory of rubber friction. *Surface Science,* 401**,** 445-454.

PERSSON, B. N. J. 2001. Elastic instabilities at a sliding interface. *Physical Review B,* 63.

PULFORD, C. T. R. 1983. Antioxidant Effects during Blade Abrasion of Natural Rubber. *Journal of Applied Polymer Science,* 28**,** 709-713.

RAMAKRISHNAN, R., DONOVAN, J. A. & MEDALIA, A. I. 1995. The Effect of Abrading Surfaces on the Wear of Rubber Tread Compounds. *Rubber Chemistry and Technology,* 68**,** 609-622.

RIVLIN, R. 1948. Large elastic deformations of isotropic materials. I. Fundamental concepts. *Philosophical Transactions of the Royal Society of London. Series A, Mathematical and Physical Sciences,* 240**,** 459-490.

RIVLIN, R. & THOMAS, A. G. 1953. Rupture of rubber. I. Characteristic energy for tearing. *Journal of polymer Science,* 10**,** 291-318.

ROBERTS, A. & THOMAS, A. 1975. The adhesion and friction of smooth rubber surfaces. *Wear,* 33**,** 45-64.

RUDAKOV, A. & KUVSHINSKII, E. 1964. The mechanism of abrasion of vulcanized rubber. *Rubber Chemistry and Technology,* 37**,** 291-296.

SAALWÄCHTER, K. 2007. Proton multiple-quantum NMR for the study of chain dynamics and structural constraints in polymeric soft materials. *Progress in Nuclear Magnetic Resonance Spectroscopy,* 51**,** 1-35.

SAIBEL, E. & TSAI, C. 1969. Tire wear model. DTIC Document.

SAKULKAEW, K. 2012. *Tearing of rubber.* PhD thesis, Queen Mary University of London (UK).

SCHALLAMACH, A. 1952. Abrasion of rubber by a needle. *Journal of polymer science,* 9**,** 385-404.

SCHALLAMACH, A. 1954. On the abrasion of rubber. *Proceedings of the Physical Society. Section B,* 67**,** 883.

SCHALLAMACH, A. 1958. Friction and abrasion of rubber. *Rubber Chemistry and Technology,* 31**,** 982-1014.

SCHALLAMACH, A. 1960. The role of hysteresis in tire wear and laboratory abrasion. *Rubber Chemistry and Technology,* 33**,** 857-867.

SCHALLAMACH, A. 1968a. Abrasion, fatigue, and smearing of rubber. *Journal of Applied Polymer Science,* 12**,** 281-293.

SCHALLAMACH, A. 1968b. Recent advances in knowledge of rubber friction and tire wear. *Rubber Chemistry and Technology,* 41**,** 209-244.

SMALLWOOD, H. M. 1945. Limiting Law of the Reinforcement of Rubber. *Rubber Chemistry and Technology,* 18**,** 292-305.

SMIT, P. 1966. The glass transition in carbon black reinforced rubber. *Rheologica Acta,* 5**,** 277-283.

SOANES, C. & STEVENSON, A. 2004. *Concise Oxford English Dictionary*, Oxford University Press, ISBN: 0199601119.

SOTTA, P., FÜLBER, C., DEMCO, D., BLÜMICH, B. & SPIESS, H. W. 1996. Effect of residual dipolar interactions on the NMR relaxation in cross-linked elastomers. *Macromolecules,* 29**,** 6222-6230.

SOUTHERN, E. & THOMAS, A. G. 1978. Studies of rubber abrasion. *Rubber chemistry and technology,* 52**,** 1008-1018.

STUPAK, P. R., KANG, J. H. & DONOVAN, J. A. 1990. Fractual characteristics of rubber wear surfaces as a function of load and velocity. *Wear,* 141**,** 73-84.

SUN, J., LEE, K. & LEE, H. 2000. Comparison of implicit and explicit finite element methods for dynamic problems. *Journal of Materials Processing Technology,* 105**,** 110-118.

THAVAMANI, P. & BHOWMICK, A. K. 1993. Influence of compositional variables and testing temperature on the wear of hydrogenated nitrile rubber *Journal of Materials Science,* 28**,** 1351-1359.

THAVAMANI, P., BHOWMICK, A. K. & KHASTGIR, D. 1993. Effect of aging on strenghth and wear of tank track pad compounds. *Wear,* 170**,** 25-32.

THOMAS, A. 1960. Rupture of rubber. VI. Further experiments on the tear criterion. *Journal of Applied Polymer Science,* 3**,** 168-174.

TRELOAR, L. 1975. The physics of rubber elasticity, 3rd edn. Clarendon. Oxford (UK), ISBN: 0198570279.

TUNNICLIFFE, L. B. 2015. *Particulate Reinforcement of Elastomers at Small Strains.* PhD thesis, Queen Mary University of London (UK).

UCHIYAMA, Y. 1986. The effect of environment on the friction and wear of rubber. *Wear,* 110**,** 369-378.

UCHIYAMA, Y. & ISHINO, Y. 1992. Pattern abrasion mechanism of Rubber. *Wear,* 158**,** 141-155.

VEIRH, A. G. 1992. A review of important factors affecting treadwear. *Rubber Chemistry and Technology,* 65**,** 601-659.

VIEHMANN, W. 1958. Surface heating by friction and abrasion by thermal decomposition. *Rubber Chemistry and Technology,* 31**,** 925-940.

VIEYRES, A., PÉREZ-APARICIO, R., ALBOUY, P.-A., SANSEAU, O., SAALWÄCHTER, K., LONG, D. R. & SOTTA, P. 2013. Sulfur-Cured Natural Rubber Elastomer Networks: Correlating Cross-Link Density, Chain Orientation, and Mechanical Response by Combined Techniques. *Macromolecules,* 46**,** 889-899.

WANG, M. J. 1998. Effect of polymer-filler and filler-filler interactions on dynamic properties of filled vulcanizates. *Rubber Chemistry and Technology,* 71**,** 520-589.

WANG, M. J., LU, S. X. & MAHMUD, K. 2000. Carbon‐silica dual‐phase filler, a new‐generation reinforcing agent for rubber. Part VI. Time‐temperature superposition of dynamic properties of carbon‐silica‐dual‐phase‐filler‐filled vulcanizates. *Journal of Polymer Science Part B: Polymer Physics,* 38**,** 1240-1249.

WEI, Z., LU, Y., MENG, Y. & ZHANG, L. 2012. Study on wear, cutting and chipping behaviors of hydrogenated nitrile butadiene rubber reinforced by carbon black and in-situ prepared zinc dimethacrylate. *Journal of Applied Polymer Science,* 124**,** 4564-4571.

WILLIAMS, M. L., LANDEL, R. F. & FERRY, J. D. 1955. The temperature dependence of relaxation mechanisms in amorphous polymers and other glass-forming liquids. *Journal of the American Chemical society,* 77**,** 3701-3707.

WOLFF, S., WANG, M.-J. & TAN, E.-H. 1993. Filler-elastomer interactions. Part VII. Study on bound rubber. *Rubber Chemistry and Technology,* 66**,** 163-177.

WU, G., THOMAS, A. G. & BUSFIELD, J. J. C. 2013. *Effect of the blade sharpness on the blade abrasion of rubber*. in Constitutive Models for Rubber VIII: *Proceedings of the Ninth European Conference on Constitutive Models for Rubber, CRC Press, San Sebastian, Spain, June 2013*. ISBN: 1138000728.

WU, Y., ZHOU, Y., LI, J., ZHOU, H., CHEN, J. & ZHAO, H. 2016. A comparative study on wear behavior and mechanism of styrene butadiene rubber under dry and wet conditions. *Wear, 356, 1-8*.

ZHANG, S. W. 1984a. MECHANISMS OF RUBBER ABRASION IN UNSTEADY STATE. *Rubber Chemistry and Technology,* 57**,** 755-768.

ZHANG, S. W. 1984b. Investigation of abrasion of nitrile rubber. *Rubber Chemistry and Technology,* 57**,** 769-778.

ZHANG, S. W. 1985. Theory of rubber abrasion by a line contact. *Acs Symposium Series,* 287**,** 189-203.

ZHANG, S. W. 1989. Advances in studies on rubber abrasion. *Tribology International,* 22**,** 143-148.

ZHANG, S. W. & YANG, Z. C. 1997. Energy theory of rubber abrasion by a line contact. *Tribology International,* 30**,** 839-843.

Appendix: Theory of ^{1}H-Double Quantum (DQ) NMR

Theoretical Background

The theoretical background of 1H-DQ NMR is fully described by Vieyres et al. (2013) as follows. Time-domain proton NMR spectroscopy is based on the measurement of the residual tensorial interactions, which originate from incomplete motional averaging of chain segments fluctuating rapidly between topological constraints, such as cross-links or chain entanglements. The local anisotropy of reorientational motions is described by a nonzero dynamical orientation of the polymer backbone $\langle P_2(\cos\theta')\rangle$ defined as the time average of the second-order Legendre polynomial (Mitchell, 1984):

$$\langle P_2(\cos\theta')\rangle = \frac{1}{t}\int_0^t \left(\frac{3\cos^2\theta'(t')-1}{2}\right), \qquad \text{Equation A-1}$$

in which θ' is the time-dependent angle between the local chain direction (segmental orientation) and a reference direction. At high enough temperature (with respect to T_g), reorientational motions are fast and the above time average stabilizes rapidly at short times t. For a network chain, topological constraints such as entanglements and cross-links lead to a nonzero permanent time average, which gives a dynamic average orientation of the polymer backbone, related to the length R and orientation α of the end-to-end vector. In a freely jointed rigid rod chain model, the average segment orientation is:

$$\langle P_2(\cos\theta')\rangle \approx \frac{3}{5}\frac{R^2}{N^2b^2}\frac{3\cos^2\alpha-1}{2} \approx S_b\frac{3\cos^2\alpha-1}{2} \qquad \text{Equation A-2}$$

where N is the number of statistical segments (freely jointed rigid rods) between constraints and b the statistical segment length.

The overall NMR signal is then the sum of contributions from all chains. From this, an average value of the local backbone orientation with respect to the end-to-end vector arises, which corresponds to S_b. Using the usual result for ideal chains $R^2 = Nb^2$, it may be written:

$$S_b \approx \frac{3}{5}\frac{R^2}{N^2 b^2} \propto \frac{1}{N} \approx \nu \qquad \text{Equation A-3}$$

Since the proton dipolar coupling, which is NMR observable, depends on molecular orientation, the nonzero dynamic orientation of the polymer backbone S_b is detected in NMR because it gives a nonzero residual dipolar coupling. S_b is calculated from the experimentally measured average residual dipolar coupling constant D_{res}, by comparison with its static counterpart, D_{static}, as (k_c is a correction factor <1 accounting for the spin arrangement and motions within a statistical segment)

$$S_b = k_c \frac{D_{res}}{D_{static}} \qquad \text{Equation A-4}$$

According to Equation A-3 and Equation A-4, D_{res} is inversely proportional to the average molecular weight of network chains between cross-links M_c or, equivalently, proportional to the crosslinking density ν. Entanglements also contribute to the NMR signal. Assuming a constant entanglement density and additivity of entanglement and cross-link densities, we may write $D_{res} \propto 1/M_c + 1/M_e$, with M_e the entanglement molecular weight.

Signal Analysis

Proton MQ-NMR involves a normalization procedure using two sets of experimental data, the DQ build-up (I_{DQ}) and reference decay (I_{ref}) curves both measured as a function of the DQ evolution time (τ_{DQ}), which represents the variable duration of the pulse sequence. The sum of both components corresponds to the full magnetization of the sample, $I_{\Sigma MQ} = I_{DQ} + I_{ref}$. That is the signal from dipolar coupled network segments and signal for uncoupled, essentially isotropic mobile network defects (such as dangling chains, loops, and sol chains). Note that protons in solid like environments are not detected in this experiment. In any case, their relative contribution to the total signal is low. The individual fractions are characterized by rather different relaxation behaviour: coupled segments relax faster and typically non-exponentially, while the signal for non-coupled (network defects) shows a slower exponential decay. Then, structural

information about the elastomer network can be obtained independently of relaxation effects by normalizing the DQ build-up through point by point division by the sum $I_{\Sigma MQ}$ after subtraction of exponential long-time signal tails (I_{def}) related to network defects: $I_{nDQ} = I_{DQ} \Big/ \left(I_{\Sigma MQ} - I_{def} \right)$ as shown in Figure A-1.

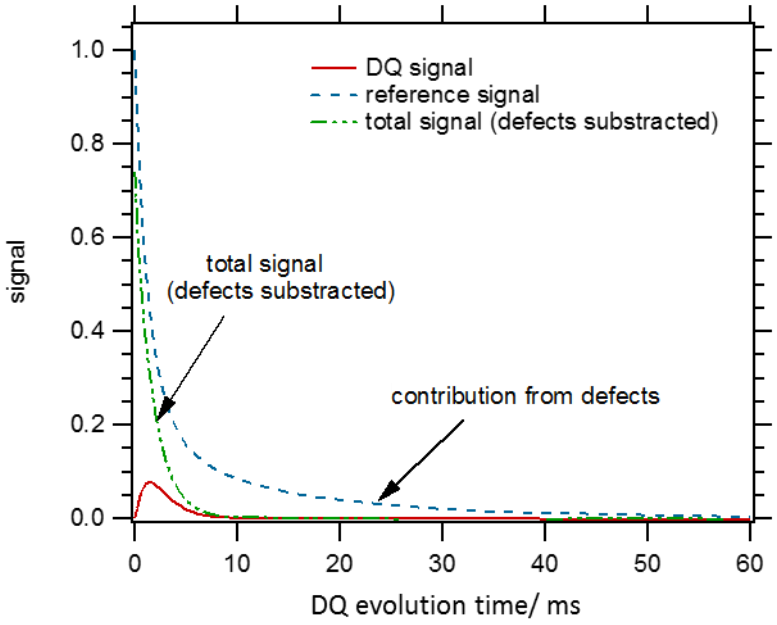

Figure A-1. Raw DQ and reference signals, total signal obtained as the sum of reference (with long time exponential contribution from network defects subtracted).

The theoretical shape of the final normalized DQ signal is:

$$I_{nDQ}(t) = \left\langle \sin^2(D_{res}t) \right\rangle = \frac{1}{2}\left(1 - \cos\left(2D_{res}t\right)\right) \qquad \text{Equation A-5}$$

It looks like in Figure A-2. Roughly, the value of D_{res} is extracted from the initial slope, or from the evolution time at half-height, or more precisely by fitting by an appropriate heuristically chosen function. I_{nDQ} is determined by the residual dipolar interactions related only to the network structure and proportional to S_b . It is independent of any temperature-dependent relaxation effect, and it must reach the theoretical relative amplitude of 0.5 in the long-time limit. In some cases, NMR data analysis yields not only the average D_{res} but also the full distribution over the sample.

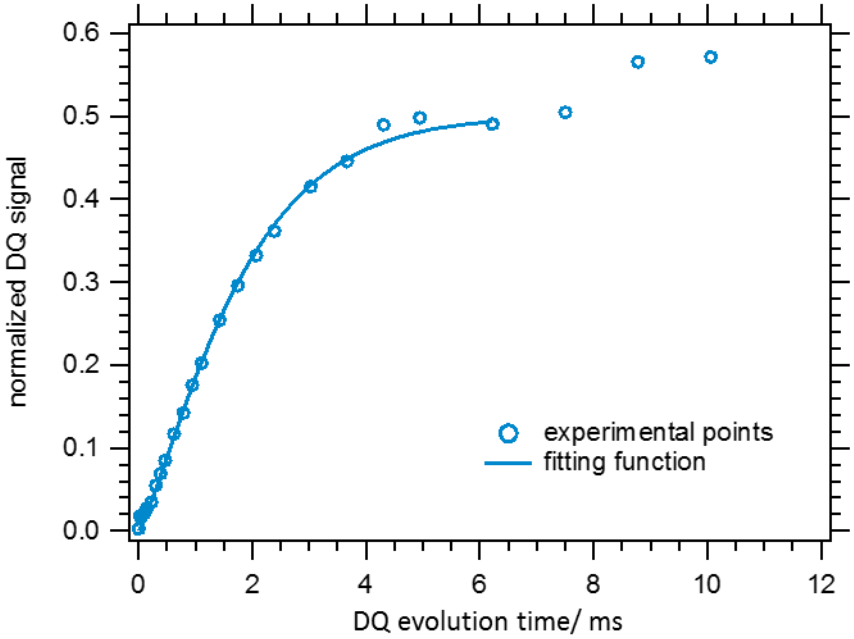

Figure A-2. Normalized DQ signal obtained by dividing the DQ signal by the total signal (with defects subtracted).